

# **ELECTROMAGNETIC INVERSE SCATTERING PROBLEMS**

**Li PAN**

B. Eng., Zhejiang University

M. Sc., Chalmers Tekniska Högskola

A THESIS SUBMITTED  
FOR THE DEGREE OF DOCTOR OF PHILOSOPHY  
DEPARTMENT OF ELECTRICAL AND COMPUTER  
ENGINEERING  
NATIONAL UNIVERSITY OF SINGAPORE

2011



## **Acknowledgments**

I take great joy in expressing my deepest gratitude to my supervisor, Prof. Swee-Ping Yeo, for his offering me the chance of pursuing this PhD program, also for his invaluable guidance and support throughout the course of this program. I consider myself most fortunate to work under his supervision, which has made the past three years such an enjoyable and rewarding experience.

In addition, I owe to Prof. Xudong Chen a huge debt of gratitude, which is not in my power to repay, for his wise suggestions, patient teaching, understanding and inspiring. The progress of this PhD program would not be possible without his support.

Also, I am grateful for the productive interactions with Prof. Linfang Shen, Dr. Krishna Agarwal, Dr. Rencheng Song, Mr. Meysam Sabahialshoara, and other colleagues in Microwave Research Laboratory.

Lastly, I wish to thank my parents, who supported me in my decision of pursuit of PhD and displayed such love during the PhD program.



# Contents

<b>List of Publications</b>	<b>v</b>
<b>List of Acronyms</b>	<b>ix</b>
<b>List of Tables</b>	<b>xi</b>
<b>List of Figures</b>	<b>xvii</b>
<b>Mathematical Notations</b>	<b>xvii</b>
<b>1 Introduction</b>	<b>1</b>
1.1 What is inverse scattering problem? . . . . .	1
1.2 Review of the approaches to inverse scattering problems . . . . .	5
1.2.1 Inversion methods for full-data measurement . . . . .	5
1.2.2 Inversion methods for phaseless-data measurement . . . . .	12
1.3 Mathematical and physical preliminaries . . . . .	15
1.3.1 Maxwell's equations and constitutive relationships . . . . .	15
1.3.2 Helmholtz equations in homogeneous media . . . . .	17
1.3.3 Dyadic Green's function in homogeneous media . . . . .	20
1.3.4 Green's Function for cylindrical geometry . . . . .	22
1.3.5 Lippmann-Schwinger equation . . . . .	26
1.3.6 The method of moments (MoM) . . . . .	28
1.3.7 The coupled dipole method (CDM) . . . . .	32
1.3.8 A glimpse at Wirtinger calculus for optimization . . . . .	34
1.4 Synopsis of this thesis . . . . .	36

---

<b>2</b>	<b>Full Data Subspace-based Optimization Method</b>	<b>39</b>
2.1	Original contributions . . . . .	39
2.2	FD-SOM in the framework of CDM . . . . .	42
2.2.1	Formulation of the forward scattering problem . . . . .	42
2.2.2	Inversion algorithm . . . . .	46
2.2.3	Numerical results . . . . .	47
2.3	FD-SOM in the framework of MoM . . . . .	52
2.3.1	Formulation of the forward scattering problem . . . . .	52
2.3.2	Inversion algorithm . . . . .	58
2.3.3	Numerical results . . . . .	59
2.4	Comparison among the variants of SOM . . . . .	62
2.4.1	The forward scattering problem . . . . .	62
2.4.2	Subspace-based optimization method and its variants . . . . .	64
2.4.3	Numerical Simulations and Comparisons . . . . .	66
2.5	Conclusion and Discussion . . . . .	79
<b>3</b>	<b>Phaseless Data Subspace-based Optimization Method</b>	<b>83</b>
3.1	Original contributions . . . . .	83
3.2	Formulation of forward scattering problem . . . . .	85
3.3	Phaseless Data Subspace-based optimization method . . . . .	88
3.4	Numerical results . . . . .	92
3.5	Conclusion . . . . .	100
<b>4</b>	<b>Compressive Phaseless Imaging (CPI)</b>	<b>103</b>
4.1	Original contributions . . . . .	103
4.2	Phaseless Imaging in the Framework of Compressive Sensing . . . . .	105
4.2.1	Description of Physical Setup . . . . .	105

---

4.2.2	Formulation of scattering phenomenon in homogeneous background medium . . . . .	106
4.2.3	Applicability of Compressive Sensing . . . . .	110
4.2.4	Phaseless Imaging with Compressive Sensing . . . . .	112
4.2.5	Phaseless Imaging of point-like scatterers in heterogeneous background medium . . . . .	113
4.3	Numerical Experiments . . . . .	114
4.4	Conclusion . . . . .	120
<b>5</b>	<b>Future Work</b>	<b>123</b>
	<b>Bibliography</b>	<b>127</b>





# List of Publications

1. L. Pan, X. Chen, and S. P. Yeo, "A Compressive-sensing-based Phaseless Imaging Method for Point-like Dielectric Objects," submitted to *IEEE Trans. Antennas Propag.*, 2011.
2. L. Pan, K. Agarwal, Y. Zhong, S. P. Yeo, and X. Chen, "Subspace-based optimization method for reconstructing extended scatterers: Transverse electric case," *J. Opt. Soc. Am. A*, vol. 26, pp. 1932 – 1937, 2009.
3. L. Pan, X. Chen, and S. P. Yeo, "Application of the subspace-based optimization method in the framework of the method of moments: Transverse electric case," in *Asia-Pacific Microwave Conference*, Singapore, Dec. 2009.
4. L. Pan, Y. Zhong, X. Chen, and S. P. Yeo, "Subspace-based optimization method for inverse scattering problems utilizing phaseless data", *IEEE Trans. Geosci. Remote Sens.*, Vol. 49. pp. 981 – 987, 2011.
5. L. Pan, X. Chen, Y. Zhong, and S. P. Yeo, "Comparison among the variants of the subspace- based optimization method for addressing inverse scattering problems: transverse electric case", *J. Opt. Soc. Am. A*, Vol. 27, pp. 2208-15, 2010.
6. L. Pan, X. Chen, S. P. Yeo, "Nondestructive evaluation of nano-scale structures: inverse scattering approach", *Applied Physics, A*, Vol. 101, pp. 143-146, 2010.
7. L. Pan, X. Chen, and S. P. Yeo, "Nondestructive Evaluation of Extended Scatterers Using Phaseless Data Subspace-based Optimization Method in the

- Framework of the Method of Moments”, *PIERS Proceedings*, Marrakesh, Morocco, March 20-23, 2011
8. K. Agarwal, L. Pan, S. P. Yeo, Y. K. Leong, M. P. S. Han, O. Y. Chan, and X Chen, “Practical applications of multiple signal classification,” in *International Journal of RF and Microwave Computer-Aided Engineering*, accepted, 2011.
  9. K. Agarwal, L. Pan, and X. Chen, “Subspace-based optimization method for reconstruction of two-dimensional complex anisotropic dielectric objects,” *IEEE Trans. Microw. Theory Tech.*, vol. 58, pp. 1065 – 74, 2010.
  10. L. Shen, X. Chen, X. Zhang, and L. Pan, “Blue-shifted contra-directional coupling between a periodic and conventional dielectric waveguides”, *Opt. Express*, Vol. 18, pp. 9341- 50, 2010.
  11. K. Agarwal, Xudong Chen, L. Pan, S. P. Yeo, “Multiple signal classification algorithm for non-destructive imaging of reinforcement bars and empty ducts in circular concrete columns”, *2011 General Assembly and Scientific Symposium of the International Union of Radio Science (Union Radio Scientifique Internationale-URSI)*, Istanbul, Turkey, 2011.

# List of Acronyms

BIM	Born iterative method
CDM	coupled dipole method
CG	conjugate gradient
CPI	Compressive Phaseless Imaging
CS	compressive (compressed) sensing
CSI	contrast source inversion
CT	computed tomography
CUDA	compute unified device architecture
DBIM	distorted Born iterative method
DORT	Décomposition de l'Opérateur de Retournement Temporel
DRIM	distorted Rytov iterative method
DT	diffraction tomography
FD	full-data
FD-SOM	full-data subspace-based optimization method
FFT	fast Fourier transform
FMM	fast multipole method
FPGA	field-programmable gate array
GPU	graphics processing unit
HPC	high performance computing
LM	Levenberg-Marquardt
LSM	linear sampling method
MLFMA	multilevel fast multipole algorithm
MoM	method of moments
MPI	the message passing interface
MRC SI	multiplicative regularized contrast source inversion
MUSIC	multiple signal classification
OpenMP	open multi-processing
OpenCL	open computing language
PD	phaseless-data
PD-SOM	phaseless-data subspace-based optimization method
SOM	Subspace-based optimization methods
STIE	source type integral equation
TSOM	twofold subspace-based optimization method
WGN	White Gaussian noise



# List of Tables

1.1	Four types of Green's function for cylinder background . . . . .	23
1.2	Wirtinger derivatives . . . . .	35
1.3	Wirtinger gradients . . . . .	36
2.1	Variables used in the formulation of the forward scattering problem	64
2.2	Comparison of the performance of the three variants of SOM in the numerical experiments . . . . .	72
3.1	Variables used in the formulation of the forward scattering problem	87
4.1	Four types of Green's functions . . . . .	114



# List of Figures

1.1	Setup for Inverse Scattering Experiment . . . . .	4
1.2	Illustration of Graf’s addition theorem . . . . .	22
1.3	Dividing the domain of interest . . . . .	27
1.4	Evaluation of 2-D depolarization dyadic $\overline{\overline{\mathbf{L}}}$ [115] . . . . .	30
1.5	Evaluation of 3-D depolarization dyadic $\overline{\overline{\mathbf{L}}}$ [115] . . . . .	31
2.1	Geometry of the inverse scattering problem. . . . .	43
2.2	An annulus with inner radius $0.15\lambda$ and outer radius $0.3\lambda$ . (a). Exact permittivity. (b) Reconstructed permittivity for SNR=20dB. (c) Reconstructed permittivity for SNR=10dB. . . . .	50
2.3	Singular values of the matrix $\overline{\overline{\mathbf{G}}}_S$ in the first numerical simulation. . . . .	51
2.4	Absolute residue versus number of iterations for different values of $L$ . . . . .	51
2.5	The pattern consisting of a circle and an annulus. (a) Exact relative permittivity. (b) Reconstructed relative permittivity for SNR=10dB. . . . .	53
2.6	The exact digit patterns of relative permittivity . . . . .	54
2.7	The reconstructed digit patterns of relative permittivity . . . . .	55
2.8	Singular values of the matrix $\overline{\overline{\mathbf{G}}}_S$ in the first numerical simulation. . . . .	60
2.9	An annulus with inner radius $0.15\lambda$ and outer radius $0.3\lambda$ . (a). Exact permittivity. (b) Reconstructed permittivity under 20dB Gaussian white noise. (c) Reconstructed permittivity under 10dB Gaussian white noise. . . . .	61
2.10	The pattern consisting of a circle and an annulus. (a) Exact relative permittivity. (b) Reconstructed relative permittivity with 10dB Gaussian white noise. . . . .	63

- 
- 2.11 The pattern of an annulus. (a1),(a2) Exact patterns of the real part and the imaginary part of relative permittivity. (b1),(b2) Reconstructed patterns of the real part and the imaginary part using the original SOM under 10% Gaussian white noise. (c1),(c2) Reconstructed patterns of the real part and the imaginary part using the CSI-like SOM under 10% Gaussian white noise. (d1),(d2) Reconstructed patterns of the real part and the imaginary part using the novel variant of SOM under 10% Gaussian white noise. . . . . 70
- 2.12 The pattern of a hollow square. (a1),(a2) Exact patterns of the real part and the imaginary part of relative permittivity. (b1),(b2) Reconstructed patterns of the real part and the imaginary part using the original SOM under 10% Gaussian white noise. (c1),(c2) Reconstructed patterns of the real part and the imaginary part using the CSI-like SOM under 10% Gaussian white noise. (d1),(d2) Reconstructed patterns of the real part and the imaginary part using the novel variant of SOM under 10% Gaussian white noise. . . . . 71
- 2.13 The pattern of an annulus. (a). Exact pattern of relative permittivity. (b) Reconstructed pattern using the original SOM under 31.6% Gaussian white noise. (c) Reconstructed pattern using the CSI-like SOM under 31.6% Gaussian white noise. (d) Reconstructed pattern using the novel variant of SOM under 31.6% Gaussian white noise. . . . . 73



2.14	The pattern consisting of two overlapping annuli. (a). Exact pattern of relative permittivity. (b) Reconstructed pattern using the original SOM under 31.6% Gaussian white noise. (c) Reconstructed pattern using the CSI-like SOM under 31.6% Gaussian white noise. (d) Reconstructed pattern using the novel variant of SOM under 31.6% Gaussian white noise. . . . .	75
2.15	The pattern consisting of a circle and an annulus. (a). Exact pattern of relative permittivity. (b) Reconstructed pattern using the original SOM under 31.6% Gaussian white noise. (c) Reconstructed pattern using the CSI-like SOM under 31.6% Gaussian white noise. (d) Reconstructed pattern using the novel variant of SOM under 31.6% Gaussian white noise. . . . .	76
2.16	The Austria pattern. (a). Exact pattern of relative permittivity. (b) Reconstructed pattern using the original SOM under 31.6% Gaussian white noise. (c) Reconstructed pattern using the CSI-like SOM under 31.6% Gaussian white noise. (d) Reconstructed pattern using the novel variant of SOM under 31.6% Gaussian white noise.	77
3.1	Geometry of the inverse scattering problem. . . . .	86
3.2	Singular values of the matrix $\overline{\overline{G}}_S$ in the first numerical simulation.	94
3.3	An annulus with inner radius $0.15\lambda$ and outer radius $0.3\lambda$ . (a). Exact relative permittivity. (b) Reconstructed relative permittivity with 50% Gaussian white noise. . . . .	95
3.4	The exact relative permittivity pattern is shown in Fig. 3.3 (a). (a) Initial guess generated by random numbers. (b) Reconstructed relative permittivity with $L = 9$ . (c) Reconstructed relative permittivity with $L = 1$ . . . . .	97

3.5	The pattern consisting of a circle and an annulus. (a) Exact relative permittivity, (b) Reconstructed relative permittivity with 31.6% Gaussian white noise. . . . .	98
3.6	Residual versus number of iterations in the optimization for determining the deterministic portion corresponding to the first incidence. "Experiment 1" means the reconstruction of an annulus from the initial guess of free space, as illustrated in Fig. 3.3; "Experiment 2" means the reconstruction of the pattern consisting of a circle and an annulus from free space initial guess, as illustrated in Fig. 3.5; and the residual is defined as the value of objective function, Eq. (3.4). . . . .	99
3.7	Absolute residue versus number of iterations in the optimization for determining relative permittivity. The residual is defined to be the the value of objective function, Eq. (3.7). . . . .	100
4.1	Configuration of physical setup . . . . .	115
4.2	The pattern consisting of two point-like objects. (a) Exact pattern of relative permittivity. (b) Reconstructed pattern obtained by solving (4.12) with no noise added into measurement. (c) Reconstructed pattern obtained by solving (4.13) with Gaussian white noise added into measurement (SNR=20 dB). (d) Reconstructed pattern obtained by solving (4.13) with Gaussian white noise added into measurement (SNR=10 dB). . . . .	116
4.3	Reconstructed patterns in the first experiment without noise for the number of RX antennas being 6, 8, 10, 12, 14, 16, 18, 20, 22 in (a), (b), (c), (d), (e), (f), (g), (i), respectively. . . . .	118
4.4	The error of reconstructed patterns in the first experiment without noise for varying number of RX antennas. . . . .	118

- 
- 4.5 The pattern consisting of five point-like objects. (a) Exact pattern of relative permittivity. (b) Reconstructed pattern obtained by solving (4.12) with no noise added into measurement. (c) Reconstructed pattern obtained by solving (4.13) with Gaussian white noise added into measurement (SNR=20 dB). (d) Reconstructed pattern obtained by solving (4.13) with Gaussian white noise added into measurement (SNR=10 dB). . . . . 119
- 4.6 The pattern consisting of two point-like objects in a cylindrical heterogeneous background medium. (a) Exact pattern of relative permittivity. (b) Reconstructed pattern obtained by solving (4.12) with no noise added into measurement. (c) Reconstructed pattern obtained by solving (4.13) with Gaussian white noise added into measurement (SNR=20 dB). . . . . 121



# Mathematical Notations

- *Italic*

we will use italic font to represent scalar variables, for example,

$$E_x^{\text{inc}}, \quad \varepsilon_x.$$

- *Italic*

Italic font under one line represents a vector as a result of discretization, for example,

$$\overline{E} = [E_1, E_2, \dots, E_n]^T.$$

- *Italic*

Italic font under two lines represents a matrix, for example,

$$\overline{\overline{G}} = \begin{bmatrix} G_{11} & G_{12} & G_{13} \\ G_{21} & G_{22} & G_{23} \\ G_{31} & G_{32} & G_{33} \end{bmatrix}$$

- **Boldface**

The boldface font is used to represent spacial vector, which has three components in  $x$ ,  $y$ , and  $z$  directions, respectively, for example,

$$\mathbf{E} = \hat{\mathbf{x}}E_x + \hat{\mathbf{y}}E_y + \hat{\mathbf{z}}E_z.$$

- **Boldface**

Boldface font under two lines represents dyadic operator, for example,

$$\begin{aligned} \overline{\overline{\mathbf{G}}} &= \hat{\mathbf{x}}\hat{\mathbf{x}}G_{xx} + \hat{\mathbf{x}}\hat{\mathbf{y}}G_{xy} + \hat{\mathbf{x}}\hat{\mathbf{z}}G_{xz} \\ &+ \hat{\mathbf{y}}\hat{\mathbf{x}}G_{yx} + \hat{\mathbf{y}}\hat{\mathbf{y}}G_{yy} + \hat{\mathbf{y}}\hat{\mathbf{z}}G_{yz} \\ &+ \hat{\mathbf{z}}\hat{\mathbf{x}}G_{zx} + \hat{\mathbf{z}}\hat{\mathbf{y}}G_{zy} + \hat{\mathbf{z}}\hat{\mathbf{z}}G_{zz}. \end{aligned}$$



# CHAPTER 1

## Introduction

---

*“The time has come,” the Walrus said,  
“To talk of many things;  
Of shoes—and ships—and sealing wax—  
Of cabbages—and kings—  
And why the sea is boiling hot—  
And whether pigs have wings.”*  
—Lewis Carroll, *Through the Looking-Glass*

This thesis addresses the electromagnetic inverse scattering problems, i.e., to reconstruct, from the scattered electromagnetic signal, the internal constitution of the domain of interest. We will cover both point-like and extended scatterers, and both full-data and phaseless-data measurements. This introductory chapter provides a general description of this subject.

### 1.1 What is inverse scattering problem?

According to the definition by Keller [1], two problems are inverse to each other if the formulation of each of them requires full or partial knowledge of the other.

The following two problems serve as a good illustrative example.

1. Given the density distribution of the earth, calculate the gravitational field due to the earth;
2. Infer the density distribution of the earth from the gravitational field due to the earth.

Both problems are formulated exactly by Newton's law of gravity, and the known information in one problem is just the unknown in the other, so they are inverse to each other.

Conventionally, one of these two problems is referred to as forward (direct) problem, and the other as inverse problem. Roughly speaking, the forward problem is to find the observable data (gravitational field, for example), given the model parameter (density distribution, for example); while the inverse problem is to the contrary, that is to find the model parameter (density distribution, for example), given the observable data (gravitational field, for example). Rigorously speaking, the identification of the direct and inverse problem is based on Hadamard's concept of the ill-posed problem, originating from the philosophy that a well-posed mathematical model for a physical problem must have three properties: uniqueness, existence, and stability. Of the two problems, the well-posed one is referred to as the forward problem, and the ill-posed one as the inverse problem.

The forward and inverse scattering problems are related to the physical phenomenon of electromagnetic scattering, which is illustrated in Fig. 1.1. The incident electromagnetic wave is scattered by the objects, and the scattered electromagnetic signal (field or intensity) is related to the internal electric characteristic of the domain. The forward scattering problem is to determine



the scattered electromagnetic signal basing on the characteristics of the scatterer. The inverse scattering problem is inverse to the direct scattering problem, i.e., to determine the characteristics of an object (its shape, internal structure, etc.) from measurement data of scattered electromagnetic signal.

The inverse scattering technique is one of the most important approaches for attaining a quantitative description of the electrical and geometrical characteristics of the scatterer, and has found vast number of applications, such as echolocation, geophysical survey, remote sensing, nondestructive testing, biomedical imaging and diagnosis, quantum field theory, and military surveillance.

In view of the fact that the inversion method ought to be designed in accordance to the characteristics of the specific problem, we necessarily classify inverse scattering problems in terms of the categories of the scatterers or the measurement data. If the scatterer's size is much smaller than the wavelength, such scatterer is referred to as the point-like scatterer. In contrast, the extended scatterer is of the size which is comparable to or larger than the wavelength of the electromagnetic wave. If the measured data of scattered electromagnetic signal contains both intensity (or amplitude) and phase information, the problem is a full data (FD) inverse scattering problem. Under certain circumstances, however, acquiring the phase information of the measured electromagnetic field becomes a more formidable and more expensive task, compared with obtaining the amplitude information of the field. As a matter of fact, it has been reported in [2–4] that the accuracy of the measured phase cannot be guaranteed for frequencies higher than tens of gigahertz. If the phase information of the scattered field is unavailable, it is a phaseless data (PD) inverse scattering problem.

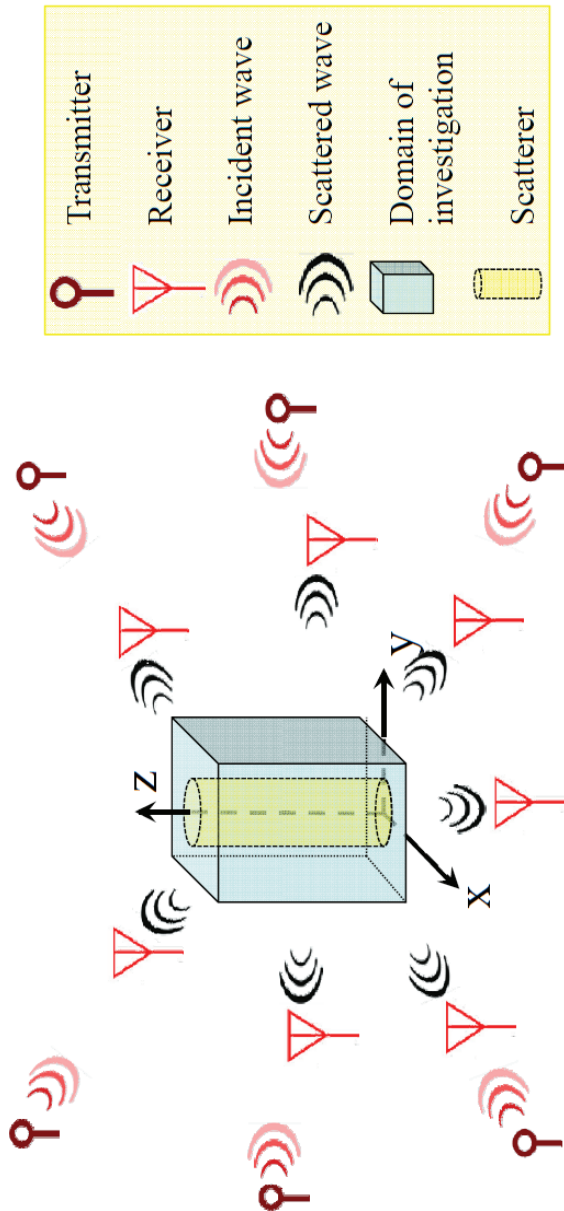


Figure 1.1: Setup for Inverse Scattering Experiment

## 1.2 Review of the approaches to inverse scattering problems

Instead of considering all possible inverse scattering approaches, we shall focus our review on a selection relevant to our project scope.

### 1.2.1 Inversion methods for full-data measurement

#### 1.2.1.1 Inversion methods for extended scatterers

The inverse scattering problems concerning extended scatterers, i.e. the scatterers whose dimensions are comparable to the wavelength of the illuminating electromagnetic wave, requires to reconstruct the electrical and geometrical characteristics of the scatterers from the scattered signal (field or intensity).

It is well known that the challenge of the inverse scattering problem arises from its property of being ill-posed. By Hadamard's definition [5], a problem is ill-posed if its solution meets at least one of the three conditions: nonexistence, non-uniqueness, instability. The existence of the solution has been mathematically proven in [6]. The non-uniqueness of the inverse scattering under single incidence can be perfectly overcome by multiple incidence [6]. The instability, unfortunately, cannot be completely eliminated, even though it can be relieved to some extent by applying certain regularization scheme, such as the Tikhonov regularization method [5–11], the multiplicative regularization scheme [12–14], and the truncated singular value decomposition [15–17].

Another obstacle to an easy solution of the inverse scattering problem is the nonlinearity relationship between the scattered field and the relative permittivity of the scatterers [6, 18]. In order to overcome the nonlinearity which exacerbates

the difficulty of finding the solution, approximate inversion methods have been proposed and found many practical applications. In these approximate methods, the scattered field is approximated by the linear functional of the scatterer, and consequently the inversion problem is notably simplified.

One way of obtaining the linear relation is to use the incident electromagnetic wave at sufficiently high frequency, so that its traveling can be described by a ray-like model, and the multi-path effects can be neglected. For such high frequency wave, the phase delay and the amplitude attenuation is linearly related to the scatterer's property[18]. The X-ray computed tomography (CT) [19] is a practical example of this approach, where the reconstruction is conducted using the back-projection algorithm with great success.

At lower frequencies, the straight-line ray model is not applicable, and the diffraction effect cannot be omitted. Some solutions to such problems apply the Born approximation and Rytov approximation model [20] to linearize the problem. Both of these linear approximations require the contrast between the scatterers and the background is small, while the former is more suitable at low frequencies, and the latter at higher frequencies. A representative iterative method of this sort is the Born iterative method (BIM) [21, 22], where the Born approximation is used to approximate the total field with the incident field.

Born approximation is also employed in distorted Born iterative method (DBIM) [9, 23, 24], which is a full-wave method, and thus does not belong to the category of linear methods, such as BIM. From the point view of algorithm, the difference between BIM and DBIM is that the Green's function used in DBIM is updated in each iteration, but it is not so in BIM. This difference causes the DBIM

to converge faster with lower error estimate, but BIM is more robust. An obvious drawback of BIM and DBIM is that each step of the iteration requires the solution of a forward or direct problem, which is computationally expensive for practical applications.

In the framework of nonlinear scattering model, such as the source type integral equation (STIE), some researchers have successfully cast the inverse scattering as an optimization problem where a nonlinear functional is minimized. One method of this sort is the modified gradient method [25], which is inspired by the over-relaxation method in solving the forward scattering problem. In this method, the nonlinearity relationship is retained, and the errors in both the field equation and in data equation are minimized by updating simultaneously the field and the contrast. Though inspired by the modified gradient method [25], the contrast source inversion (CSI) method [14, 26–28] distinguishes itself in the sense that the contrast sources (induced current) and the contrast itself are alternatively updated in each step of iteration. It is reported that the CSI method outperforms the modified gradient method in terms of computational speed and memory requirement and the readiness of accommodating a priori information [14, 26–28]. The subspace-based optimization method (SOM) was proposed in [29], and has been found to be rapidly convergent, robust against noise, and able to reconstruct scatterers with complicated shapes. SOM was inspired by the multiple signal classification (MUSIC) algorithm [7, 30, 31] and the two-step least squares method [32, 33]. The essence of SOM is that the contrast source is partitioned into the deterministic portion and the ambiguous portion. The former is readily obtained by the spectrum analysis, while the latter can be determined by various optimization means.

Boundary integral formalism is a framework frequently employed for reconstructing the shape of homogeneous objects in homogeneous background. In this formulation, the global optimization techniques are employed to reconstruct scatterers' boundary, including the well known generic algorithm [4, 34–37], differential evolution strategy [38–41], simulated annealing [42], Tabu list [34], etc. These methods do not require the analytical formulation of the cost functional and of its gradient, but normally consume noticeably long computational time and can only produce a quasi-local solution instead of a truly global optimum, given finite CPU time in reality. In addition, some researchers couple the line-search optimization algorithms with the equivalent boundary integral formalism to minimize a cost function, so as to reconstruct the boundary of scatterers [43–45]. Furthermore, the level set technique [46] is also applied in the equivalent boundary integral model, which exhibits the potential to use the limited amount of available data to directly reconstruct scatterers for certain structures or features and to accordingly incorporate available prior information into the reconstruction.

There are some other important noteworthy methods for reconstructing extended scatterers. The iterative multi-scaling approach [47] belongs to the family of multi-resolution algorithms [48], which employs a non-uniform discretization of the domain of interest to achieve the optimal trade-off between the achievable spatial resolution accuracy and the limited amount of information collected during the data acquisition. For the real-time detection of buried objects and also for large values of the contrast function, the learning-by-examples techniques [49–51] have been shown to be very effective and attractive methods to avoid the necessity of large computational resources, in the presence of either single-illumination

or multi-illumination acquisition systems, which have been successfully adopted in the framework of inverse scattering problems. The qualitative approaches, such as the MUSIC algorithm and the linear sampling method (LSM), are also implemented with notable computational speed and very little a priori information for detecting efficiently the scatterer's support or to locate the scatterers without recourse to nonlinear optimization methods.

### **1.2.1.2 Inversion methods for point-like scatterers**

Point-like scatterers are conventionally defined as the scatterers whose dimensions are so much smaller than the wavelength of the illuminating electromagnetic wave that it permits a long-wavelength approximation [52]. As a matter of fact, when solving numerically inverse scattering problems for point-like scatterers, we usually assume that each scatterer occupies a single subunit of discretization. If the number of detectors is more than the number of scatterers, as is normally the case, a one-to-one mapping exists between the induced currents and the scattered fields, which guarantees fortunately that imaging point-like scatterers is a mathematically well-posed problem. However, we still have to tackle the difficulty of inverse scattering of point-like scatterers which mainly arises in the inherent nonlinearity.

For certain practical applications, it suffices to retrieve only the information regarding the locations of the point-like scatterers, which is therefore referred to as the qualitative imaging problem. The focusing techniques provide one way of qualitatively imaging point-like scatterers. As an example, the DORT, which is the French acronym for Decomposition of the Time Reversal Operator (Décomposition de l'Opérateur de Retournement Temporel) [53–67], takes advantage of the

invariance of wave propagation under time reversal. It is a selective detection and focusing technique, i.e., it focuses synthetic waves at the point of interest. In this method, an array of transceivers are utilized to measure the inter-element impulse responses of each pair of transceivers in the array. As the result of the measurement, the time reversal operator is generated. This operator is then diagonalized and the analysis of its eigenvectors provides the internal information of the domain of investigation. Another representative focusing technique is the synthetic aperture focusing technique (SAFT) [68, 69], which was originally proposed to improve the image quality of a fixed-focus imaging system. In SAFT, the pulse-echo measurements are conducted at multiple transceiver locations. Then, the measurement data are processed (specifically, delayed and summed) to generate a map of the domain of interest. The applicability of DORT and SAFT is limited to the situations where the targets are well-resolved, where the antenna array is not sparse, and where the antennas are regularly arranged. In contrast, the multiple signal classification (MUSIC) method exhibits superior performance in situations that are too harsh for DORT or SAFT. The MUSIC method is an improvement of the Pisarenko's method [70], based on the idea of using average value to enhance the performance of the Pisarenko estimator. In MUSIC, we analyze the eigen-space to estimate the the frequency content of a signal or autocorrelation matrix. It has been utilized to address the electromagnetic inverse scattering problem for no more than a decade, firstly for the scalar wave and 2-D scenario [71, 72], and later extended to the vectorial wave and 3-D scenario [31, 33, 73–79].

In cases where a qualitative imaging is not sufficient, people demand



quantitative imaging of scatterers, i.e., both the location and the electrical characteristic of the scatterers. References [30, 32, 80] provide noniterative methods for obtaining scattering strengths of point targets, after locating the targets with MUSIC in advance. Noticing the sparsity in the signal to be reconstruct, some researchers proposed a number of compressive-sensing-based approaches to the inverse scattering problems of point-like scatterers by exploiting either basis pursuit techniques [81–83] or Bayesian approaches [84–86].

### **1.2.1.3 A brief introduction to fast forward scattering algorithms**

In the course of inverse scattering, one needs to compute repeatedly the forward solutions. For practical large-scale problems, for instance, a large 3D inverse scattering problem with objects embedded in either homogeneous medium or in layered media, this need usually imposes a very heavy burden in both CPU time and memory consumption. To ameliorate this problem, some fast algorithms are often applied as a forward solver within the inversion scheme. During the past two decades, there have been a large number of substantial techniques published on fast algorithms expediting the procedure of forward scattering. In this thesis, however, we use straightforward CDM and MoM, instead of incorporating these accelerating algorithms into the inversion scheme, since fast forward solvers are not the main focus of this thesis and may prevent the readers from judging clearly and fairly the performance of only the core idea of the inversion algorithm. Nonetheless a brief review of a few important accelerating algorithms, such as the fast multipole method (FMM) and conjugate gradient fast Fourier transform (CG-FFT), are still mention-worthy, in view of their practical significance.

The fast multipole method (FMM) was proposed to solve the integral equation

of scattering for Helmholtz problems [87], and was later generalized to the multilevel fast multipole algorithm (MLFMA) [88, 89]. The FMM and its hierarchical extension MLFMA, provide an efficient way for computing large-scale forward electromagnetic scattering problems, with the computational complexity scaling linearly with the number of scattering elements for volumetric scatterers [90, 91]. The conjugate gradient (CG) method combined with the fast Fourier transform (FFT) is another efficient means frequently applied as a fast forward scattering solver for large-scale problems [90, 92, 93], where CG algorithm is an efficient method to solve linear system equations, and FFT is used to evaluate rapidly the cyclic convolution and the cyclic correlation, so the burden of Sommerfeld integrals' evaluation is reduced to a minimum.

### **1.2.2 Inversion methods for phaseless-data measurement**

One of the severe limitations of the aforementioned approaches lies in the need to measure both the amplitude (intensity) and the phase of the scattered fields, and that is why these methods are conventionally referred to as full-data inverse scattering approaches. It is commonly acknowledged that phase is generally more difficult to measure than amplitude. As a matter of fact, researchers have observed [2, 3, 94] that the accuracy of phase measurements cannot be guaranteed for operating frequencies approaching the millimeter-wave band and beyond, due to the fact that the phase data is more prone to noise corruption during measurement than the amplitude data. Consequently, the adoption of phaseless (intensity-only) inverse scattering techniques is mandatory at optical frequencies, and strongly suggested at microwave and millimeter wave frequencies. Despite the lack of phase information compounded by marked ill-posedness and nonlinearity, the phaseless

inverse scattering problem is still solvable, either by the indirect approach (phase retrieval) or by the direct approach.

As rigorously elaborated in [95, 96], the physical principle of the indirect approach mainly involves two important concepts: (1) the minimally redundant finite-dimensional representation of the scattered fields; (2) the degrees of freedom of the scattered fields as a function of the incidence and the observation variables, which indicates the maximum amount of information on the scatterer that can be extracted from scattering measurements. Specifically, the indirect approach splits the problem into two steps [97–99]. In the first step, the scattered field (essentially the phase information) is estimated from the measurement of the intensity of the total field usually in an iterative manner, so as to convert a phaseless inverse scattering problem to a full-data inverse scattering problem. After that, as the second step, various full-data inverse scattering methods, which have been introduced in previous sections, can be readily adopted to reconstruct from both amplitude and phase information. The indirect approaches have been successfully exploited to address the phaseless inverse scattering problems, as reported in [97] for synthetic data on a closed curve, and then in [98] for synthetic data on open lines, and also in [99] for experimental data.

In contrast to the two-step indirect approach, the direct approach generates the reconstruction straightforwardly from the measured amplitude (intensity). Actually, most direct approaches to phaseless inverse scattering problems were extended from their counterparts for the full-data inverse scattering problems. In the context of diffraction tomography (DT), for instance, the original algorithms are based on both amplitude and phase information. It was extended later

to the phaseless case in [100], where, given weak scatterers, the the Rytov approximation is used to generate a linear mapping from the index perturbation of the object to the phase. Similarly, the distorted Born iterative method (DBIM) inspired the proposition of the distorted Rytov iterative method with phaseless data (PD-DRIM) [101, 102], for both lossy and lossless objects. The contrast source inversion (CSI) and multiplicative regularized CSI (MRCSI) methods, which were originally developed for full-data inverse scattering, have been extended to the phaseless inverse scattering problem [103, 104] so as to obviate the need for measuring phase. In this resultant customized algorithms, referred to as phaseless-data contrast source inversion (PD-CSI) and the phaseless-data multiplicative regularized contrast source inversion (PD-MRCSI), the term of the cost function regarding the field equation has been redefined accordingly. It was reported that the initial guess provided by the back-projection algorithm is necessary for rapid convergence and correct result for these two methods. Whereas the original version of the SOM outlined in [29, 105–107] requires the full set of amplitude and phase measurements for the scattered fields, a phaseless data version of the SOM [108] (referred to as PD-SOM) is afterwards proposed to handle inverse scattering problems without recourse to phase measurements. Furthermore, in the emerging framework of compressive sensing, we successfully formulate the intrinsically nonlinear phaseless inverse scattering problem for point-like scatterers, and solve it by convex programming [109].

## 1.3 Mathematical and physical preliminaries

This section is intended to be a brief yet self-contained introduction of some useful mathematical and physical knowledge, which is to be heavily involved in succeeding chapters. We refer interested readers to [18, 110–118] for a detailed treatment.

### 1.3.1 Maxwell’s equations and constitutive relationships

The four Maxwell’s equations first appeared in the famous paper “A Dynamical Theory of the Electromagnetic Field”, written by James Clerk Maxwell, published in 1865. They describe in full generality the laws of classical electrodynamics, which can be viewed as a limit of latter-developed quantum electrodynamics for small momentum and energy transfers, and large average numbers of virtual or real photons [111]. The Maxwell’s equations in differential and integral forms are given in Eq. (1.1) and Eq. (1.2), respectively.

$$\nabla \times \mathbf{H} = \mathbf{J} + \frac{\partial \mathbf{D}}{\partial t} \quad \text{Ampère’s Law} \quad (1.1a)$$

$$\nabla \times \mathbf{E} = -\frac{\partial \mathbf{B}}{\partial t} \quad \text{Faraday’s Law} \quad (1.1b)$$

$$\nabla \cdot \mathbf{D} = \rho \quad \text{Coulomb’s Law} \quad (1.1c)$$

$$\nabla \cdot \mathbf{B} = 0 \quad \text{Gauss’s Law} \quad (1.1d)$$

$$\oint_{\partial S} \mathbf{H} \cdot d\mathbf{l} = I_{f,S} + \frac{\partial \Phi_{D,S}}{\partial t} \quad \text{Ampère's Law} \quad (1.2a)$$

$$\oint_{\partial S} \mathbf{E} \cdot d\mathbf{l} = -\frac{\partial \Phi_{B,S}}{\partial t} \quad \text{Faraday's Law} \quad (1.2b)$$

$$\oiint_{\partial V} \mathbf{D} \cdot d\mathbf{A} = Q_f(V) \quad \text{Coulomb's Law} \quad (1.2c)$$

$$\oiint_{\partial V} \mathbf{B} \cdot d\mathbf{A} = 0 \quad \text{Gauss's Law} \quad (1.2d)$$

where  $\mathbf{D}$  is electric displacement;  $\mathbf{E}$  is the electric field strength;  $\mathbf{B}$  is the magnetic flux density;  $\mathbf{H}$  is the magnetic field strength;  $\mathbf{J}$  is the electric current density;  $\Phi_{D,S}$  is the electric flux;  $\Phi_{B,S}$  is the magnetic flux;  $I_{f,S}$  is the electric current; and  $Q_f$  is the electric charge.

In addition to Maxwell's equations, we also need the constitutive relationships describing the characteristics of the medium in which the field and wave exist. For anisotropic medium, the constitutive relationship is shown in Eq. (1.3).

$$\mathbf{D} = \bar{\bar{\epsilon}} \cdot \mathbf{E} \quad (1.3)$$

$$\mathbf{B} = \bar{\bar{\mu}} \cdot \mathbf{H}$$

Most problems studied in this thesis consider only the case, where the permittivity tensor of anisotropic medium in principal system is described by  $\bar{\bar{\epsilon}} = \text{diag}[\epsilon_x, \epsilon_y, \epsilon_z]$ , and the permeability tensor is replaced by a scalar  $\mu$ .

$$\mathbf{D} = \text{diag}[\epsilon_x, \epsilon_y, \epsilon_z] \cdot \mathbf{E} \quad (1.4)$$

$$\mathbf{B} = \mu \mathbf{H}$$

In some problems, we will consider only the simple isotropic media, which is described by

$$\mathbf{D} = \epsilon \mathbf{E} \quad (1.5)$$

$$\mathbf{B} = \mu \mathbf{H}$$

### 1.3.2 Helmholtz equations in homogeneous media

In this section, we solve 1-D, 2-D, and 3-D Helmholtz equations in homogeneous media, with plane, line, and point sources, respectively. The solutions are useful in the our later derivation of Green's function.

#### 1.3.2.1 1-D Helmholtz equations with plane source

Consider the 1-D Helmholtz equation Eq. (1.6) about  $f(z)$  in homogeneous media,

$$\left(\frac{d^2}{dz^2} + k^2\right)f(z) = -\delta(z), \quad (1.6)$$

where the  $\delta(z)$  is plane source on the  $xy$  plane.

When  $z \neq 0$ ,  $\delta(z) = 0$ , and the equation becomes

$$\left(\frac{d^2}{dz^2} + k^2\right)f(z) = 0.$$

Its general solution is  $f(z) = Ae^{ikz} + Be^{-ikz}$ , where  $A$  and  $B$  are constants. In view of the physical facts that the wave propagates in  $+z$  direction when  $z > 0$ , and in  $-z$  direction when  $z < 0$ , we can give the solution as  $f(z) = Ce^{ik|z|}$ , where  $C$  is the constant to be determined.

Now take the integral of the two sides of Eq. (1.6) in the interval  $(-\Delta, \Delta)$ , and let  $\Delta \rightarrow 0$ . The right side becomes

$$\lim_{\Delta \rightarrow 0} \int_{-\Delta}^{\Delta} -\delta(z) dz = -1.$$

The left hand side becomes

$$\lim_{\Delta \rightarrow 0} \int_{-\Delta}^{\Delta} \left(\frac{d^2}{dz^2} + k^2\right)Ce^{ik|z|} dz = 2Cik.$$

Finally, we get  $C = \frac{i}{2k}$ , and the solution  $f(z) = \frac{i}{2k}e^{ik|z|}$ .

### 1.3.2.2 2-D Helmholtz equations with line source

Consider the 2-D Helmholtz equation Eq. (1.7) about  $f(x, y)$  in homogeneous media,

$$(\nabla_t^2 + k^2)f(x, y) = -\delta(x)\delta(y), \quad (1.7)$$

where the  $\nabla_t = \frac{\partial^2}{\partial x^2} + \frac{\partial^2}{\partial y^2}$ , and  $\delta(x)\delta(y)$  is the line source.

Due to the obvious  $\phi$  symmetry, and the identity  $\delta(x)\delta(y) = \frac{\delta(\rho)}{2\pi\rho}$ , we can transform Eq. (1.7) to Bessel equation of zeroth order Eq. (1.8)

$$\left[ \frac{1}{\rho} \frac{d}{d\rho} \left( \rho \frac{d}{d\rho} \right) + k^2 \right] f(\rho) = -\frac{\delta(\rho)}{2\pi\rho}. \quad (1.8)$$

For  $\rho \neq 0$ , this equation becomes

$$\left[ \frac{1}{\rho} \frac{d}{d\rho} \left( \rho \frac{d}{d\rho} \right) + k^2 \right] f(\rho) = 0.$$

In view of the fact that there is a singularity at  $\rho = 0$  and the wave must be propagating outward, we find the solution to be  $f(\rho) = CH_0^{(1)}(k\rho)$ , where  $C$  is a constant to be determined.

Now take the integral of the two sides of Eq. (1.8) in the circular region (radius is  $\Delta$ ) and let  $\Delta \rightarrow 0$ . The right side becomes

$$\lim_{\Delta \rightarrow 0} \int_0^{2\pi} \int_0^\Delta -\frac{\delta(\rho)}{2\pi\rho} \rho \, d\phi d\rho = -1.$$

The left hand side becomes

$$\lim_{\Delta \rightarrow 0} \int_0^{2\pi} \int_0^\Delta \left[ \frac{1}{\rho} \frac{d}{d\rho} \left( \rho \frac{d}{d\rho} \right) + k^2 \right] f(\rho) \rho \, d\phi d\rho = 4iC.$$

In the above derivation, the asymptotic property of Hankel's function is used,



$H_0^{(1)}(\xi) = \frac{2i}{\pi} \ln(\xi)$ . Finally, we get  $C = \frac{i}{4}$ , and the solution  $f(\rho) = \frac{i}{4} H_0^{(1)}(k\rho)$ .

### 1.3.2.3 3-D Helmholtz equations with point source

Consider the 3-D Helmholtz equation Eq. (1.9) about  $f(x, y, z)$  in homogeneous media,

$$(\nabla^2 + k^2)f(x, y, z) = -\delta(x)\delta(y)\delta(z), \quad (1.9)$$

where the  $\nabla^2 = \frac{\partial^2}{\partial x^2} + \frac{\partial^2}{\partial y^2} + \frac{\partial^2}{\partial z^2}$ , and  $\delta(x)\delta(y)\delta(z)$  is the point source.

Due to the obvious  $\phi$  and  $\theta$  symmetry, and the identity  $\delta(x)\delta(y)\delta(z) = \frac{\delta(r)}{4\pi r^2}$ , we transform Eq. (1.9) to Eq. (1.10)

$$\left[ \frac{1}{r^2} \frac{d}{dr} \left( r^2 \frac{d}{dr} \right) + k^2 \right] f(r) = -\frac{\delta(r)}{4\pi r^2}. \quad (1.10)$$

For  $r \neq 0$ , this equation becomes

$$\left[ \frac{1}{r^2} \frac{d}{dr} \left( r^2 \frac{d}{dr} \right) + k^2 \right] f(r) = 0.$$

It is easy to find the general solution to the above equation to be  $f(r) = A \frac{e^{-ikr}}{r} + B \frac{e^{ikr}}{r}$ , where  $A$  and  $B$  are constants. Since the wave must be propagating outward, the solution should be  $f(r) = C \frac{e^{ikr}}{r}$ , where  $C$  is a constant to be determined.

Now take the integral of the two sides of Eq. (1.10) in the sphere region (radius is  $\Delta$ ) and let  $\Delta \rightarrow 0$ . The right side becomes

$$\lim_{\Delta \rightarrow 0} \int_0^\pi \int_0^{2\pi} \int_0^\Delta -\frac{\delta(r)}{4\pi r^2} d\theta d\phi dr = -1.$$

The left hand side becomes

$$\lim_{\Delta \rightarrow 0} \int_0^\pi \int_0^{2\pi} \int_0^\Delta \left[ \frac{1}{r^2} \frac{d}{dr} \left( r^2 \frac{d}{dr} \right) + k^2 \right] f(r) d\theta d\phi dr = -4\pi C.$$

Finally, we get  $C = \frac{1}{4\pi}$ , and the solution  $f(\rho) = \frac{1}{4\pi} \frac{e^{ikr}}{r}$ .

### 1.3.3 Dyadic Green's function in homogeneous media

Throughout this thesis, ‘‘Green’s function’’ means ‘‘field due to a point or line source’’. The ‘‘dyadic (tensor) Green’s function’’ provides an attractive way of compact formulation of some electromagnetic problems, by indicating the linear relationship between a vector field and a vector current source.

In this section, we give the derivation of 1-D Green’s function, as well as 2-D and 3-D dyadic Green’s functions, starting from Eq. (1.1). We introduce the vector and scalar potentials  $\mathbf{A}$  and  $\Phi$  defined as  $\mathbf{B} = \nabla \times \mathbf{A}$  and  $\mathbf{E} = -\frac{\partial \mathbf{A}}{\partial t} - \nabla \Phi$ , respectively, and substitute them into Eq. (1.1). For time-harmonic fields, an equivalent set of equations are found to be

$$\nabla \cdot \mathbf{A} - \frac{i\omega}{c^2} \Phi = 0 \quad \text{Lorenz gauge} \quad (1.11a)$$

$$\nabla^2 \Phi + k^2 \Phi = -\rho/\epsilon_0 \quad (1.11b)$$

$$\nabla^2 \mathbf{A} + k^2 \mathbf{A} = -\mu_0 \mathbf{J} \quad (1.11c)$$

where  $k = \omega/c$  is the wave number.

The above equation about  $\mathbf{A}$  is clearly the Helmholtz equations whose solution has been given in 1.3.2, so we get

$$\mathbf{A}(\mathbf{r}) = \iiint \frac{e^{ik|\mathbf{r}-\mathbf{r}'|}}{4\pi|\mathbf{r}-\mathbf{r}'|} \mu_0 \mathbf{J}(\mathbf{r}') d\mathbf{r}'.$$

It follows that the electric field is

$$\mathbf{E}(\mathbf{r}) = i\omega\mu_0 \iiint (\bar{\bar{\mathbf{I}}} + \frac{1}{k^2}\nabla\nabla) \cdot \frac{e^{ik|\mathbf{r}-\mathbf{r}'|}}{4\pi|\mathbf{r}-\mathbf{r}'|} \mathbf{J}(\mathbf{r}') d\mathbf{r}'.$$

It is convenient to introduce the dyadic Green's function

$$\bar{\bar{\mathbf{G}}}(\mathbf{r}, \mathbf{r}') = (\bar{\bar{\mathbf{I}}} + \frac{1}{k^2}\nabla\nabla) \frac{e^{ik|\mathbf{r}-\mathbf{r}'|}}{4\pi|\mathbf{r}-\mathbf{r}'|},$$

so the electric field can be expressed in a compact form

$$\mathbf{E}(\mathbf{r}) = i\omega\mu_0 \iiint \bar{\bar{\mathbf{G}}}(\mathbf{r}, \mathbf{r}') \cdot \mathbf{J}(\mathbf{r}') d\mathbf{r}'.$$

Suppose the source is invariant along the  $\hat{z}$  direction, the three-fold integral can be reduced by removing the integral over  $z$ -axis by using the identity,

$$\int_{z=-\infty}^{\infty} \frac{e^{ik|\mathbf{r}-\mathbf{r}'|}}{4\pi|\mathbf{r}-\mathbf{r}'|} = \frac{i}{4} H_0^{(1)}(k\rho).$$

In transverse magnetic (TM) case, the source is invariant along the  $\hat{z}$ -direction and has only the  $\hat{z}$  component. Using the above identity, the TM Green's function can be derived as

$$\bar{\bar{\mathbf{G}}}_{TM}(\mathbf{r}, \mathbf{r}') = \frac{i}{4} H_0^{(1)}(k\rho).$$

In transverse electric (TE) case, the source is invariant along the  $\hat{z}$ -direction and has only the  $\hat{x}$  and  $\hat{y}$  component. Using the identity, we can also derive the TE Green's function as

$$\begin{aligned} \bar{\bar{\mathbf{G}}}_{TE}(\mathbf{r}, \mathbf{r}') = & \hat{\mathbf{x}}\hat{\mathbf{x}}g_{11} + \hat{\mathbf{x}}\hat{\mathbf{y}}g_{12} \\ & + \hat{\mathbf{y}}\hat{\mathbf{x}}g_{21} + \hat{\mathbf{y}}\hat{\mathbf{y}}g_{22} \end{aligned}$$

where

$$g_{11} = H_0^{(1)}(k_0|\mathbf{r} - \mathbf{r}'|) + H_2^{(1)}(k_0|\mathbf{r} - \mathbf{r}'|) \cos^2 \gamma - \frac{H_1^{(1)}(k_0|\mathbf{r} - \mathbf{r}'|)}{k_0|\mathbf{r} - \mathbf{r}'|},$$

$$g_{22} = H_0^{(1)}(k_0|\mathbf{r} - \mathbf{r}'|) + H_2^{(1)}(k_0|\mathbf{r} - \mathbf{r}'|) \sin^2 \gamma - \frac{H_1^{(1)}(k_0|\mathbf{r} - \mathbf{r}'|)}{k_0|\mathbf{r} - \mathbf{r}'|},$$

$$g_{12} = g_{21} = H_2^{(1)}(k_0|\mathbf{r} - \mathbf{r}'|) \sin \gamma \cos \gamma,$$

$$\gamma = \tan^{-1} \left( \frac{y - y'}{x - x'} \right).$$

### 1.3.4 Green's Function for cylindrical geometry

The cylinder geometry is involved in the succeeding chapters and so we derive the Green's function for cylindrical structures in this section. First, consider the background where free space surrounds a cylinder with its center located at the origin  $(0, 0)$ . The radius of the cylinder is  $R$ , and its relative permittivity is  $\epsilon_r$ .

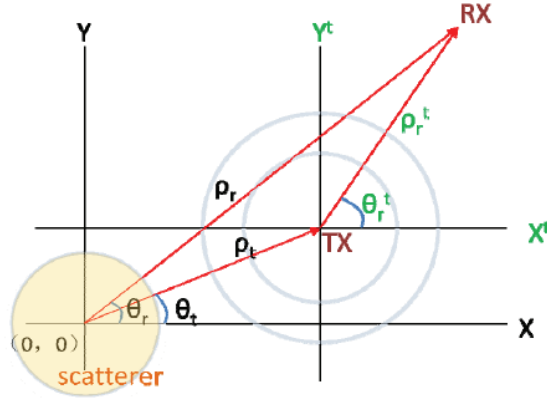


Figure 1.2: Illustration of Graf's addition theorem

Next, consider a transmitter (TX) located at  $\bar{r}_t = (\rho_t, \theta_t)$ , a receiver (RX) located at  $\bar{r}_r = (\rho_r, \theta_r)$ , both in terms of the original polar coordinate system (O) whose origin is at the center of the cylinder. Consider a shifted polar coordinate system (T) whose origin is at the position of TX. The location of RX with respect

to the coordinate system (T) is denoted as  $\bar{r}_r^t = (\rho_r^t, \theta_r^t)$ , where the superscript ‘t’ signifies that the origin of the frame of reference is TX, the origin of coordinates system (T). Obviously, we know that  $\bar{r}_r^t = \bar{r}_r - \bar{r}_t$ . The problem is this: Find Green’s Function for the following four situations in Table 1.1, respectively.

Table 1.1: Four types of Green’s function for cylinder background

N.O. of situation	Location of TX	Location of RX	Notation of Green’s Function
1	Inside cylinder	Inside cylinder	$G_{ii}(\rho_t, \theta_t, \rho_r, \theta_r)$
2	Inside cylinder	Outside cylinder	$G_{oi}(\rho_t, \theta_t, \rho_r, \theta_r)$
3	Outside cylinder	Inside cylinder	$G_{io}(\rho_t, \theta_t, \rho_r, \theta_r)$
4	Outside cylinder	Outside cylinder	$G_{oo}(\rho_t, \theta_t, \rho_r, \theta_r)$

Graf’s addition theorem expands a displaced cylinder harmonic as a linear superposition of the undisplaced cylinder harmonics. It will be repeatedly referred to, in particular, for a special case, which is given in Eq. (1.13) for the sake of convenience

$$H_0^{(1)}(k\rho_r^t) = \begin{cases} \sum_{n=-\infty}^{\infty} J_n(k\rho_t) \cdot e^{-in\theta_t} \cdot H_n^{(1)}(k\rho_r) \cdot e^{-in\theta_r}, & \text{if } \rho_t < \rho_r, \\ \sum_{n=-\infty}^{\infty} H_0^{(1)}(k\rho_t) \cdot e^{-in\theta_t} \cdot H_n^{(1)}(k\rho_r) \cdot e^{-in\theta_r}, & \text{if } \rho_r < \rho_t \end{cases} \quad (1.13)$$

Now we will derive Green’s function for situation 1 and situation 2 :  $G_{ii}(\rho_t, \theta_t, \rho_r, \theta_r)$  and  $G_{oi}(\rho_t, \theta_t, \rho_r, \theta_r)$ .

Green’s function is basically the electric field caused by a unitary current source. For the first and second situation, the source is put inside the cylinder. The field inside the cylinder due to the source is

$$E^{\text{inc}}(\rho, \theta) = -\frac{\omega\mu_0}{4} H_0^{(1)}(k_c\rho^t)$$

In this equation,  $k_c = \omega\sqrt{\mu_0\varepsilon_c} = \omega\sqrt{\mu_0\varepsilon_r\varepsilon_0}$  is the wave number inside the cylinder.

The field outside the cylinder is

$$E^{\text{out}}(\rho, \theta) = -\frac{\omega\mu_0}{4} \sum_{n=-\infty}^{\infty} b_n \cdot H_n^{(1)}(k_0\rho) \cdot e^{in\theta}$$

The field inside the cylinder due to scattering is

$$E^{\text{in}}(\rho, \theta) = -\frac{\omega\mu_0}{4} \sum_{n=-\infty}^{\infty} c_n \cdot J_n(k_c\rho) \cdot e^{in\theta}$$

Noting that the boundary condition to be matched is at  $\rho_r = R > \rho_t$ , we use Graf's addition theorem to expand  $E^{\text{inc}}$  as

$$\begin{aligned} E^{\text{inc}}(\rho, \theta) &= -\frac{\omega\mu_0}{4} H_0^{(1)}(k_c\rho^t) \\ &= -\frac{\omega\mu_0}{4} \sum_{n=-\infty}^{\infty} J_n(k\rho_t) \cdot e^{-in\theta_t} \cdot H_n^{(1)}(k\rho_r) \cdot e^{-in\theta_r} \\ &= -\frac{\omega\mu_0}{4} \sum_{n=-\infty}^{\infty} a_n \cdot H_n^{(1)}(k\rho_r) \cdot e^{-in\theta_r}. \end{aligned} \quad (1.14)$$

In the last expression,  $a_n = J_n(k\rho_t) \cdot e^{-in\theta_t}$ .

The boundary condition that the tangential electric and magnetic fields are continuous on the boundary yield

$$\begin{aligned} a_n \cdot H_n^{(1)}(k_c R) + c_n \cdot J_n(k_c R) &= b_n \cdot H_n^{(1)}(k_0 R) \\ a_n k_c \cdot H_n^{(1)'}(k_c R) + c_n k_c \cdot J_n'(k_c R) &= b_n k_0 \cdot H_n^{(1)'}(k_0 R) \end{aligned}$$

Solving the two equations, we obtain

$$b_n = a_n \frac{k_c \cdot H_n^{(1)}(k_c R) \cdot J_n'(k_c R) - k_c \cdot H_n^{(1)'}(k_c R) \cdot J_n(k_c R)}{k_c \cdot H_n^{(1)}(k_c R) \cdot J_n'(k_c R) - k_0 \cdot H_n^{(1)'}(k_0 R) \cdot J_n(k_c R)}$$

After calculating  $b_n$ , we can also get  $c_n$ .

$$c_n = \frac{b_n \cdot H_n^{(1)}(k_0 R) - a_n \cdot H_n^{(1)}(k_c R)}{J_n(k_c R)}$$

Finally, we get Green's functions for the first and second situations as follows.

$$\begin{aligned} G_{ii}(\rho_t, \theta_t, \rho_r, \theta_r) &= E^{\text{inc}}(\rho_r, \theta_r) + E^{\text{in}}(\rho_r, \theta_r) \\ &= -\frac{\omega\mu_0}{4} \sum_{n=-\infty}^{\infty} [a_n \cdot H_n^{(1)}(k_c \rho_r) + c_n \cdot J_n(k_c \rho_r)] \cdot e^{-in\theta_r} \end{aligned}$$

$$\begin{aligned} G_{oi}(\rho_t, \theta_t, \rho_r, \theta_r) &= E^{\text{out}}(\rho_r, \theta_r) \\ &= -\frac{\omega\mu_0}{4} \sum_{n=-\infty}^{\infty} b_n \cdot H_n^{(1)}(k_0 \rho_r) \cdot e^{-in\theta_r} \end{aligned}$$

By the similar token, we derive Green's function for situation 3 and situation 4:  $G_{io}(\rho_t, \theta_t, \rho_r, \theta_r)$  and  $G_{oo}(\rho_t, \theta_t, \rho_r, \theta_r)$ . The field outside the cylinder due to the source is

$$E^{\text{inc}}(\rho, \theta) = -\frac{\omega\mu_0}{4} H_0^{(1)}(k_0 \rho^t)$$

The field outside the cylinder due to scattering is

$$E^{\text{out}}(\rho, \theta) = -\frac{\omega\mu_0}{4} \sum_{n=-\infty}^{\infty} b_n \cdot H_n^{(1)}(k_0 \rho) \cdot e^{in\theta}$$

The field inside the cylinder due to scattering is

$$E^{\text{in}}(\rho, \theta) = -\frac{\omega\mu_0}{4} \sum_{n=-\infty}^{\infty} c_n \cdot J_n(k_c \rho) \cdot e^{in\theta}$$

In this equation,  $k_c = \omega\sqrt{\mu_0\varepsilon_c} = \omega\sqrt{\mu_0\varepsilon_r\varepsilon_0}$  is the wave number inside the cylinder.

Noting that the boundary condition to be matched is at  $\rho_r = R < \rho_t$ , we use Graf's addition theorem to expand  $E^{\text{inc}}$  as

$$\begin{aligned} E^{\text{inc}}(\rho, \theta) &= -\frac{\omega\mu_0}{4} H_0^{(1)}(k_0 \rho^t) \\ &= -\frac{\omega\mu_0}{4} \sum_{n=-\infty}^{\infty} H_n^{(1)}(k_0 \rho_t) \cdot e^{-in\theta_t} \cdot J_n(k_0 \rho) \cdot e^{-in\theta} \\ &= -\frac{\omega\mu_0}{4} \sum_{n=-\infty}^{\infty} a_n \cdot J_n(k_0 \rho) \cdot e^{-in\theta} \end{aligned}$$

In the last expression,  $a_n = H_n^{(1)}(k_0\rho_t) \cdot e^{-in\theta_t}$ .

The boundary condition that the tangential electric and magnetic fields are continuous on the boundary yield

$$\begin{aligned} b_n \cdot H_n^{(1)}(k_0R) + a_n \cdot J_n(k_0R) &= c_n \cdot J_n(k_cR) \\ b_n k_0 \cdot H_n^{(1)'}(k_0R) + a_n k_0 \cdot J_n'(k_0R) &= c_n k_c \cdot J_n'(k_cR) \end{aligned}$$

Solving the two equations, we obtain

$$\begin{aligned} b_n &= a_n \frac{k_0 \cdot J_n(k_cR) \cdot J_n'(k_0R) - k_c \cdot J_n'(k_cR) \cdot J_n(k_0R)}{k_c \cdot H_n^{(1)}(k_0R) \cdot J_n'(k_cR) - k_0 \cdot H_n^{(1)'}(k_0R) \cdot J_n(k_cR)} \\ c_n &= \frac{b_n \cdot H_n^{(1)}(k_0R) + a_n \cdot J_n(k_0R)}{J_n(k_cR)} \end{aligned}$$

Finally, we get Green's functions for the third and fourth situations as follows.

$$\begin{aligned} G_{oo}(\rho_t, \theta_t, \rho_r, \theta_r) &= E^{\text{inc}}(\rho_r, \theta_r) + E^{\text{in}}(\rho_r, \theta_r) \\ &= -\frac{\omega\mu_0}{4} \sum_{n=-\infty}^{\infty} [a_n \cdot J_n(k_0\rho_r) + b_n \cdot H_n^{(1)}(k_0\rho_r)] \cdot e^{-in\theta_r} \\ G_{io}(\rho_t, \theta_t, \rho_r, \theta_r) &= E^{\text{in}}(\rho_r, \theta_r) \\ &= -\frac{\omega\mu_0}{4} \sum_{n=-\infty}^{\infty} c_n \cdot J_n(k_c\rho_r) \cdot e^{-in\theta_r} \end{aligned}$$

### 1.3.5 Lippmann-Schwinger equation

In this section, we derive the Lippmann-Schwinger equation [5], which describes the electromagnetic scattering phenomenon. As shown in Fig. 1.3, we divide the domain of interest into two mutually-disjoint portions: the one occupied by the scatterers is  $V_{\text{scat}}$ , and the other one occupied by the background media (supposed to be free-space) is  $V_{\text{bg}}$ . The constitutive relationship is described by

$$\mathbf{D}(\mathbf{r}) = \begin{cases} \bar{\bar{\epsilon}}(\mathbf{r}) \cdot \mathbf{E}(\mathbf{r}), & \mathbf{r} \in V_{\text{scat}} \\ \epsilon_0 \mathbf{E}(\mathbf{r}), & \mathbf{r} \in V_{\text{bg}} \end{cases} \quad (1.15)$$



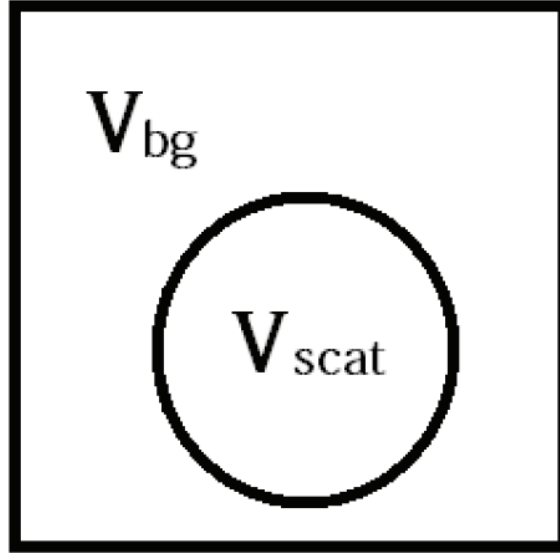


Figure 1.3: Dividing the domain of interest

From Maxwell's equations Eq. (1.1) and the above constitutive relationship Eq. (1.15), we get

$$\nabla \times \mathbf{E}(\mathbf{r}) - i\omega\mu_0\mathbf{H}(\mathbf{r}) = 0, \quad \mathbf{r} \in V_{bg} \cup V_{scat} \quad (1.16a)$$

$$\nabla \times \mathbf{H}(\mathbf{r}) - i\omega\varepsilon_0\mathbf{E}(\mathbf{r}) = 0, \quad \mathbf{r} \in V_{bg} \quad (1.16b)$$

$$\nabla \times \mathbf{H}(\mathbf{r}) - i\omega\varepsilon_0\bar{\bar{\varepsilon}}_r(\mathbf{r}) \cdot \mathbf{E}(\mathbf{r}) = 0, \quad \mathbf{r} \in V_{scat} \quad (1.16c)$$

Using the equivalence principle [113], Eq. (1.16) can be simplified by replacing the scatterers with equivalent induced polarization currents  $\mathbf{J}(\mathbf{r})$ . Thus, Eq. (1.16)

is reduced to Eq. (1.17)

$$\nabla \times \mathbf{E}(\mathbf{r}) - i\omega\mu_0\mathbf{H}(\mathbf{r}) = 0, \quad \mathbf{r} \in V_{bg} \cup V_{scat} \quad (1.17a)$$

$$\nabla \times \mathbf{H}(\mathbf{r}) - i\omega\varepsilon_0\mathbf{E}(\mathbf{r}) = \mathbf{J}(\mathbf{r}), \quad \mathbf{r} \in V_{bg} \cup V_{scat} \quad (1.17b)$$

where

$$\mathbf{J}(\mathbf{r}) = 0 \quad \mathbf{r} \in V_{bg} \quad (1.17c)$$

$$\mathbf{J}(\mathbf{r}) = -i\omega\varepsilon_0[\bar{\bar{\mathbf{I}}} - \bar{\bar{\varepsilon}}_r(\mathbf{r})] \cdot \mathbf{E}(\mathbf{r}) \quad \mathbf{r} \in V_{scat}. \quad (1.17d)$$

Solving Eq. (1.17) yields the Lippman-Schwinger integral equation Eq. (1.18),

$$\mathbf{E}(\mathbf{r}) = \mathbf{E}^{\text{inc}}(\mathbf{r}) + i\omega\mu_0 \iiint_{V_{scat}} \bar{\bar{\mathbf{G}}}(\mathbf{r}, \mathbf{r}') \cdot \mathbf{J}(\mathbf{r}') d\mathbf{r}', \quad \mathbf{r} \in V_{bg} \cup V_{scat}. \quad (1.18)$$

where  $\mathbf{E}^{\text{inc}}(\mathbf{r})$  is the solution of sourceless counterparts of the integral equation Eq. (1.17).

### 1.3.6 The method of moments (MoM)

The method of moments (MoM) is a numerical technique converting integral equations, such as the Lippmann-Schwinger equation Eq. (1.18), into a linear system that can be solved numerically using a computer. In this section, the method of moments (MoM) is derived from the Lippmann-Schwinger equation. We will consider only the anisotropic media and the weak form MoM (to be discussed shortly), since they are sufficient for the problems studied in this thesis. For the case of the general bianisotropic media and the strong form MoM, the readers are referred to [114].

In order to solve the Lippmann-Schwinger equation Eq. (1.18) numerically, the scatterer  $V_{scat}$  is discretized into a union of non-overlapping subunits  $V_m$  ( $m =$

$1, 2, \dots, N$ ), so that  $V_{scat} = \bigcup_{m=1}^N V_m$ . The volumetric capacity of  $V_m$  is  $v_m = \iiint_{V_m} d\mathbf{r}$ . Let  $\mathbf{r}_m$  be a distinguished point lying inside  $V_m$ , and let  $\mathbf{E}_m = \mathbf{E}(\mathbf{r}_m)$  be the actual field at  $\mathbf{r}_m$ .

Conventionally, we require

1.  $V_m$  is homogeneous,
2. the maximum linear extent  $2a_m$  of  $V_m$  is such that  $k_0 a_m < 0.1$ ,

so the long-wavelength approximation can be applied:  $\mathbf{E}(\mathbf{r}) = \mathbf{E}_m, \quad \forall \mathbf{r} \in V_m$ .

The difficulty in numerically solving the Lippmann-Schwinger equation Eq. (1.18) lies in the problem of the integral of dyadic Green's function in the source region. Fortunately the weak form approximation provided in [114] paves the way. Suppose  $V$  is electrically small enough for long-wavelength approximation and  $\mathbf{r}_0$  is a point inside  $V$ , we have Eq. (1.19),

$$\lim_{V \rightarrow 0} \iiint_V \overline{\overline{\mathbf{G}}}(\mathbf{r}, \mathbf{r}') \cdot \mathbf{J}(\mathbf{r}') d\mathbf{r}' \approx -\frac{1}{k_0^2} \overline{\overline{\mathbf{L}}} \cdot \mathbf{J}(\mathbf{r}_0) \quad (1.19)$$

where the evaluation of the depolarization dyadic  $\overline{\overline{\mathbf{L}}}$  is dependent on the shape of subunit. It is worth mentioning that the condition of infinitesimal principal volume ( $V \rightarrow 0$ ) coupled with an inhomogeneous limiting procedure may cause troubles in numerical calculations, and these troubles can be avoided by some alternative methods provided by some recent study [119], which considers a finite size principal volume instead of an infinitesimally small principal volume and does not contain the source dyadic term. The details about these recent development [119], however, is beyond the scope of this thesis. The results of  $\overline{\overline{\mathbf{L}}}$  for typical shapes are given in two tables provided by [115].

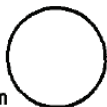
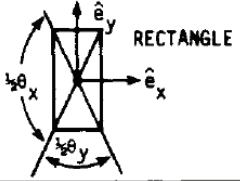
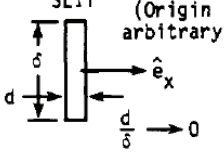
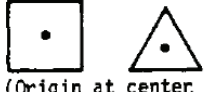
PRINCIPAL AREA	2-D SOURCE DYADIC $\overline{\overline{\mathbf{I}}}$
CIRCLE  (Origin and axes arbitrary)	$\frac{\overline{\overline{\mathbf{I}}}}{2}$
RECTANGLE 	$\frac{1}{2\pi}(\theta_x \hat{e}_x \hat{e}_x + \theta_y \hat{e}_y \hat{e}_y)$ $(\theta_x + \theta_y = 2\pi)$
SLIT (Origin arbitrary) 	$\hat{e}_x \hat{e}_x$
SQUARE AND EQUILATERAL TRIANGLE  (Origin at center, axes arbitrary)	$\frac{\overline{\overline{\mathbf{I}}}}{2}$

Figure 1.4: Evaluation of 2-D depolarization dyadic  $\overline{\overline{\mathbf{L}}}$  [115]

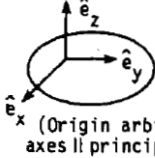
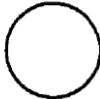
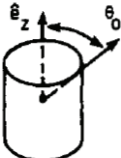
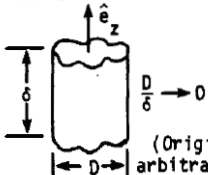
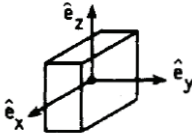
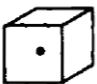
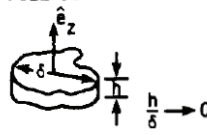
PRINCIPLE VOLUME	SOURCE DYADIC $\overline{\overline{\mathbf{L}}}$
<p>ELLIPSOID</p>  <p>(Origin arbitrary, axes    principal axes)</p>	$\frac{\overline{\overline{\mathbf{L}}}}{\epsilon_0} = L_1 \hat{e}_x \hat{e}_x + L_2 \hat{e}_y \hat{e}_y + L_3 \hat{e}_z \hat{e}_z$ $(L_1 + L_2 + L_3 = 1/\epsilon_0)$ <p><math>L_1, L_2, L_3</math> are the depolarizing factors [23], Sec. 3.27.</p>
<p>SPHERE</p>  <p>(Origin and axes arbitrary)</p>	$\frac{\overline{\overline{\mathbf{I}}}}{3}$
<p>RIGHT CIRCULAR CYLINDER</p>  <p>(Origin at center)</p>	$(1 - \cos \theta_0) \hat{e}_z \hat{e}_z + (1/2) \cos \theta_0 \overline{\overline{\mathbf{I}}}_t$
<p>THIN RIGHT CYLINDER</p>  <p>(Origin arbitrary)</p>	<p>Same as 2-D source dyadic for P.A. equal to cross section of cylinder P.V. (see Table II e.g., for a thin circular cylinder <math>\overline{\overline{\mathbf{L}}} = \overline{\overline{\mathbf{I}}}_t/2</math>).</p>
<p>RECTANGULAR PARALLELEPIPED</p>  <p>(Origin at center)</p>	$\frac{1}{4\pi} (\Omega_x \hat{e}_x \hat{e}_x + \Omega_y \hat{e}_y \hat{e}_y + \Omega_z \hat{e}_z \hat{e}_z)$ <p><math>(\Omega_x + \Omega_y + \Omega_z = 4\pi)</math>, <math>\Omega_x, \Omega_y,</math> and <math>\Omega_z</math> are twice the solid angle subtended by a side <math>\perp</math> to the x, y, and z direction respectively.</p>
<p>CUBE</p>  <p>(Origin at center, axes arbitrary)</p>	$\frac{\overline{\overline{\mathbf{I}}}}{3}$
<p>PILL BOX</p>  <p>(Origin arbitrary)</p>	$\hat{e}_z \hat{e}_z$

Figure 1.5: Evaluation of 3-D depolarization dyadic  $\overline{\overline{\mathbf{L}}}$  [115]

Now we are able to reduce the Eq. (1.18) to

$$\mathbf{E}_m = \mathbf{E}_m^{\text{inc}} - i\omega\mu_0 \frac{1}{k_0^2} \bar{\bar{\mathbf{L}}}_m \cdot \mathbf{J}_m + \sum_{\substack{n=1 \\ n \neq m}}^N i\omega\mu_0 \bar{\bar{\mathbf{G}}}_{m,n} \cdot \mathbf{J}_n, \quad m = 1, 2, \dots, N. \quad (1.20)$$

where  $\mathbf{E}_m^{\text{inc}} = \mathbf{E}^{\text{inc}}(\mathbf{r}_m)$ ,  $\mathbf{J}_m = \mathbf{J}(\mathbf{r}_m)$ ,  $\bar{\bar{\mathbf{G}}}_{m,n} = \bar{\bar{\mathbf{G}}}(\mathbf{r}_m, \mathbf{r}_n)$ .

Eq. (1.20) is then transformed to the compact linear system of MoM.

$$\mathbf{E}^{\text{inc}}(\mathbf{r}_m) = \sum_{n=1}^N \bar{\bar{\mathbf{A}}}_{m,n} \cdot \mathbf{E}(\mathbf{r}_n), \quad m = 1, 2, \dots, N, \quad (1.21)$$

where

$$\bar{\bar{\mathbf{A}}}_{m,m} = \bar{\bar{\mathbf{I}}} - \bar{\bar{\mathbf{L}}}_m \cdot [\bar{\bar{\mathbf{I}}} - \bar{\bar{\boldsymbol{\epsilon}}}_{r_m}], \quad m = 1, 2, \dots, N,$$

and for  $m \neq n$

$$\bar{\bar{\mathbf{A}}}_{m,n} = k_0^2 v_n \bar{\bar{\mathbf{G}}}_{m,n} \cdot [\bar{\bar{\mathbf{I}}} - \bar{\bar{\boldsymbol{\epsilon}}}_{r_m}], \quad m, n = 1, 2, \dots, N.$$

Once  $\mathbf{E}_m$  has been calculated,  $\mathbf{J}_m$  is determined using Eq. (1.17). Finally, the scattered field is computed as

$$\mathbf{E}^{\text{scat}}(\mathbf{r}) = i\omega\mu_0 \sum_{n=1}^N v_n \bar{\bar{\mathbf{G}}}(\mathbf{r}, \mathbf{r}_n) \cdot \mathbf{J}(\mathbf{r}_n). \quad (1.22)$$

### 1.3.7 The coupled dipole method (CDM)

In MoM, we consider  $\mathbf{E}(\mathbf{r}_n)$ , the actual field at the subunit  $V_n$ , while in the coupled dipole method (CDM), we consider  $\mathbf{E}^{\text{tot}}(\mathbf{r}_n)$ , which is interpreted as the field exciting the subunit  $V_n$ . As a matter of fact,  $\mathbf{E}^{\text{tot}}(\mathbf{r}_n)$  is the sum of the incident field and the scattered field from all the other subunits, and its linear relation with

$\mathbf{E}(\mathbf{r}_n)$  can be readily derived from Eq. (1.20) as shown in Eq. (1.23).

$$\begin{aligned}
\mathbf{E}_m^{tot} &= \mathbf{E}_m^{inc} + \sum_{\substack{n=1 \\ n \neq m}}^N i\omega\mu_0 \overline{\overline{\mathbf{G}}}_{m,n} \cdot \mathbf{J}_n \\
&= \mathbf{E}_m + i\omega\mu_0 \cdot \frac{1}{k_0^2} \overline{\overline{\mathbf{L}}}_m \cdot \mathbf{J}_m \\
&= \left[ \overline{\overline{\mathbf{I}}} + \overline{\overline{\mathbf{L}}}_m \cdot \left( \overline{\overline{\mathbf{I}}} - \overline{\overline{\boldsymbol{\varepsilon}}}_{r_m} \right) \right] \cdot \mathbf{E}_m \\
& \quad m = 1, 2, \dots, N.
\end{aligned} \tag{1.23}$$

Let  $\overline{\overline{\mathbf{P}}}_m = \left[ \overline{\overline{\mathbf{I}}} + \overline{\overline{\mathbf{L}}}_m \cdot \left( \overline{\overline{\mathbf{I}}} - \overline{\overline{\boldsymbol{\varepsilon}}}_{r_m} \right) \right]$ . So  $\mathbf{J}$  is also linearly associated with  $\mathbf{E}^{tot}$ ,

$$\mathbf{J}_m = i\omega\varepsilon_0 \left( \overline{\overline{\mathbf{I}}} - \overline{\overline{\boldsymbol{\varepsilon}}}_{r_m} \right) \cdot \overline{\overline{\mathbf{P}}}_m^{-1} \cdot \mathbf{E}_m^{tot}. \tag{1.24}$$

Now we are able to get the linear system of CDM Eq. (1.25), which seems similar to Eq. (1.21)

$$\mathbf{E}_m^{inc} = \sum_{n=1}^N \overline{\overline{\mathbf{Q}}}_{m,n} \cdot \mathbf{E}_n^{tot}, \quad m = 1, 2, \dots, N, \tag{1.25}$$

where

$$\overline{\overline{\mathbf{Q}}}_{m,m} = \overline{\overline{\mathbf{I}}},$$

and for  $m \neq n$

$$\overline{\overline{\mathbf{Q}}}_{m,n} = k_0^2 v_n \overline{\overline{\mathbf{G}}}_{m,n} \cdot \left( \overline{\overline{\mathbf{I}}} - \overline{\overline{\boldsymbol{\varepsilon}}}_{r_n} \right) \cdot \overline{\overline{\mathbf{P}}}_n^{-1}.$$

Once  $\mathbf{E}^{tot}$  has been calculated,  $\mathbf{J}_m$  is determined using Eq. (1.24). Finally, the scattered field is computed as

$$\mathbf{E}^{scat}(\mathbf{r}) = i\omega\mu_0 \sum_{n=1}^N v_n \overline{\overline{\mathbf{G}}}(\mathbf{r}, \mathbf{r}_n) \cdot \mathbf{J}(\mathbf{r}_n). \tag{1.26}$$

### 1.3.8 A glimpse at Wirtinger calculus for optimization

In research of many engineering problems (not only the electromagnetic inverse scattering), one often has to use line search algorithms to address the optimization of scalar real function of complex variables. To determine the search direction, although using the real gradient is always correct, this way is rather awkward and inconvenient since the problem is defined in the framework of complex domain. Fortunately, the derivation can be greatly simplified if we apply the complex derivative (gradient) operator defined in the Wirtinger calculus, termed as Wirtinger derivatives. Interested readers are referred to [116–118] for an extended discussion.

Despite its usefulness, the Wirtinger derivative often causes confusion, because it is not consistent with the standard definition of complex derivative in standard complex variables courses. According to the standard definition of complex derivative, the derivative of a function  $f(z) = u(x, y) + iv(x, y)$  of complex number  $z$  exists if and only if it satisfies the *Cauchy-Riemann conditions*

$$\frac{\partial u}{\partial x} = \frac{\partial v}{\partial y}, \quad (1.27a)$$

$$\frac{\partial v}{\partial x} = -\frac{\partial u}{\partial y}, \quad (1.27b)$$

Such function is termed as holomorphic (analytic in  $z$ ).

By this definition, the scalar real function of complex variables is not holomorphic, so its standard derivative does not even exist. In Wirtinger calculus, however, as long as a function  $f(z)$  is differential with respect to  $x$  and  $y$ , its



*Wirtinger derivative* can be defined as

$$\frac{\partial f}{\partial z} \triangleq \frac{1}{2} \left( \frac{\partial f}{\partial x} - i \frac{\partial f}{\partial y} \right) \quad (1.28a)$$

$$\frac{\partial f}{\partial z^*} \triangleq \frac{1}{2} \left( \frac{\partial f}{\partial x} + i \frac{\partial f}{\partial y} \right) \quad (1.28b)$$

where the superscript  $*$  signifies complex conjugate. It follows that

$$\left( \frac{\partial f}{\partial x} + i \frac{\partial f}{\partial y} \right) = 2 \frac{\partial f}{\partial z^*}, \quad (1.29)$$

so instead of calculating the derivative with respect to  $x$  and  $y$  respectively, we only need to calculate the Wirtinger derivative with respect to  $z^*$ . The Wirtinger derivatives of most common functions with respect to a single variable are listed in Table 1.2. It is naturally generalized to the Wirtinger derivative of a scalar real

Table 1.2: Wirtinger derivatives

$f(z)$	$\frac{\partial f(z)}{\partial z}$	$\frac{\partial f(z)}{\partial z^*}$
$cz$	$c$	$0$
$cz^*$	$0$	$c$
$zz^*$	$z^*$	$z$

function  $f(\mathbf{z})$  with respect to multiple variables ( $\bar{\mathbf{z}} = [z_1, z_2, \dots, z_n]^T$ ), i.e., the *Wirtinger gradient*, which is conveniently defined accordingly:

$$\nabla_{\bar{\mathbf{z}}} f \triangleq \begin{bmatrix} \frac{\partial f}{\partial z_1} \\ \frac{\partial f}{\partial z_2} \\ \vdots \\ \frac{\partial f}{\partial z_n} \end{bmatrix}$$

$$\nabla_{\bar{\mathbf{z}}^*} f \triangleq \begin{bmatrix} \frac{\partial f}{\partial z_1^*} \\ \frac{\partial f}{\partial z_2^*} \\ \vdots \\ \frac{\partial f}{\partial z_n^*} \end{bmatrix}$$

The Wirtinger gradient of most common functions are listed in Table 1.3, where the superscript  $H$  signifies Hermitian.

Table 1.3: Wirtinger gradients

$f(\bar{z})$	$\nabla_{\bar{z}} f$	$\nabla_{\bar{z}^*} f$
$\bar{c}^T \bar{z} = \bar{z}^T \bar{c}$	$\bar{c}$	$\bar{0}$
$\bar{c}^T \bar{z}^* = \bar{z}^H \bar{c}$	$\bar{0}$	$\bar{c}$
$\bar{z}^H \bar{z} = \bar{z}^T \bar{z}^*$	$\bar{z}^*$	$\bar{z}$
$\bar{z}^H \bar{M} \bar{z} = \bar{z}^T \bar{M} \bar{z}^*$	$\bar{M}^T \bar{z}^*$	$\bar{M} \bar{z}$

## 1.4 Synopsis of this thesis

The author's original contribution is described in the remainder of this thesis, where the specific electromagnetic inverse problems of different sorts are addressed, covering both the full-data and the phaseless data measurement, and both point-like and extended scatterers. These sub-topics are discussed in individual chapters.

In Chapter 2, we describe the formulation of the electromagnetic inverse scattering problem of extended scatterers, with the measurement data being the scattered electromagnetic field. This problem is solved by the full-data subspace-based optimization method (FD-SOM). In addition, a comparison among the variants of FD-SOM is also presented, which indicates the optimum choice for specific problems.

Chapter 3 presents the phaseless-data subspace-based optimization method (PD-SOM), which deals with the inverse scattering problem of reconstructing extended scatterers with intensity-only measurement.

In Chapter 4, we formulate in the framework of compressive sensing (CS) the problem of imaging point-like scatterers with phaseless-data and describe the compressive phaseless imaging through minimizing a convex functional.

Chapter 5 concludes the thesis with suggestions for future work.



# Full Data Subspace-based Optimization Method

---

*“Curiouser and curiouser!”*

—*Lewis Carroll, Alice’s Adventures in Wonderland*

## 2.1 Original contributions

Recently, a full data subspace-based optimization method (FD-SOM or briefly SOM) was proposed in [29] to solve the electromagnetic inverse scattering problem, which has been found to be rapidly convergent, robust against noise, and able to reconstruct scatterers with complicated shapes. The essence of SOM is that the contrast source is partitioned into the deterministic portion and the ambiguous portion. The former is readily obtained by the spectrum analysis, while the latter can be determined by various optimization means. The original SOM was published in [29], where the coefficient vector  $\bar{\alpha}_p^n$  (refer to Section 3 of [29] or Section 2.4.2 of this chapter for the detail) is treated as a function of the scattering strength  $\bar{\xi}$  (refer to Section 2 of [29] or Table 2.1 of this chapter for the detail) in the least squares sense, and  $\bar{\xi}$  is determined by minimizing a nonlinear

objective function. Subsequently, a combination of CSI and SOM, which we shall conveniently refer to as CSI-like SOM was proposed in [120]. For the CSI-like SOM, the ambiguous portion is determined by an algorithm sharing some common features with CSI, i.e.,  $\bar{\alpha}_p^n$  and  $\bar{\xi}$  being alternatively updated [120]. As a consequence, the matrix inverse operation can be avoided so as to reduce considerably the computational cost.

Sections 2.2 and 2.3 generalize the SOM method for extension to the transverse electric (TE) case, where the electric field is transverse to the longitudinal direction of the two-dimensional system, in both the framework of the coupled dipole method (CDM) and the framework of the method of moments (MoM). It is worth highlighting that this generalization is not a simple mathematical replacement of TM parameters by their corresponding TE counterparts. The analysis involves a vector wave for the TE case since the electric field is in the transverse plane; for the TM case, on the other hand, the electric field is in the longitudinal direction and thus it is effectively a scalar electric field. As a consequence, the TE case is mathematically more complex than the TM case. In addition, the total electric field incident upon a subunit is not equal to the electric field inside the subunit, and the scattering strength of the subunit becomes a nonlinear function of relative permittivity. In comparison, for the TM case, the total electric field incident upon a subunit is equal to the electric field inside the subunit, resulting in a simple linear relationship of the scattering strength to the relative permittivity. Another significant difference between these two cases is that the electric field for the TE case is oriented differently for different incidence directions, hence allowing for enhanced capability in probing the two-dimensional structure of scatterers.

The original contributions in sections 2.2 and 2.3 may be summarized as follows:

- (a) It generalizes the SOM method to the TE case, which is physically different from and mathematically more complex than the TM case.
- (b) By analyzing the role of the dimension of the signal subspace, we show that it behaves somewhat as a regularization parameter, balancing the error of the measured data and the error of the physical model. It is encouraging to find that there is a wide range of dimensions of the signal subspace yielding satisfactory reconstruction results.
- (c) We show that for the TE case the electric field is oriented differently for different incidence directions, thus allowing for a better capability of probing the two dimensional structure of scatterers. Numerical results show that the reconstructed pattern in the TE case is smoother than that in the TM case.
- (d) There is a dominance of numerical results presented in the literature for the TM case. We present, instead, numerical results for several scatterers of complex geometries under TE incidence.

After that, a comparative study of the variants of SOM is provided in section 2.4, where the original contributions may be summarized as follows:

- (a) Firstly, for transverse electric (TE) case, it provides the user of SOM with the empirical formulas for the choice of the number of leading singular values and the definition of a practically effective criterion of terminating the optimization iteration.

- (b) Secondly, on the basis of a number of numerical simulations, we evaluate comparatively the performance of the three variants of SOM in TE case in terms of computational cost and the reconstruction capability. In order to support a relatively thorough analysis, the numerical experiments are designed to cover different working conditions, including different complexity levels of the patterns, different noise levels, both lossless and the lossy scatterers, and so on. For SOM, the calculation of the ambiguous portion plays a dominant role in determining the computational cost and the reconstruction capability of the algorithm. Therefore the exploration for the optimal method in this regard through a detailed comparative analysis is valuable in research and necessary in application. The main conclusion is that the CSI-like SOM surpasses the other two variants in terms of computational cost and the reconstruction capability.
- (c) Thirdly, it proposes a novel variant of SOM, where the cost function remains identical to that in CSI-like SOM, however, both  $\bar{\alpha}_p^n$  and  $\bar{\xi}$  are concurrently updated in each iteration. This novel variant makes our comparative study complete.

## 2.2 FD-SOM in the framework of CDM

### 2.2.1 Formulation of the forward scattering problem

In this section, we consider a two-dimensional setting under TE incidence for the inverse problem where the cylindrical dielectric scatterers (which are inhomogeneous in the  $x$ - $y$  plane but invariant in the  $z$  direction) are located in the domain  $\mathbf{D} \subset \mathbf{R}^2$  in the  $x$ - $y$  plane. The geometry of the inverse scattering problem



is shown in Fig. 2.1.  $N_t$  unit magnetic current line sources (TE polarization) are arranged at  $\mathbf{r}_p^t$  ( $p = 1, 2, \dots, N_t$ ) in a circle around the scatterers, which are illuminated successively by the sources with the incident waves expressed as  $\mathbf{H}_p^{inc}(\mathbf{r}) = \hat{\mathbf{z}}H_{z,p}^{inc}(\mathbf{r}) = \hat{\mathbf{z}}\frac{i}{4}H_0^{(1)}(k_0 \cdot |\mathbf{r}_p^t - \mathbf{r}|)$ , and  $\mathbf{E}_p^{inc}(\mathbf{r}) = \hat{\mathbf{x}}E_{x,p}^{inc}(\mathbf{r}) + \hat{\mathbf{y}}E_{y,p}^{inc}(\mathbf{r})$  can be obtained by Ampère's Law. The scattered waves are received by  $N_r$  receivers located at  $\mathbf{r}_q^r$  ( $q = 1, 2, \dots, N_r$ ), which are also placed in a circle surrounding the scatterers. The inverse problem consists of determining the relative permittivity profile of the scatterers, given a set of  $N_t N_r$  scattering data,  $\mathbf{E}_p^{scat}(\mathbf{r}_q^r)$ , where  $p = 1, 2, \dots, N_t$ ;  $q = 1, 2, \dots, N_r$ . In practice, the domain  $\mathbf{D}$  is discretized into a total number of  $N_d$  subunits, with the centers of the subunits located at  $\mathbf{r}_m$  ( $m = 1, 2, \dots, N_d$ ), and the problem then reduces to determining  $\varepsilon(\mathbf{r}_m)$ .

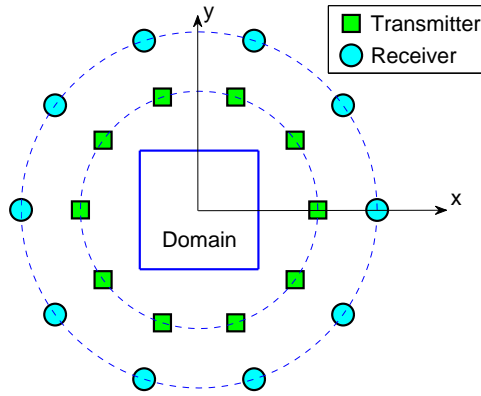


Figure 2.1: Geometry of the inverse scattering problem.

The total electric field incident upon the  $m$ th subunit is denoted as  $\mathbf{E}^{tot}(\mathbf{r}_m) = \hat{\mathbf{x}}E_x^{tot}(\mathbf{r}_m) + \hat{\mathbf{y}}E_y^{tot}(\mathbf{r}_m)$ . Collectively, they satisfy the following self-consistent

relationships [114, 121, 122],

$$E_{p,x}^{tot}(\mathbf{r}_m) = E_{p,x}^{inc}(\mathbf{r}_m) + \sum_{\substack{n=1 \\ n \neq m}}^{N_d} ik_0\eta_0\xi(\mathbf{r}_n)[g_{11}(\mathbf{r}_m, \mathbf{r}_n)E_{p,x}^{tot}(\mathbf{r}_n) + g_{12}(\mathbf{r}_m, \mathbf{r}_n)E_{p,y}^{tot}(\mathbf{r}_n)], \quad (2.1a)$$

$$E_{p,y}^{tot}(\mathbf{r}_m) = E_{p,y}^{inc}(\mathbf{r}_m) + \sum_{\substack{n=1 \\ n \neq m}}^{N_d} ik_0\eta_0\xi(\mathbf{r}_n)[g_{21}(\mathbf{r}_m, \mathbf{r}_n)E_{p,x}^{tot}(\mathbf{r}_n) + g_{22}(\mathbf{r}_m, \mathbf{r}_n)E_{p,y}^{tot}(\mathbf{r}_n)], \quad (2.1b)$$

$$(m = 1, 2, \dots, N_d),$$

where the subscript  $p$  means that the incident field is due to the  $p$ th source antenna; the subscripts  $x$  and  $y$  denote the x- and y- components, respectively; the superscript *inc* refers to the incident field radiated by the line sources; the superscript *tot* represents the summation of all the fields incident upon the subunit, including the fields due to the transmitting sources and the induced sources;  $k_0$  and  $\eta_0$  are the free-space wave number and impedance respectively;  $\xi(\mathbf{r}_n)$  denotes the scattering strength of  $n$ th subunit; and  $g_{ab}(\mathbf{r}_m, \mathbf{r}_n)$  is the element of the following two-dimensional dyadic Green's function [112], with respect to two locations  $\mathbf{r}_m$  and  $\mathbf{r}_n$ ,

$$\bar{\bar{g}}(\mathbf{r}_m, \mathbf{r}_n) = \begin{pmatrix} g_{11}(\mathbf{r}_m, \mathbf{r}_n) & g_{12}(\mathbf{r}_m, \mathbf{r}_n) \\ g_{21}(\mathbf{r}_m, \mathbf{r}_n) & g_{22}(\mathbf{r}_m, \mathbf{r}_n) \end{pmatrix}.$$

After the  $E^{tot}$  is obtained, the scattered field is given by

$$E_{p,x}^{scat}(\mathbf{r}_q^r) = \sum_{n=1}^{N_d} ik_0\eta_0\xi(\mathbf{r}_n)[g_{11}(\mathbf{r}_q^r, \mathbf{r}_n)E_{p,x}^{tot}(\mathbf{r}_n) + g_{12}(\mathbf{r}_q^r, \mathbf{r}_n)E_{p,y}^{tot}(\mathbf{r}_n)], \quad (2.2a)$$

$$E_{p,y}^{scat}(\mathbf{r}_q^r) = \sum_{n=1}^{N_d} ik_0\eta_0\xi(\mathbf{r}_n)[g_{21}(\mathbf{r}_q^r, \mathbf{r}_n)E_{p,x}^{tot}(\mathbf{r}_n) + g_{22}(\mathbf{r}_q^r, \mathbf{r}_n)E_{p,y}^{tot}(\mathbf{r}_n)], \quad (2.2b)$$

$$(q = 1, 2, \dots, N_r).$$

The small square subunits, which are chosen in the numerical simulations, can

be well approximated by circles of equal area [113], therefore in Eq. (2.1) and Eq. (2.2), the scattering strength reads  $\xi(\mathbf{r}_n) = -2i \frac{k_0}{\eta_0} A_n \frac{\varepsilon_r(\mathbf{r}_n) - 1}{\varepsilon_r(\mathbf{r}_n) + 1}$ , where  $A_n$  and  $\varepsilon_r(\mathbf{r}_n)$  denote the area and the relative permittivity of the  $n$ th subunit. This parameter relates the induced contrast displacement current in the  $n$ th subunit to the total incident electric field by

$$I_x^d(\mathbf{r}_n) = \xi(\mathbf{r}_n) E_x^{tot}(\mathbf{r}_n), \quad (2.3a)$$

$$I_y^d(\mathbf{r}_n) = \xi(\mathbf{r}_n) E_y^{tot}(\mathbf{r}_n). \quad (2.3b)$$

The combination of Eq. (2.3) and Eq. (2.1) yields

$$\bar{I}_p^d = \bar{\xi}(\bar{E}_p^{inc} + \bar{G}_D \cdot \bar{I}_p^d), \quad (2.4)$$

where

$$\bar{I}_p^d = [I_{p,x}^d(\mathbf{r}_1), I_{p,x}^d(\mathbf{r}_2), \dots, I_{p,x}^d(\mathbf{r}_{N_d}), I_{p,y}^d(\mathbf{r}_1), I_{p,y}^d(\mathbf{r}_2), \dots, I_{p,y}^d(\mathbf{r}_{N_d})]^T$$

(the superscript  $T$  represents the transpose operator) and

$$\bar{E}_p^{inc} = [E_{p,x}^{inc}(\mathbf{r}_1), E_{p,x}^{inc}(\mathbf{r}_2), \dots, E_{p,x}^{inc}(\mathbf{r}_{N_d}), E_{p,y}^{inc}(\mathbf{r}_1), E_{p,y}^{inc}(\mathbf{r}_2), \dots, E_{p,y}^{inc}(\mathbf{r}_{N_d})]^T$$

are both column vectors of size  $2N_d$ ;

$$\bar{\xi} = \text{diag}[\xi(\mathbf{r}_1), \xi(\mathbf{r}_2), \dots, \xi(\mathbf{r}_{N_d}), \xi(\mathbf{r}_1), \xi(\mathbf{r}_2), \dots, \xi(\mathbf{r}_{N_d})]$$

is a diagonal matrix of size  $2N_d \times 2N_d$ ;

$$\bar{G}_D = \begin{pmatrix} \bar{G}_{D11} & \bar{G}_{D12} \\ \bar{G}_{D21} & \bar{G}_{D22} \end{pmatrix}$$

is a matrix of size  $2N_d \times 2N_d$  with

$$\overline{\overline{G}}_{Dab}(m, n) = \begin{cases} ik_0\eta_0 \cdot g_{ab}(\mathbf{r}_m, \mathbf{r}_n), & m \neq n \\ 0, & m = n \end{cases}, \quad (a, b = 1, 2; m, n = 1, 2, \dots, N_d).$$

Similarly, substituting Eq. (2.3) into Eq. (2.2) gives

$$\overline{E}_p^{scat} = \overline{\overline{G}}_S \cdot \overline{I}_p^d, \quad (2.5)$$

where

$$\overline{E}_p^{scat} = [E_{p,x}^{scat}(\mathbf{r}_1^r), E_{p,x}^{scat}(\mathbf{r}_2^r), \dots, E_{p,x}^{scat}(\mathbf{r}_{N_r}^r), E_{p,y}^{scat}(\mathbf{r}_1^r), E_{p,y}^{scat}(\mathbf{r}_2^r), \dots, E_{p,y}^{scat}(\mathbf{r}_{N_r}^r)]^T$$

is a column vector of size  $2N_r$ ;

$$\overline{\overline{G}}_S = \begin{pmatrix} \overline{\overline{G}}_{S11} & \overline{\overline{G}}_{S12} \\ \overline{\overline{G}}_{S21} & \overline{\overline{G}}_{S22} \end{pmatrix}$$

is a matrix of size  $2N_r \times 2N_d$  with

$$\overline{\overline{G}}_{Sab}(q, n) = ik_0\eta_0 \cdot g_{ab}(\mathbf{r}_q^r, \mathbf{r}_n), \quad (a, b = 1, 2; q = 1, 2, \dots, N_r; n = 1, 2, \dots, N_d).$$

Eq. (2.4) and Eq. (2.5) are referred to as *state equation* and *field equation* respectively, and they constitute the basic equations for use in the inverse scattering problem.

## 2.2.2 Inversion algorithm

Following the SOM algorithm proposed in [29], the induced currents due to the  $p$ th incidence ( $\overline{I}_p^d$ ) on scatterers are decomposed into two orthogonally complementary parts, i.e., the deterministic part  $\overline{I}_p^s$  and the ambiguous part  $\overline{I}_p^n$ . It can be expressed as  $\overline{I}_p^d = \overline{I}_p^s + \overline{I}_p^n = \overline{I}_p^s + \overline{\overline{V}}^n \cdot \overline{\alpha}_p^n$ , where  $\overline{\overline{V}}^n$  is the noise subspace composed of the last  $2N_d - L$  right singular vectors,  $\overline{\alpha}_p^n$  is a vector of coefficients

to be determined by optimization, and  $L$  is the total number of singular values that are above a predefined noise-dependent threshold [29]. After  $\bar{I}_p^s$  is determined by the singular value decomposition (SVD), the  $\varepsilon_r$  of the scatterers can be obtained by minimizing the objective function which can be expressed explicitly as

$$f(\bar{\varepsilon}_r) = \frac{1}{2} \sum_{p=1}^{N_t} \left[ \frac{\|\bar{G}_S \cdot \bar{V}^n \cdot \bar{\alpha}_p^n + \bar{G}_S \cdot \bar{I}_p^s - \bar{E}_p^{scat}\|^2}{\|\bar{E}_p^{scat}\|^2} + \frac{\|\bar{A} \cdot \bar{\alpha}_p^n - \bar{B}_p\|^2}{\|\bar{I}_p^s\|^2} \right]^2 \quad (2.6)$$

where  $\bar{A} = \bar{V}^n - \bar{\xi} \cdot (\bar{G}_D \cdot \bar{V}^n)$  and  $\bar{B}_p = \bar{\xi} \cdot (\bar{E}^{inc} + \bar{G}_D \cdot \bar{I}_p^s) - \bar{I}_p^s$  are both functions of the  $N_d \times 1$  relative permittivity vector  $\bar{\varepsilon}_r$ . Note that  $\bar{\alpha}_p^n$  can be obtained by the least squares solution [29]. In numerical simulations, we use the Levenberg-Marquardt algorithm to minimize the objective function. It is worth mentioning that the parameter to be optimized in Eq. (2.6) is relative permittivity, which is different from [29] where the scattering strength is optimized.

The main feature of the proposed SOM lies in the following two aspects: First, deterministic current  $\bar{I}^s$  can be obtained straightforwardly by the SVD, without recourse to optimization; Second, the dimension of the space of ambiguous current, which is to be reconstructed by optimization methods, is smaller than that used in the traditional optimization methods. These two features reduce the degree of non-linearity of the inverse scattering problem; as a result, the SOM significantly speeds up the convergence and performs robustly in presence of noise.

### 2.2.3 Numerical results

All the numerical simulations reported in this section are based on the same set of values assigned to the following parameters. The line sources (transmitting antennas) are evenly distributed on a circle of radius  $5\lambda$ , with locations  $(5\lambda \cdot$

$\cos \frac{2\pi p}{N_t}, 5\lambda \cdot \sin \frac{2\pi p}{N_t}$   $p = 1, 2, \dots, N_t$ . A total number of  $N_r = 30$  receivers are also evenly distributed on a circle of radius  $5\lambda$ , with locations  $(5\lambda \cdot \cos \frac{2\pi q}{N_r}, 5\lambda \cdot \sin \frac{2\pi q}{N_r})$   $q = 1, 2, \dots, N_r$ . In order to avoid the inverse crime [6], we first check the validity of the forward solver Eq. (2.4) and Eq. (2.5) by comparing it with another numerical method, the method of moments (MoM) [113]. The difference between the scattered fields produced by these two methods is negligibly small, which proves the validity of the forward solver. The scattered field is recorded in the format of the multi-static response (MSR) matrix  $\overline{\overline{K}}$  whose size is  $2N_r \times N_t$  [30]. Gaussian white noise  $\overline{\overline{\kappa}}$  is thereafter added to the MSR matrix, and the resultant noise-corrupted matrix  $\overline{\overline{K}} + \overline{\overline{\kappa}}$  is treated as the measured MSR matrix which is used to reconstruct the scatterers. The noise level is quantified in signal-to-noise ratio ( $SNR$ ) as  $20 \cdot \log \frac{\|\overline{\overline{K}}\|_F}{\|\overline{\overline{\kappa}}\|_F}$ , where  $\|\cdot\|_F$  denotes the Frobenius norm of a matrix [105]. We choose free space as the initial guess in the optimization problem, i.e.,  $\varepsilon_r(\mathbf{r}_m) = 1$ ,  $m = 1, 2, \dots, N_d$ .

The previous TM case reported in paper [29] reconstructs the pattern of an annulus in the presence of 10dB and 20dB noise level. Although the reconstructed pattern in [29] clearly exhibits the central hole, its quality suffers from the flaw that the value of  $\varepsilon_r$  fluctuates noticeably along the annulus. This drawback may be attributed to the reason that for the TM mode all the incident electric fields are oriented in the longitudinal direction, and therefore contain limited amount of information about  $\varepsilon_r$ , which is non-uniform in the transverse plane. In contrast, for TE mode, the orientation of the electric field varies in the transverse plane for every incidence direction, and hence the scattered wave might be able to provide additional information about  $\varepsilon_r$  and upgrade the quality of the reconstructed

pattern. To demonstrate this, a numerical experiment is performed to reconstruct the identical scatterer by using the SOM algorithm under the same conditions adopted in [29] except for the switch to TE incidence. The result, as illustrated in Fig. 2.2, shows a smoother pattern with much less fluctuation of  $\varepsilon_r$  along the annulus, compared with Fig. 3 and Fig. 4 in [29]. In presence of noise, for the SOM algorithm, choosing an appropriate value for the number of leading singular values ( $L$ ) from the spectrum of the matrix  $\overline{\overline{G_S}}$  (shown in Fig. 2.3) not only improves the convergence speed and the quality of the reconstructed patterns, but also strengthens the immunity to noise. It has been observed during the course of this investigation that a quantitative study of the exact choice of  $L$  proves difficult, mainly because it is a problem that depends on individual situations. Nevertheless, from the qualitative point of view, there may roughly exist a range of values for  $L$  over which optimal reconstruction could be achieved. If  $L$  is too large (i.e. on the right side of the optimal range), although the field equation is well satisfied and the convergence can be swiftly reached, the increase in the residue occurs due to the error of the physical model. On the other hand, if  $L$  is too small (i.e. on the left side of the optimal range), less deterministic current is determined and the dimension of the noise subspace is large. Consequently, the convergence becomes more time-consuming. Another numerical experiment has been performed to study the relation between  $L$  and absolute residue that is defined as the arithmetic mean of the absolute value of the difference between the exact relative permittivity and the reconstructed relative permittivity. From the result, shown in Fig. 2.4, it can be seen that, for the pattern of annulus, the absolute residue saturates after about 15 iterations, and the optimal range, corresponding to the minimum absolute residue,

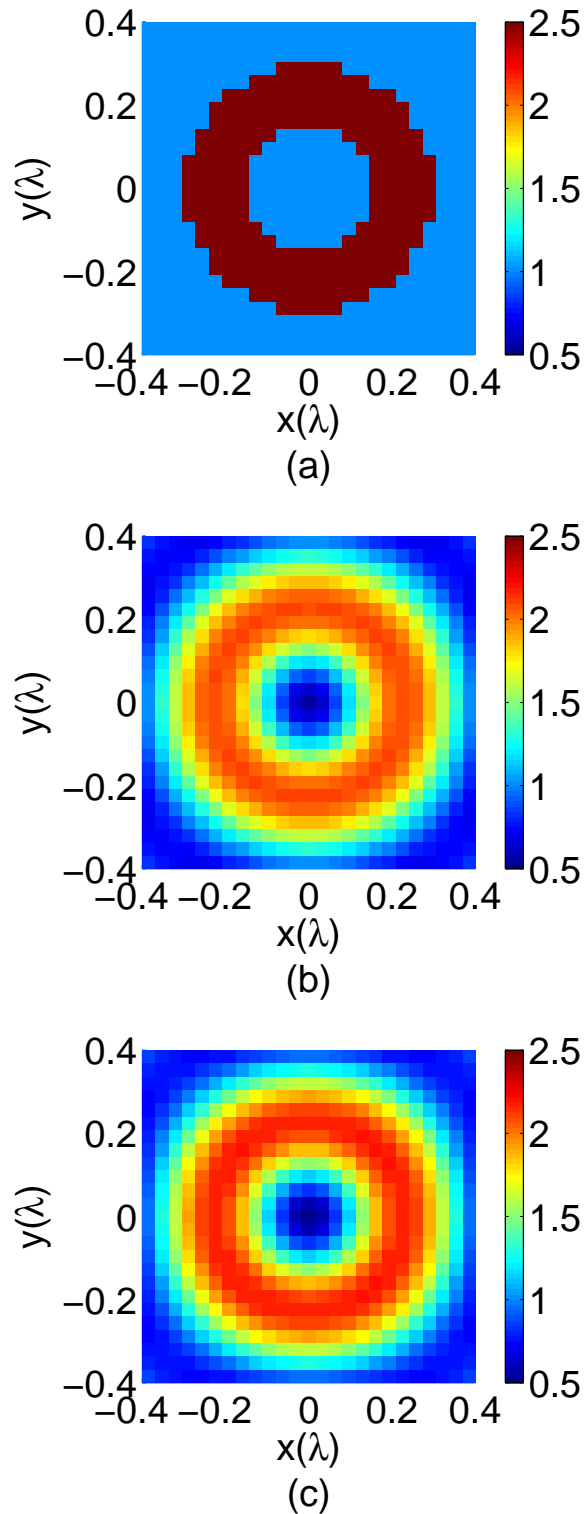


Figure 2.2: An annulus with inner radius  $0.15\lambda$  and outer radius  $0.3\lambda$ . (a). Exact permittivity. (b) Reconstructed permittivity for SNR=20dB. (c) Reconstructed permittivity for SNR=10dB.



is found to be from 10 to 35, where the optimal balance is reached between the error of the field equation and the error of the state equation. This is an encouraging result, since the value of  $L$  does not critically depend on any parameter and there is a wide continuous range of integer values of  $L$  yielding satisfactory reconstruction results.

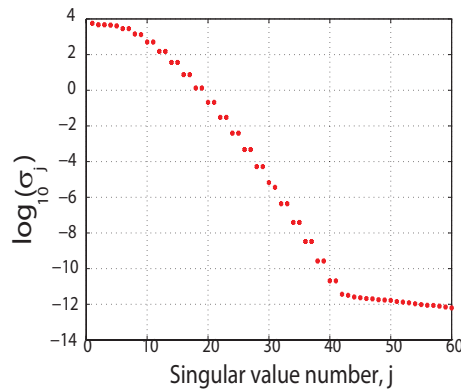


Figure 2.3: Singular values of the matrix  $\overline{\overline{G}}_S$  in the first numerical simulation.

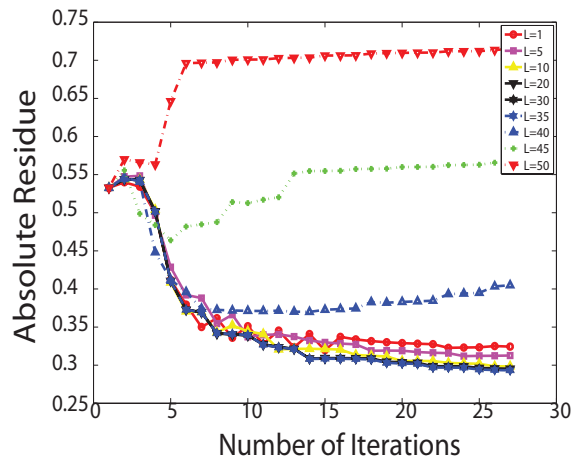


Figure 2.4: Absolute residue versus number of iterations for different values of  $L$

To challenge the SOM algorithm for the TE case, the next numerical experiment deals with a more complex pattern, where a circle (with relative permittivity of 2.5 and radius of  $0.15\lambda$ ) is placed in the central hole of a concentric annulus (with

relative permittivity of 2 and inner and outer radii of  $0.4\lambda$  and  $0.6\lambda$  respectively) in a square domain (with width of  $1.6\lambda$ ) discretized into a grid of  $40 \times 40$  subunits. Since this pattern is more complicated than the one adopted for the first experiment (Fig. 2.2), the number of transmitting antennas is increased to  $N_t = 14$ . In addition,  $L$  is chosen to be 10, and SNR is increased to 10dB. The exact pattern and the inverse result obtained after 20 iterations are presented in Fig. 2.5(a)(b) respectively, where the reconstructed pattern seems rather close to the original one, and the gap (with width of  $0.25\lambda$ ) can be clearly seen between the central circle and the annulus. For the final example, a set of digit patterns (with relative permittivity of 2) is reconstructed by the SOM algorithm under TE incidence. The set of patterns in Fig. 2.6 has not been reported elsewhere in the literature for use in the inverse scattering (to the best of the author's knowledge). The domain is a rectangle of size  $1.4\lambda \times 0.7\lambda$  which has been discretized into a grid of  $40 \times 20$  subunits. The number of incidence is increased to  $N_t = 20$  because of the complexity of the patterns. For the numerical experiment, the SNR is 20dB and the value of  $L$  is chosen to be 7. Fig. 2.7 shows that the original digits can be easily identified from the reconstructed patterns obtained after 20 iterations.

## 2.3 FD-SOM in the framework of MoM

### 2.3.1 Formulation of the forward scattering problem

We consider a two-dimensional setting under TE incidence for the inverse problem. The configuration of the experiment is the same as described in section 2.2.

The electric field integral equation (EFIE) [113] can be expressed as the

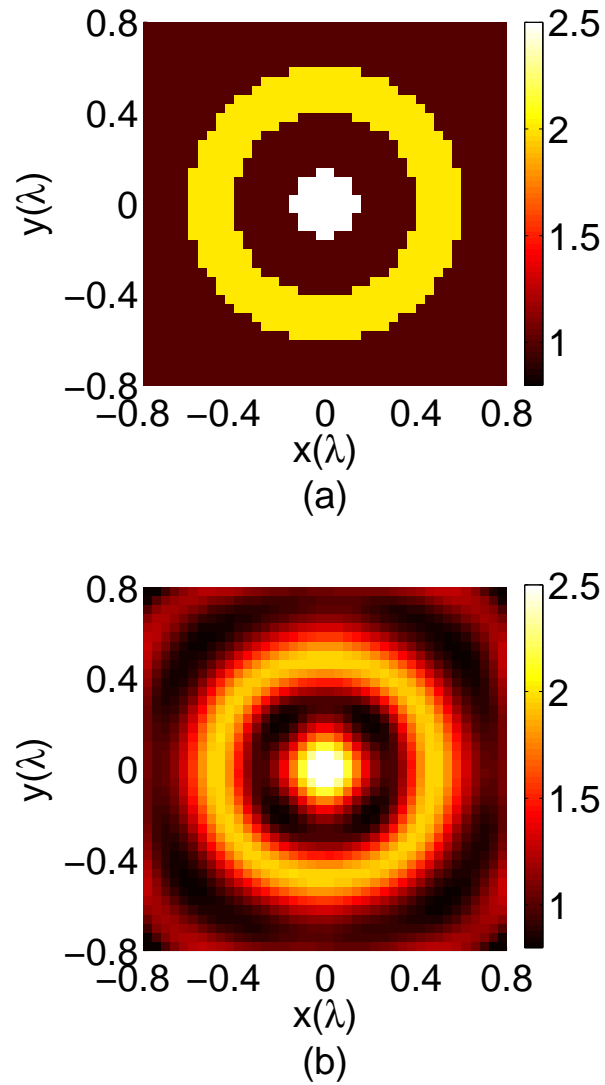


Figure 2.5: The pattern consisting of a circle and an annulus. (a) Exact relative permittivity. (b) Reconstructed relative permittivity for SNR=10dB.

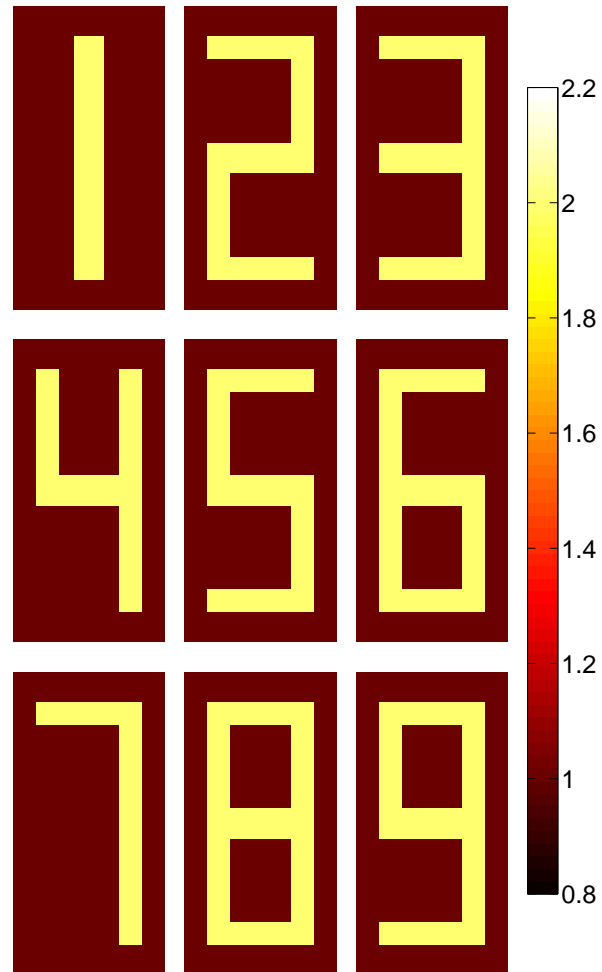


Figure 2.6: The exact digit patterns of relative permittivity

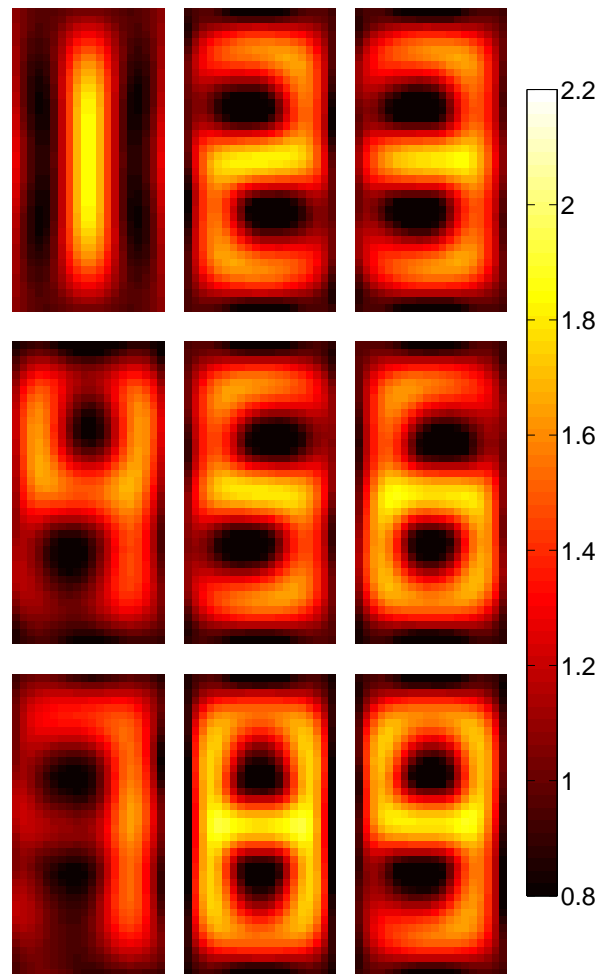


Figure 2.7: The reconstructed digit patterns of relative permittivity

relationship between the incident electric field  $\mathbf{E}^{inc}(\mathbf{r}_m) = \hat{\mathbf{x}}E_x^{inc}(\mathbf{r}_m) + \hat{\mathbf{y}}E_y^{inc}(\mathbf{r}_m)$  and the equivalent electric polarization current densities  $\mathbf{J}(\mathbf{r}_m) = \hat{\mathbf{x}}J_x(\mathbf{r}_m) + \hat{\mathbf{y}}J_y(\mathbf{r}_m)$ , which is known as the MoM method [113],

$$E_{p,x}^{inc}(\mathbf{r}_m) = \sum_{n=1}^{N_d} \frac{A_n \eta_0}{4k_0} \left[ \frac{\partial^2 H_0^{(1)}(k\rho_{mn})}{\partial x_n \partial y_n} J_{p,y}(\mathbf{r}_n) - \frac{\partial^2 H_0^{(1)}(k\rho_{mn})}{\partial y_n^2} J_{p,x}(\mathbf{r}_n) \right] + \frac{J_{p,x}(\mathbf{r}_m)}{\theta(\mathbf{r}_m)}, \quad (2.7a)$$

$$E_{p,y}^{inc}(\mathbf{r}_m) = \sum_{n=1}^{N_d} \frac{A_n \eta_0}{4k_0} \left[ \frac{\partial^2 H_0^{(1)}(k\rho_{mn})}{\partial x_n \partial y_n} J_{p,x}(\mathbf{r}_n) - \frac{\partial^2 H_0^{(1)}(k\rho_{mn})}{\partial x_n^2} J_{p,y}(\mathbf{r}_n) \right] + \frac{J_{p,y}(\mathbf{r}_m)}{\theta(\mathbf{r}_m)}, \quad (2.7b)$$

$(m = 1, 2, \dots, N_d),$

where the subscript  $p$  means that the incident field is due to the  $p$ th source antenna; the subscripts  $x$  and  $y$  denote the x- and y- components, respectively; the superscript *inc* refers to the incident field radiated by the line sources;  $k_0$  and  $\eta_0$  are the free-space wave number and impedance respectively;  $A_n$  denotes the area of the  $n$ th subunit. and  $\rho_{mn}$  is the distance between two locations  $\mathbf{r}_m$  and  $\mathbf{r}_n$ ,

$$\rho_{mn} = \sqrt{(x_m - x_n)^2 + (y_m - y_n)^2},$$

and

$$\theta(\mathbf{r}_m) = \frac{jk_0}{\eta_0} \cdot \frac{\varepsilon(\mathbf{r}_m) - 1}{\varepsilon(\mathbf{r}_m)}.$$

Eq. (2.7) can be expressed in a compact form as

$$\bar{\mathbf{J}}_p^d = \bar{\theta}(\bar{\mathbf{E}}_p^{inc} + \bar{\mathbf{G}}_D \cdot \bar{\mathbf{J}}_p^d), \quad (2.8)$$

where

$$\overline{\overline{G}}_D = \begin{pmatrix} \overline{\overline{G}}_{D11} & \overline{\overline{G}}_{D12} \\ \overline{\overline{G}}_{D21} & \overline{\overline{G}}_{D22} \end{pmatrix}$$

with

$$\overline{\overline{G}}_{D11}(m, n) = \begin{cases} \frac{\eta_0 A_n}{4k_0} \cdot \frac{\partial^2 H_0^{(1)}(k\rho_{mn})}{\partial y_n^2}, & m \neq n \\ \lim_{\rho_{mn} \rightarrow 0} \frac{\eta_0 A_n}{4k_0} \cdot \frac{\partial^2 H_0^{(1)}(k\rho_{mn})}{\partial y_n^2}, & m = n \end{cases}$$

$$\begin{aligned} \overline{\overline{G}}_{D12}(m, n) &= \overline{\overline{G}}_{D21}(m, n) \\ &= \begin{cases} -\frac{\eta_0 A_n}{4k_0} \cdot \frac{\partial^2 H_0^{(1)}(k\rho_{mn})}{\partial x_n \partial y_n}, & m \neq n \\ 0, & m = n \end{cases} \end{aligned}$$

$$\overline{\overline{G}}_{D22}(m, n) = \begin{cases} \frac{\eta_0 A_n}{4k_0} \cdot \frac{\partial^2 H_0^{(1)}(k\rho_{mn})}{\partial x_n^2}, & m \neq n \\ \lim_{\rho_{mn} \rightarrow 0} \frac{\eta_0 A_n}{4k_0} \cdot \frac{\partial^2 H_0^{(1)}(k\rho_{mn})}{\partial x_n^2}, & m = n \end{cases}$$

$$(m, n = 1, 2, \dots, N_d).$$

After obtaining the current densities  $\mathbf{J}(\mathbf{r}_m)$ , the scattered field can be determined

as

$$E_{p,x}^{scat}(\mathbf{r}_q) = \sum_{n=1}^{N_d} \frac{\eta_0 A_n}{4k_0} \left[ \frac{\partial^2 H_0^{(1)}(k\rho_{qn})}{\partial y_n^2} J_{p,x}(\mathbf{r}_n) - \frac{\partial^2 H_0^{(1)}(k\rho_{qn})}{\partial x_n \partial y_n} J_{p,y}(\mathbf{r}_n) \right], \quad (2.9a)$$

$$E_{p,y}^{scat}(\mathbf{r}_q) = \sum_{n=1}^{N_d} \frac{\eta_0 A_n}{4k_0} \left[ \frac{\partial^2 H_0^{(1)}(k\rho_{qn})}{\partial x_n^2} J_{p,y}(\mathbf{r}_n) - \frac{\partial^2 H_0^{(1)}(k\rho_{qn})}{\partial x_n \partial y_n} J_{p,x}(\mathbf{r}_n) \right], \quad (2.9b)$$

$$(q = 1, 2, \dots, N_r),$$

Similarly, it can be expressed in compact form as

$$\overline{E}_p^{scat} = \overline{\overline{G}}_S \cdot \overline{J}_p^d, \quad (2.10)$$

where

$$\overline{\overline{G}}_S = \begin{pmatrix} \overline{\overline{G}}_{S11} & \overline{\overline{G}}_{S12} \\ \overline{\overline{G}}_{S21} & \overline{\overline{G}}_{S22} \end{pmatrix}$$

with

$$\begin{aligned} \overline{\overline{G}}_{S11}(q, n) &= \frac{\eta_0 A_n}{4k_0} \frac{\partial^2 H_0^{(1)}(k\rho_{qn})}{\partial y_n^2}, \\ \overline{\overline{G}}_{S12}(q, n) = \overline{\overline{G}}_{S21}(q, n) &= -\frac{\eta_0 A_n}{4k_0} \frac{\partial^2 H_0^{(1)}(k\rho_{qn})}{\partial x_n \partial y_n}, \\ \overline{\overline{G}}_{S22}(q, n) &= \frac{\eta_0 A_n}{4k_0} \frac{\partial^2 H_0^{(1)}(k\rho_{qn})}{\partial x_n^2}, \end{aligned}$$

### 2.3.2 Inversion algorithm

Following the SOM algorithm proposed in [29], the equivalent electric polarization current density due to the  $p$ th incidence ( $\overline{J}_p^d$ ) on scatterers is decomposed into two orthogonally complementary parts, i.e., the deterministic part  $\overline{J}_p^s$  and the ambiguous part  $\overline{J}_p^n$ . It can be expressed as  $\overline{J}_p^d = \overline{J}_p^s + \overline{J}_p^n = \overline{J}_p^s + \overline{\overline{V}}^n \cdot \overline{\alpha}_p^n$ , where  $\overline{\overline{V}}^n$  is the noise subspace composed of the last  $2N_d - L$  right singular vectors,  $\overline{\alpha}_p^n$  is a vector of coefficients to be determined by optimization, and  $L$  is the total number of singular values that are above a predefined noise-dependent threshold [29]. After  $\overline{J}_p^s$  is determined by the singular value decomposition (SVD), the  $\varepsilon_r$  of the scatterers can be obtained by minimizing the objective function which can be expressed explicitly as



$$f(\bar{\varepsilon}_r) = \frac{1}{2} \sum_{p=1}^{N_t} \left[ \frac{\|\bar{G}_S \cdot \bar{V}^n \cdot \bar{\alpha}_p^n + \bar{G}_S \cdot \bar{J}_p^s - \bar{E}_p^{scat}\|^2}{\|\bar{E}_p^{scat}\|^2} + \frac{\|\bar{A} \cdot \bar{\alpha}_p^n - \bar{B}_p\|^2}{\|\bar{J}_p^s\|^2} \right]^2 \quad (2.11)$$

where  $\bar{A} = \bar{V}^n - \bar{\theta} \cdot (\bar{G}_D \cdot \bar{V}^n)$  and  $\bar{B}_p = \bar{\theta} \cdot (\bar{E}^{inc} + \bar{G}_D \cdot \bar{J}_p^s) - \bar{J}_p^s$  are both functions of the  $N_d \times 1$  relative permittivity vector  $\bar{\varepsilon}_r$ . Note that  $\bar{\alpha}_p^n$  can be obtained by the least squares solution [29]. In numerical simulations, we use the Levenberg-Marquardt algorithm to minimize the objective function. It is worth mentioning that the parameter to be optimized in Eq. (2.11) is relative permittivity, which is different from [29] where the scattering strength is optimized.

### 2.3.3 Numerical results

All the numerical simulations reported in this section are based on the same set of values assigned to the following parameters. The line sources (transmitting antennas) are evenly distributed on a circle of radius  $5\lambda$ , with locations  $(5\lambda \cdot \cos \frac{2\pi p}{N_t}, 5\lambda \cdot \sin \frac{2\pi p}{N_t})$   $p = 1, 2, \dots, N_t$ , to prevent the super-resolution phenomenon. A total number of  $N_r = 30$  receivers are also evenly distributed on a circle of radius  $5\lambda$ , with locations  $(5\lambda \cdot \cos \frac{2\pi q}{N_r}, 5\lambda \cdot \sin \frac{2\pi q}{N_r})$   $q = 1, 2, \dots, N_r$ . In order to avoid the inverse crime [6], we first check the validity of the forward solver Eq. (2.8) and Eq. (2.10) by comparing it with another numerical method, the coupled dipole method (CDM). The difference between the scattered fields produced by these two methods is negligibly small, which proves the validity of the forward solver. The scattered field is recorded in the format of the multi-static response (MSR) matrix  $\bar{K}$  whose size is  $2N_r \times N_t$  [30]. Gaussian white noise  $\bar{\kappa}$  is

thereafter added to the MSR matrix, and the resultant noise-corrupted matrix  $\overline{\overline{K}} + \overline{\overline{\kappa}}$  is treated as the measured MSR matrix which is used to reconstruct the scatterers. The noise level is defined in dB as done in [29]. We choose free space as the initial guess in the optimization problem, i.e.,  $\varepsilon_r(\mathbf{r}_m) = 1$ ,  $m = 1, 2, \dots, N_d$ .

The first numerical experiment investigates an annulus pattern (with relative permittivity of 2.5 and inner and outer radii of  $0.15\lambda$  and  $0.3\lambda$  respectively) which is the same pattern as in Fig. 3 in [29]. The value of  $L$  is chosen to be 9, where the singular values noticeably change the slope in the spectrum of the matrix  $\overline{\overline{G}}_S$  as shown in Fig. 2.8; this criterion is supported by the systematic work in [96, 123]. Using the SOM algorithm under the same conditions adopted in [29] except for the switch to TE incidence and the MoM framework, we obtain the reconstructed results after 20 iterations, as illustrated in Fig. 2.9 (b),(c) for 20dB and 10dB noise respectively, which are rather close to the exact pattern in Fig. 2.9 (a).

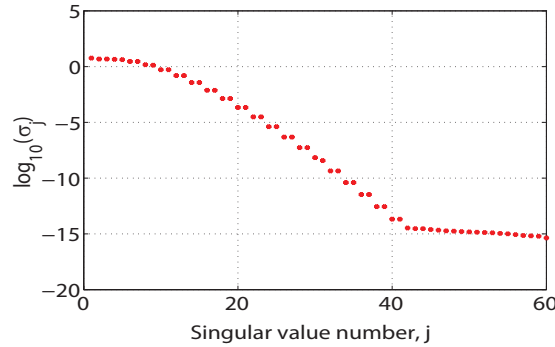


Figure 2.8: Singular values of the matrix  $\overline{\overline{G}}_S$  in the first numerical simulation.

The second numerical experiment deals with a more complex and challenging pattern, where a circle (with relative permittivity of 2.5 and radius of  $0.15\lambda$ ) is placed in the central hole of a concentric annulus (with relative permittivity of 2 and inner and outer radii of  $0.4\lambda$  and  $0.6\lambda$  respectively) in a square domain (with

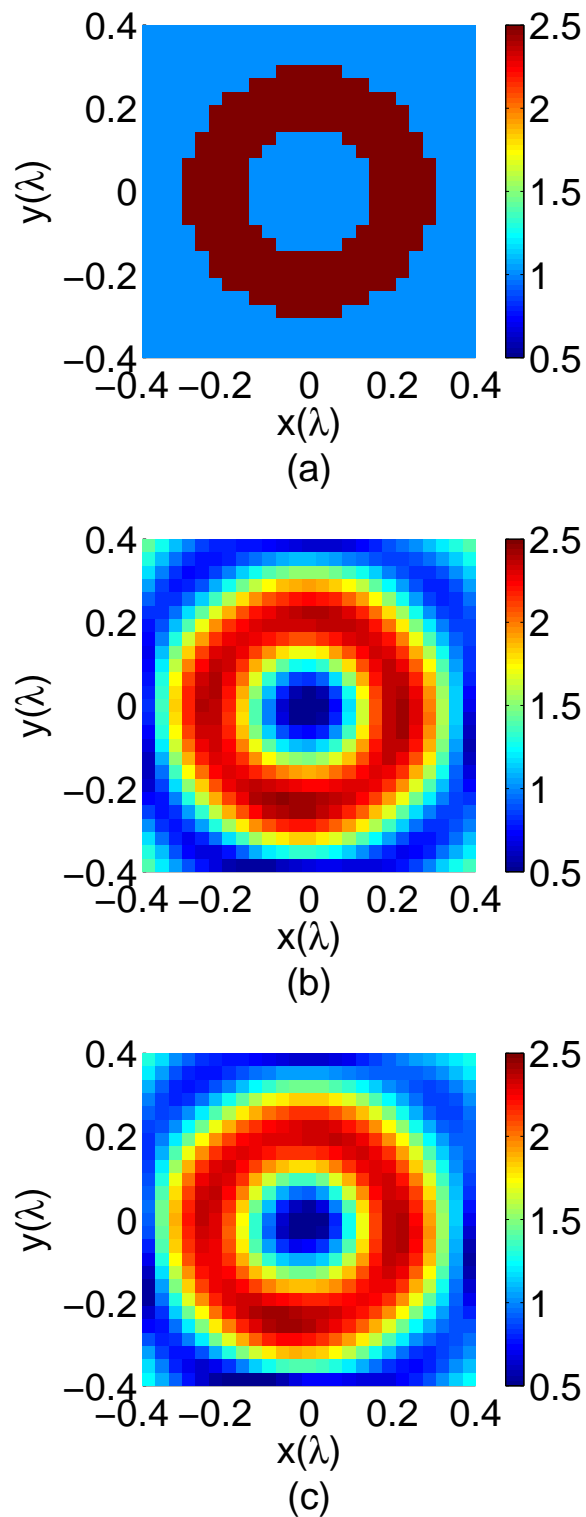


Figure 2.9: An annulus with inner radius  $0.15\lambda$  and outer radius  $0.3\lambda$ . (a). Exact permittivity. (b) Reconstructed permittivity under 20dB Gaussian white noise. (c) Reconstructed permittivity under 10dB Gaussian white noise.

width of  $1.6\lambda$ ) discretized into a grid of  $40 \times 40$  subunits. Since this pattern is more complicated than the one adopted for the first experiment (Fig. 2.9), the number of transmitting antennas is increased to  $N_t = 14$ . In addition,  $L$  is chosen to be 10, and 10dB noise is added into the scattering data. The exact pattern and the inverse result obtained after 20 iterations are presented in Fig. 2.10(a)(b) respectively, where the reconstructed pattern seems rather close to the original one, and the gap (with width of  $0.25\lambda$ ) can be clearly seen between the central circle and the annulus.

## 2.4 Comparison among the variants of SOM

### 2.4.1 The forward scattering problem

The configuration studied in this section is similar to that in Section 2 of [105], and is the same as described in section 2.2.

For reader's convenience, Table 2.1 lists the information about the variables involved in the formulation of the forward scattering problem. The *state equation* (Eq. (2.12)) and the *field equation* (Eq. (2.13)) constitute the basic equations for use in the inverse scattering problem. Their detailed derivation has already been furnished in [105]. The *state equation*, which describes how the induced contrast displacement current is generated by an incident field, can be expressed as

$$\bar{I}_p^d = \bar{\xi} \cdot (\bar{E}_p^{\text{inc}} + \bar{G}_D \cdot \bar{I}_p^d), \quad (2.12)$$

where the scattering strength  $\bar{\xi}$  is a function of relative permittivity. The *field equation*, which describes the relationship between the scattered field and the induced current, can be written as

$$\bar{E}_p^{\text{scat}} = \bar{G}_S \cdot \bar{I}_p^d. \quad (2.13)$$

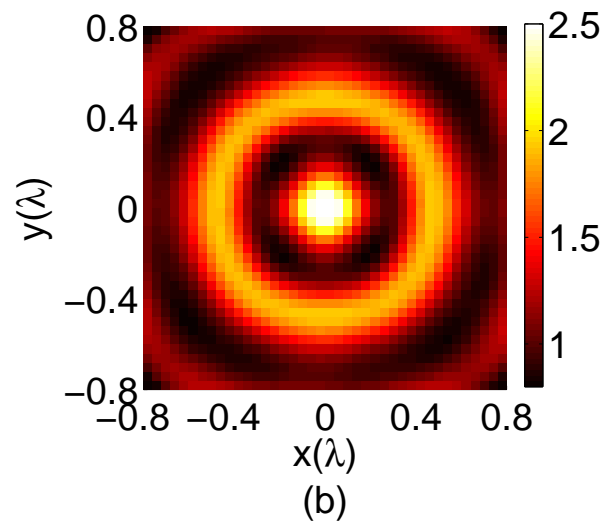
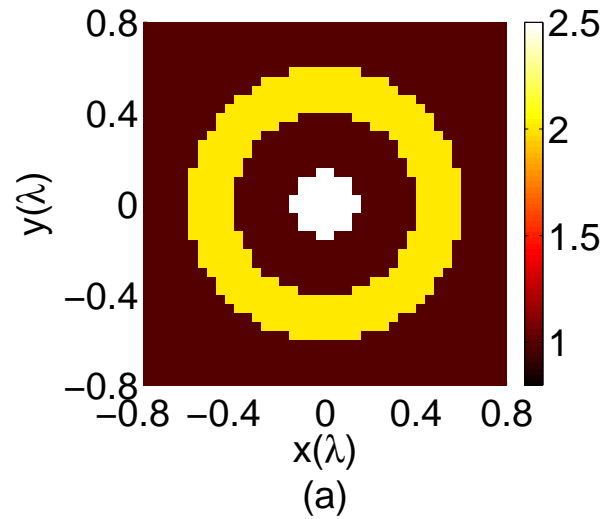


Figure 2.10: The pattern consisting of a circle and an annulus. (a) Exact relative permittivity. (b) Reconstructed relative permittivity with 10dB Gaussian white noise.

Table 2.1: Variables used in the formulation of the forward scattering problem

Variable Name	Size	Meaning
$\overline{E}_p^{\text{inc}}$	$2N_d \times 1$	electrical field incident to the scatter from the $p$ th transmitting antenna
$\overline{E}_p^{\text{scat}}$	$2N_r \times 1$	scattered electrical field due to $p$ th incidence
$\overline{I}_p^{\text{d}}$	$2N_d \times 1$	induced contrast displacement current due to $p$ th incidence
$\overline{\xi}$	$2N_d \times 2N_d$	diagonal matrix of scattering strength
$\overline{G}_S$	$2N_r \times 2N_d$	Green's function matrix describing the scattering from object to the receiving antennas
$\overline{G}_D$	$2N_d \times 2N_d$	Green's function matrix describing the multiple scattering effect

## 2.4.2 Subspace-based optimization method and its variants

The following is a brief review of the SOM. The SVD of  $\overline{G}_S$  can be expressed as  $\overline{G}_S = \overline{U} \cdot \overline{\Sigma} \cdot \overline{V}^*$ . The induced currents ( $\overline{I}_p^{\text{d}}$ ) on scatterers due to the  $p$ th incidence are partitioned into two orthogonally complementary portions (viz., the deterministic portion  $\overline{I}_p^{\text{s}}$  and the ambiguous portion  $\overline{I}_p^{\text{n}}$ ) in the following manner:  $\overline{I}_p^{\text{d}} = \overline{I}_p^{\text{s}} + \overline{I}_p^{\text{n}} = \overline{V}^{\text{s}} \cdot \overline{\alpha}_p^{\text{s}} + \overline{V}^{\text{n}} \cdot \overline{\alpha}_p^{\text{n}}$ , where  $\overline{V}^{\text{s}}$  (which comprises the first  $L$  right singular columns of the  $\overline{V}$  matrix [105]) is the basis of the signal subspace,  $\overline{V}^{\text{n}}$  (which comprises the last  $2N_d - L$  right singular columns of the  $\overline{V}$  matrix [105]) is the basis of the noise subspace,  $L$  is the total number of singular values in the  $\overline{\Sigma}$  matrix that are above a predefined noise-dependent threshold [120, 124–126], and  $\overline{\alpha}_p^{\text{s}}$  and  $\overline{\alpha}_p^{\text{n}}$  are two vectors of coefficients for the deterministic and ambiguous portions, respectively. The coefficients for the deterministic portion can be uniquely determined by the linear relationship, as conducted in [29]. After that, the ambiguous portion can be determined by three variants of SOM.

For the original SOM [29], the ambiguous portion is calculated by solving

the *field equation* in the least squares sense, and expressed as  $\bar{\alpha}_p^n(\bar{\xi}) = (\bar{A}^* \cdot \bar{A})^{-1}(\bar{A}^* \cdot \bar{B}_p)$ , where  $\bar{A} = \bar{V}^n - \bar{\xi} \cdot \bar{G}_D \cdot \bar{V}^n$ ,  $\bar{B}_p = \bar{\xi} \cdot (\bar{E}_p^{\text{inc}} + \bar{G}_D \cdot \bar{I}_p^s) - \bar{I}_p^s$ ,  $(\cdot)^*$  is the Hermitian operator. The scattering strength is determined by minimizing the objective function

$$f(\bar{\xi}) = \sum_{p=1}^{N_t} \frac{\|\bar{G}_S \cdot \bar{V}^n \cdot \bar{\alpha}_p^n(\bar{\xi}) + \bar{G}_S \cdot \bar{I}_p^s - \bar{E}_p^{\text{scat}}\|^2}{\|\bar{E}_p^{\text{scat}}\|^2} + \frac{\|\bar{A}(\bar{\xi}) \cdot \bar{\alpha}_p^n(\bar{\xi}) - \bar{B}_p(\bar{\xi})\|^2}{\|\bar{I}_p^s\|^2} \quad (2.14)$$

The Levenberg-Marquardt (LM) or conjugate gradient (CG) method can be used to solve for the unknowns.

For the CSI-like SOM [120], not only  $\bar{\xi}$  but also the ambiguous portion ( $\bar{\alpha}_p^n$ ) are regarded as unknown variables, and a different objective function is minimized

$$f(\bar{\alpha}_1^n, \bar{\alpha}_2^n, \dots, \bar{\alpha}_{N_t}^n, \bar{\xi}) = \sum_{p=1}^{N_t} \frac{\|\bar{G}_S \cdot \bar{V}^n \cdot \bar{\alpha}_p^n + \bar{G}_S \cdot \bar{I}_p^s - \bar{E}_p^{\text{scat}}\|^2}{\|\bar{E}_p^{\text{scat}}\|^2} + \frac{\|\bar{A}(\bar{\xi}) \cdot \bar{\alpha}_p^n - \bar{B}_p(\bar{\xi})\|^2}{\|\bar{I}_p^s\|^2} \quad (2.15)$$

by alternatively updating  $\bar{\alpha}_p^n$  and  $\bar{\xi}$ .

In this chapter, we propose a new variant of SOM, where the objective function is also Eq. (2.15), the same as the one in CSI-like SOM, while both  $\bar{\alpha}_p^n$  and  $\bar{\xi}$  are concurrently updated in each iteration using conjugate gradient method. The idea can be expressed as the following algorithm, where  $\bar{x} = [\bar{\alpha}_1^T, \bar{\alpha}_2^T, \dots, \bar{\alpha}_{N_t}^T, \bar{\xi}^T]^T$ ,  $\bar{\xi}$  denotes a column vector formed from the elements of the main diagonal of  $\bar{\xi}$ , the superscript T denotes the transpose operator.

Step 1 Calculate  $\bar{G}_S$ ,  $\bar{G}_D$ , and obtain  $\bar{I}_p^s$  using the SVD of  $\bar{G}_S$  ;

Step 2 Initial step,  $k=0$ .

2.1 Make initial guess:  $\bar{\xi}_0$  is obtained by using free space as the starting position ( $\varepsilon(\mathbf{r}_m) = 1$ ,  $m = 1, 2, \dots, N_d$ ); set  $\bar{\alpha}_{p,0}^n = 0$ , where  $p =$

$1, 2, \dots, N_t$ ; let  $\bar{x}_0 = [\bar{\alpha}_{1,0}^T, \bar{\alpha}_{2,0}^T, \dots, \bar{\alpha}_{N_t,0}^T, \bar{\xi}_0^T]^T$ .

2.2 Evaluate cost function:  $f_0 = f(\bar{x}_0)$ .

2.3 Set search direction:  $\bar{p}_0 = -\nabla_{\bar{x}} f_0$ .

Step 3 3.1 Compute step length  $a_k$  using one-dimensional line search algorithm.

3.2 Update variables by setting  $\bar{x}_{k+1} = \bar{x}_k + a_k \bar{p}_k$ ;

3.3 Calculate next search direction  $\bar{p}_{k+1} = -\nabla_{\bar{x}} f_{k+1} + \beta_{k+1} \bar{p}_k$ , where

$$\beta_{k+1} = \frac{\nabla_{\bar{x}} f_{k+1}^T \nabla_{\bar{x}} f_{k+1}}{\nabla_{\bar{x}} f_k^T \nabla_{\bar{x}} f_k} \text{ and } f_{k+1} = f(\bar{x}_{k+1}),$$

Step 4 If the termination criterion is met, stop iteration; otherwise  $k = k + 1$ , go to Step 3.

When CG is used in the CSI-like SOM, the step length has an analytical solution [120], but this is not the case for the new variant, where, instead, the one-dimensional line search algorithm presented in [127] is used to determine the step length  $a_k$ . The idea of the line search algorithm is that we try out a sequence of candidate values for the step length, and stop to accept one of these values when certain conditions, such as the Wolfe conditions [127], are satisfied. The difference in how to calculate step length may cause the computational cost per iteration of the new variant to be higher than that of the CSI-like SOM.

### 2.4.3 Numerical Simulations and Comparisons

In this section, we intend to evaluate and compare the three variants' performance, such as the computational cost and the quality of the reconstructed profile. For this purpose, we will utilize the three methods to reconstruct a number of complex patterns. For a fair comparison, CG instead of LM is used in the original SOM. Because the fast Fourier transform (FFT) cannot be readily applied for an



arbitrary shape of domain, it is not used in CSI-like SOM for the generality of the comparison. The data reported in this section are based on our simulations on a IBM workstation with 16 GB memory and two Intel Octal-Core Xeon processors at 2.83 GHz.

The numerical experiments are designed based on the idea that different working conditions should be considered in order to make a relatively exhaustive assessment.

- (I) We have considered different complexity levels of the patterns of scatterers. For example, the square pattern in Experiment 1 is the easiest one; and the Austria pattern in Experiment 6 is the most difficult one.
- (II) We have considered different noise levels. After showing the first two experiments, which are performed under relatively lower noise level, we intentionally chose a very high noise level (higher than most normal cases) for the remaining experiments. Consequently, we suppose the conclusions obtained from these simulations are convincingly valid for common inverse scattering problems.
- (III) We have considered both the lossless and the lossy scatterers. For example, the scatterers in the first two experiments are objects with conductivity, and the scatterers in the remaining experiments are lossless.
- (IV) We have also considered the special case where the scatterer profile consists of parts with different permittivities, as shown in Experiment 5.

For all the following numerical simulations, the same set of values are assigned to the following parameters.  $N_t$  line sources (transmitting antennas) are evenly

distributed on a circle of radius  $5\lambda$ , with locations  $(5\lambda \cdot \cos \frac{2\pi p}{N_t}, 5\lambda \cdot \sin \frac{2\pi p}{N_t})$   $p = 1, 2, \dots, N_t$ . A total number of  $N_r$  receivers are also evenly distributed on a circle of radius  $5\lambda$ , with locations  $(5\lambda \cdot \cos \frac{2\pi q}{N_r}, 5\lambda \cdot \sin \frac{2\pi q}{N_r})$   $q = 1, 2, \dots, N_r$ . The scattered field is recorded in the format of the multi-static response (MSR) matrix  $\overline{\overline{K}}$  whose size is  $2N_r \times N_t$  [30]. White Gaussian noise (WGN)  $\overline{\overline{\kappa}}$  is thereafter added to the MSR matrix, and the resultant noise-corrupted matrix  $\overline{\overline{K}} + \overline{\overline{\kappa}}$  is treated as the measured MSR matrix which is used to reconstruct the scatterers. The noise level is quantified in percentage form as  $\rho = \frac{\|\overline{\overline{\kappa}}\|_F}{\|\overline{\overline{K}}\|_F} \cdot 100\%$ , where  $\|\cdot\|_F$  denotes the Frobenius norm of a matrix. We choose free space as the initial guess in the optimization problem, i.e.,  $\varepsilon_r(\mathbf{r}_m) = 1$ ,  $m = 1, 2, \dots, N_d$ .

The choice of  $N_t$  and  $N_r$  determines the number of independent data and the choice of  $N_d$  determines the number of unknown data; these choices play a critical role when the deterministic optimizer is used to solve the inverse scattering problem. It has also been pointed out that in order to avoid local minima it is necessary to increase the ratio between the number of independent data and the number of unknown parameters [96, 123, 128]. Consequentially, once  $N_t$  and  $N_r$  have been fixed, it is not sensible to overly refine the grid of discretization (i.e., to set  $N_d$  a overly large number) in the presence of false solutions. On the other hand, higher value of  $N_t$ ,  $N_r$ , and  $N_d$  will incur higher measurement or computational cost. In our experiment, the values of these parameters are chosen the same as it was done for similar cases in the previously published papers [29, 105, 126, 129], where the configurations have been shown to be efficient.

The issue of choosing the number of leading singular values  $L$  has been well studied in [29, 105, 129], and it has been observed that there is a wide continuous

range of integer values of  $L$  yielding satisfactory reconstruction results. In our simulations, an empirical guideline is adopted and proves to be practically helpful, i.e., we choose  $L$  to be the largest integer so that the  $L$ th singular value is larger than  $\sigma_{\max} \cdot \rho$ , with  $\sigma_{\max}$  being the largest singular value of the SVD of  $\overline{\overline{G}}_S$ . The convergence criterion is defined as that the optimization terminates if either of the following two conditions is fulfilled: (1) there is little reduction of the cost function (for example,  $\Delta f < 0.01$ ) in five consecutive iterations; (2) the value of cost function becomes smaller than a tolerance value, which is given by an empirical formula,  $tol \approx N_t \cdot \frac{\rho^2}{(1 + \rho)^2}$ . The idea for setting such a tolerance value is that, in the objective functions, Eq. (2.14) and Eq. (2.15), the total relative mismatch accounts for all  $N_t$  incidences, and once the total relative residue is reduced to the order of relative noise, the optimization algorithm should be stopped [5]. The empirical rules for choosing  $L$  and  $tol$  require the value of noise level, which may not be difficult or expensive to measure or estimate in some applications. Even if the noise level is unavailable, we can still deliberately choose a value which, based on common sense, must be higher than the real noise level, for instance 30% or 40%, and then apply the empirical rules. The resultant parameters  $L$  and  $tol$  obtained this way are also conservative estimates. Fortunately, it has been shown that conservative choice of the parameters can still produce satisfactory reconstruction patterns in our numerical experiments [29, 105, 129]. The only loss due to the unavailability of noise level is the higher computational cost, which is caused by the smaller dimension of signal subspace.

### 2.4.3.1 Experiment 1: the pattern of a square

The first experiment considers a lossy scatterer with square pattern ( $0.4\lambda \times 0.4\lambda$ ) and relative permittivity of  $1.5 + 0.2i$ , in the presence of 10% noise, which corresponds to the signal-to-noise ratio (SNR) 20dB. The object is centered at the origin of the  $x$ - $y$  plane and the selected domain (which is a square of  $0.8\lambda$  for each side) has been discretized into a grid of  $25 \times 25$  subunits.  $N_t = 10$  transmitting antennas and  $N_r = 30$  receiving antennas are placed around the domain. The number of leading singular values  $L$  is chosen to be 11. The exact pattern and the inversion results obtained using the original SOM, CSI-like SOM, and the new variant are presented in Fig. 2.11(a)(b)(c)(d), respectively. The number of iterations needed to reach convergence and the computational time per iteration are listed in Table 2.2.

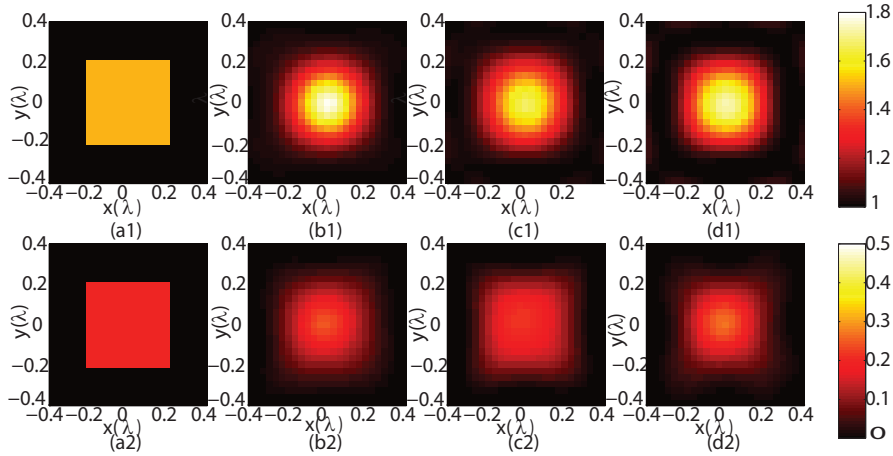


Figure 2.11: The pattern of an annulus. (a1),(a2) Exact patterns of the real part and the imaginary part of relative permittivity. (b1),(b2) Reconstructed patterns of the real part and the imaginary part using the original SOM under 10% Gaussian white noise. (c1),(c2) Reconstructed patterns of the real part and the imaginary part using the CSI-like SOM under 10% Gaussian white noise. (d1),(d2) Reconstructed patterns of the real part and the imaginary part using the novel variant of SOM under 10% Gaussian white noise.

## 2.4.3.2 Experiment 2: the pattern of a hollow square

In our second experiment, we consider a lossy scatterer with hollow square pattern and relative permittivity of  $1.5 + 0.2i$  in the presence of 10% noise. The size of the pattern is  $0.55\lambda \times 0.55\lambda$ , and the central hole is  $0.25\lambda \times 0.25\lambda$ . The object is centered at the origin of the  $x$ - $y$  plane and the selected domain (which is a square of  $0.8\lambda$  for each side) has been discretized into a grid of  $25 \times 25$  subunits.  $N_t = 10$  transmitting antennas and  $N_r = 30$  receiving antennas are placed around the domain. The number of leading singular values  $L$  is chosen to be 11. The exact pattern and the inversion results obtained using the original SOM, CSI-like SOM, and the new variant are presented in Fig. 2.12(a)(b)(c)(d), respectively. The number of iterations needed to reach convergence and the computational time per iteration are listed in Table 2.2.

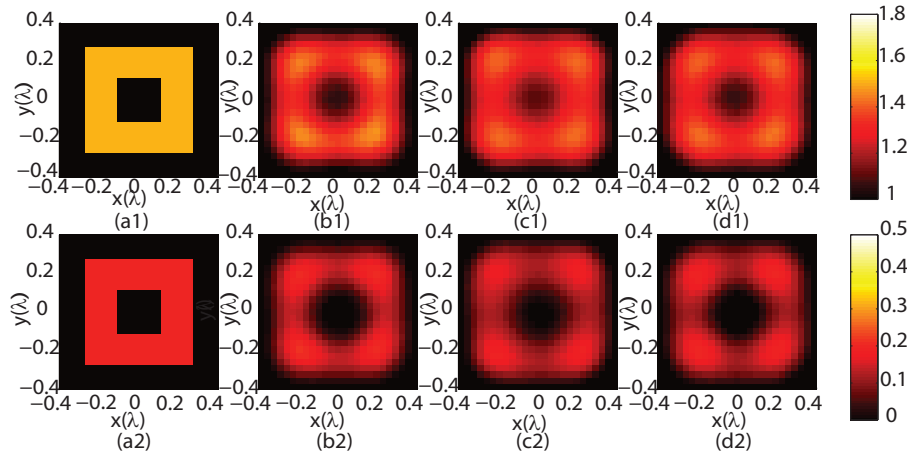


Figure 2.12: The pattern of a hollow square. (a1),(a2) Exact patterns of the real part and the imaginary part of relative permittivity. (b1),(b2) Reconstructed patterns of the real part and the imaginary part using the original SOM under 10% Gaussian white noise. (c1),(c2) Reconstructed patterns of the real part and the imaginary part using the CSI-like SOM under 10% Gaussian white noise. (d1),(d2) Reconstructed patterns of the real part and the imaginary part using the novel variant of SOM under 10% Gaussian white noise.

Table 2.2: Comparison of the performance of the three variants of SOM in the numerical experiments

	Original SOM		CSI-like SOM		New variant of SOM	
	Number of iterations	Time per iteration (s)	Number of iterations	Time per iteration (s)	Number of iterations	Time per iteration (s)
Exp. 1	10	17.4	28	0.14	19	0.84
Exp. 2	7	17.7	30	0.14	23	0.82
Exp. 3	5	16.5	9	0.13	7	0.64
Exp. 4	15	211	18	0.91	40	4.3
Exp. 5	6	267	12	0.92	8	4.5
Exp. 6	12	256	40	0.93	30	4.6

### 2.4.3.3 Experiment 3: the pattern of an annulus

The third experiment considers the pattern of an annulus in the presence of 31.6% noise, which corresponds to the signal-to-noise ratio (SNR) 10dB. The annular scatterer (with relative permittivity of 3 and inner and outer radii of  $0.15\lambda$  and  $0.3\lambda$  respectively) is centered at the origin of the  $x$ - $y$  plane and the selected domain (which is a square of  $0.8\lambda$  for each side) has been discretized into a grid of  $25 \times 25$  subunits.  $N_t = 10$  transmitting antennas and  $N_r = 30$  receiving antennas are placed around the domain. The number of leading singular values  $L$  is chosen to be 9. The exact pattern and the inversion results obtained using the original SOM, CSI-like SOM, and the new variant are presented in Fig. 2.13(a)(b)(c)(d), respectively. The number of iterations needed to reach convergence and the computational time per iteration are listed in Table 2.2.

### 2.4.3.4 Experiment 4: the pattern of two overlapping annuli

Our fourth numerical experiment considers the structure of two overlapping annuli, which are situated at  $(0.2\lambda, 0.2\lambda)$  and  $(-0.2\lambda, -0.2\lambda)$  in the  $x$ - $y$  coordinate system respectively, with relative permittivity being  $\varepsilon_r = 2$ . The inner and outer

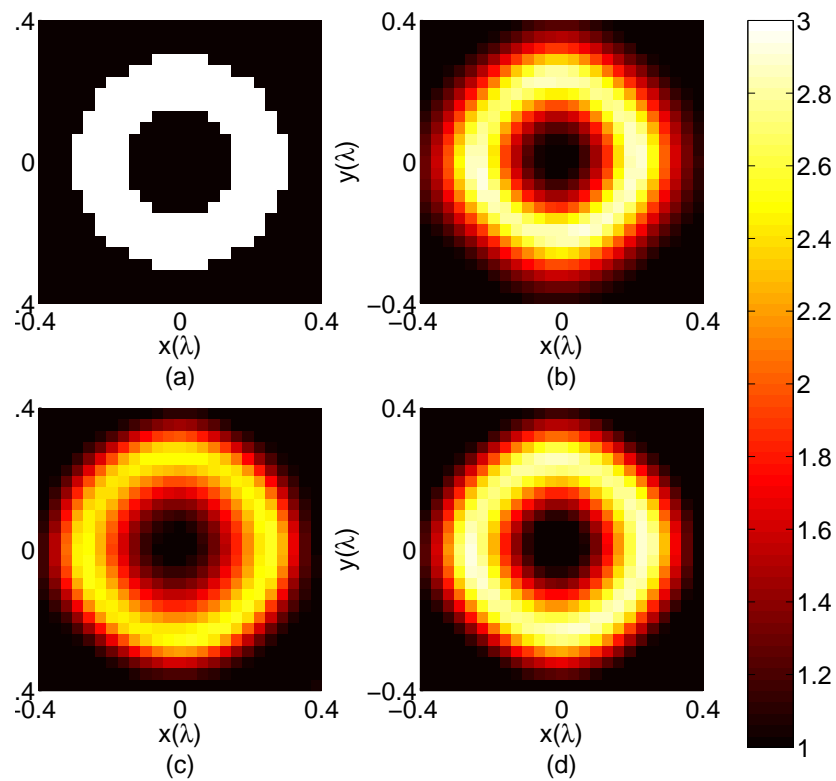


Figure 2.13: The pattern of an annulus. (a). Exact pattern of relative permittivity. (b) Reconstructed pattern using the original SOM under 31.6% Gaussian white noise. (c) Reconstructed pattern using the CSI-like SOM under 31.6% Gaussian white noise. (d) Reconstructed pattern using the novel variant of SOM under 31.6% Gaussian white noise.

radii of each annuli are  $0.5\lambda$  and  $0.7\lambda$  respectively. The square domain ( $2\lambda \times 2\lambda$ ) is centered at the origin, and discretized into a grid of  $40 \times 40$  subunits. The number of transmitting antennas is  $N_t = 10$ , and the number of receiving antennas is  $N_r = 30$ . In addition,  $L$  is chosen to be 19, and 31.6% noise is added into the scattering data. The exact pattern is shown in Fig. 2.14(a), and the inversion result obtained using the three variants of SOM in Fig. 2.14(b)(c)(d) respectively. The number of iterations needed to reach convergence and the computational time per iteration are listed in Table 2.2.

Compared with the original SOM, The CSI-like SOM and the new variant of SOM give slightly better reconstructed patterns, which are closer to exact pattern. The number of iterations needed to reach convergence and the computational time per iteration are listed in Table 2.2, where the CSI-like SOM requires fewest iterations and lowest time per iteration, while the original SOM is slowest.

#### 2.4.3.5 Experiment 5: the pattern of a circle and a concentric annulus

In the fifth example, we try to reconstruct the pattern of a circle and a concentric annulus in the presence of 31.6% noise. The circle (with relative permittivity of 2 and radius of  $0.15\lambda$ ) is placed in the central hole of a concentric annulus (with relative permittivity of 3 and inner and outer radii of  $0.4\lambda$  and  $0.6\lambda$  respectively). For the domain of interest, we have chosen a square region (with width of  $1.6\lambda$ ), which is discretized into a grid of  $40 \times 40$  subunits. The domain is surrounded by  $N_t = 14$  transmitting antennas and  $N_r = 30$  receiving antennas. We choose the number of leading singular values  $L$  to be 14. The exact pattern and the reconstructed results obtained using the three variants of SOM are presented in Fig. 2.15(a)(b)(c)(d) respectively. The number of iterations needed to reach



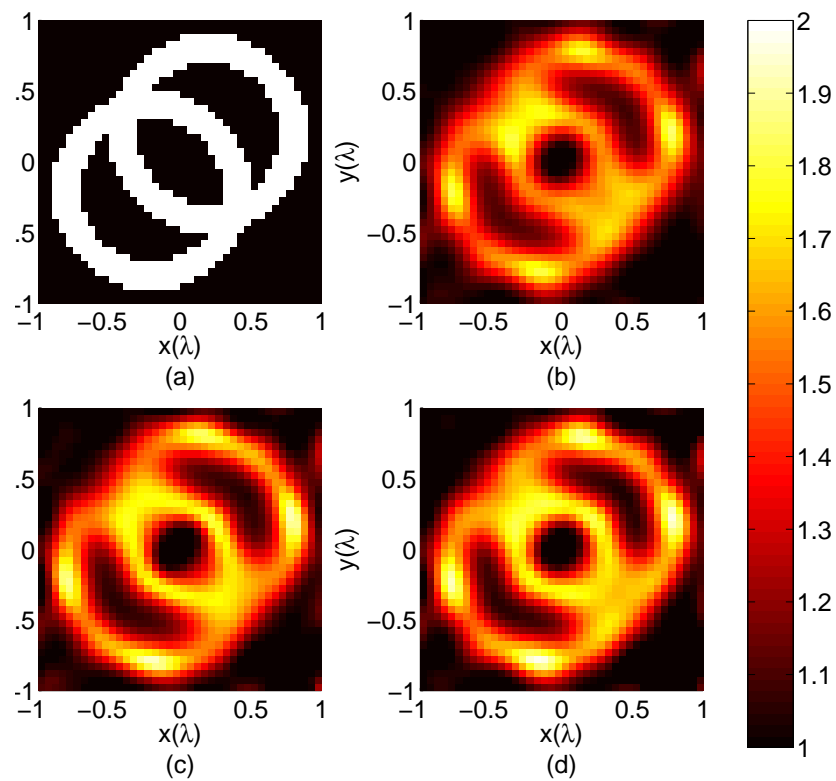


Figure 2.14: The pattern consisting of two overlapping annuli. (a). Exact pattern of relative permittivity. (b) Reconstructed pattern using the original SOM under 31.6% Gaussian white noise. (c) Reconstructed pattern using the CSI-like SOM under 31.6% Gaussian white noise. (d) Reconstructed pattern using the novel variant of SOM under 31.6% Gaussian white noise.

convergence and the computational time per iteration are listed in Table 2.2.

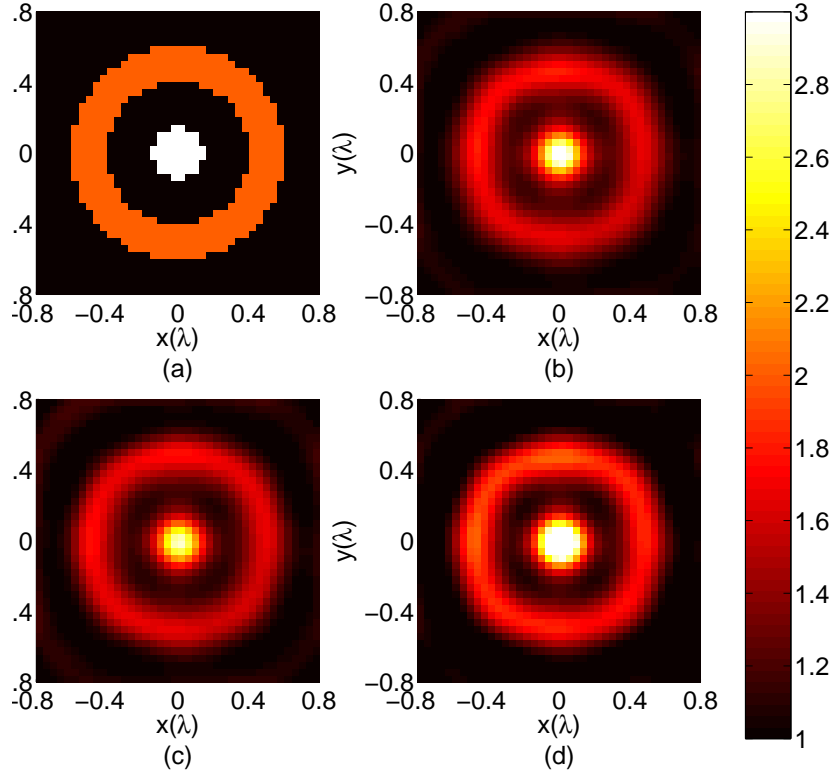


Figure 2.15: The pattern consisting of a circle and an annulus. (a). Exact pattern of relative permittivity. (b) Reconstructed pattern using the original SOM under 31.6% Gaussian white noise. (c) Reconstructed pattern using the CSI-like SOM under 31.6% Gaussian white noise. (d) Reconstructed pattern using the novel variant of SOM under 31.6% Gaussian white noise.

#### 2.4.3.6 Experiment 6: the 'Austria' profile

For the final example, we try to reconstruct the 'Austria' pattern in a square domain with width of  $2\lambda$  in the presence of 31.6% noise. The discs of radius  $0.2\lambda$  are centered at  $(0.3\lambda, 0.6\lambda)$  and  $(-0.3\lambda, 0.6\lambda)$ . The ring has an exterior radius of  $0.6\lambda$  and an inner radius of  $0.3\lambda$ , and is centered at  $(0\lambda, -0.2\lambda)$ . The relative permittivity of the discs and ring is 3. The domain is surrounded by  $N_t = 20$  transmitting antennas and  $N_r = 30$  receiving antennas. We choose the number of

leading singular values  $L$  to be 16. The exact pattern and the reconstructed results obtained using the three variants of SOM are presented in Fig. 2.16(a)(b)(c)(d) respectively. The number of iterations needed to reach convergence and the computational time per iteration are listed in Table 2.2.

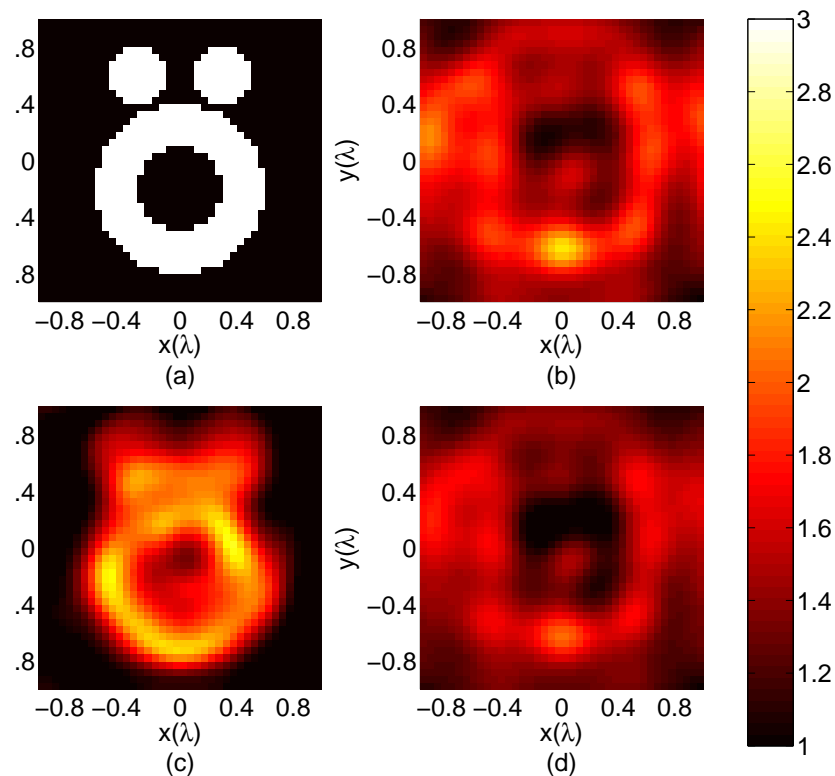


Figure 2.16: The Austria pattern. (a). Exact pattern of relative permittivity. (b) Reconstructed pattern using the original SOM under 31.6% Gaussian white noise. (c) Reconstructed pattern using the CSI-like SOM under 31.6% Gaussian white noise. (d) Reconstructed pattern using the novel variant of SOM under 31.6% Gaussian white noise.

#### 2.4.3.7 Comparison and discussion

An investigation into the simulation results in Fig. 2.11, Fig. 2.12, Fig. 2.13, Fig. 2.14, Fig. 2.15, Fig. 2.16, and Table 2.2 generates the following performance assessment on the three variants.

- (a) The CSI-like SOM is capable of reconstructing the complex pattern that is beyond the capability of the other two methods, or in other words, although none of the deterministic methods is guaranteed to find the global optimum in highly nonlinear problems, the CSI-like SOM, compared with the other two variants, is more likely to converge to the global optimum. Fig. 2.11, Fig. 2.12, Fig. 2.13, Fig. 2.14, and Fig. 2.15 show that each of the three variants of SOM can successfully reconstruct the pattern of a square, a hollow square, an annulus, the pattern of two overlapping annuli, and the pattern of a circle and a concentric annulus, respectively. In Experiment 6, however, as shown in Fig. 2.16, only the CSI-like SOM can produce the reconstructed pattern which exhibits the contour of the exact pattern that is satisfactory considering the complexity of the pattern and the presence of 31.6% noise.
- (b) While it might seem intuitively reasonable that updating all the unknown variables concurrently in each iteration (as in the original SOM and the new variant of SOM) may take fewer iterations than updating them alternatively per iteration (as in the CSI-like SOM), this is not generally true. For instance, as shown in Table 2.2, in Experiment 1,2,3,5 and 6, the original SOM and the new variant take fewer iterations than the CSI-like SOM does, however, it is not the case in Experiment 4. This may be due to the key issue that the sampling of the solution space for these two types of optimization is different, although the landscape of the cost function is the same. Another possible but non-rigorous explanation which may be suggested is that when CG is utilized in the CSI-like SOM, the objective

function is quadratic in terms of the step length [120], so the step length can be readily obtained; when CG is utilized in the original SOM and the new variant of SOM, however, the dependence of the cost function upon the step length is so complicated that the step length has to be calculated through the one-dimensional line search algorithm (see Section 2.4.2), which may potentially increase the number of iterations required.

- (c) As shown in Table 2.2, the computational time per iteration of CSI-like SOM is approximately 1/4 of that of the new variant, while the computational time per iteration of the original SOM is significantly higher than that of the other two. This is mainly because the matrix inverse operation is required in the original SOM, but it is avoided in the other two methods. As a result, the computational complexity of CSI-like SOM and the new variant is  $\mathcal{O}(N_d^2)$ , while the computational complexity of the original SOM is  $\mathcal{O}(N_d^3)$ . In addition, the line search algorithm may incur more computational time for the original SOM and the new variant of SOM compared to the CSI-like SOM.
- (d) In terms of the total computational time (the product of number of iterations and the computational time per iteration), CSI-like SOM outperforms noticeably the other two variants.

## 2.5 Conclusion and Discussion

In sections 2.2 and 2.3, we extend the application of the FD-SOM to the TE case, within the frameworks of both CDM and MoM, so as to reconstruct the relative-permittivity profiles of extended scatterers in two-dimensional settings.

The results of the TE-incidence experiments confirm that the SOM algorithm is capable of reconstructing objects of complex shapes. What is more, the reconstructed patterns for the TE case exhibits better quality than those obtained under TM incidence. In our numerical experiments, the number of leading singular values ( $L$ ) acts to balance the error of the data equation and the error of the physical model.

In section 2.4, a comparative study on three variants of SOM is conducted on the basis of several numerical experiments, to find the optimal solution to the determination of the ambiguous portion, which has a dominant influence upon the computational cost and reconstruction capability of SOM. The simulation for TE case shows that the CSI-like SOM outperforms the other two methods, in that it requires lowest computational time to reach convergence; and it can reconstruct some complex patterns which is beyond the capability of the other two variants. The comparison made in the thesis provides useful guidelines for the use of SOM method in solving inverse scattering problems.

For a complete introduction to FD-SOM, it is worth mentioning its other important developments here. [107] proposed the twofold subspace-based optimization method (TSOM) boosting the convergence of optimization, by restricting the induced current in some lower-dimensional subspace and thereby generating a good initial guess. After that, the large computational complexity and memory demand due to singular value decomposition, as is one of the predominantly expensive parts of SOM, has been considerably ameliorated by the FFT twofold subspace-based optimization method (FFT-TSOM) [130], where the discrete Fourier bases are used to construct a current subspace that is a good

approximation to the original current subspace spanned by singular vectors.





# Phaseless Data Subspace-based Optimization Method

---

*“From a long view of the history of mankind – seen from, say, ten thousand years from now, there can be little doubt that the most significant event of the 19th century will be judged as Maxwell’s discovery of the laws of electrodynamics. The American Civil War will pale into provincial insignificance in comparison with this important scientific event of the same decade.”*

*–Richard Phillips Feynman*

## 3.1 Original contributions

It is commonly acknowledged that phase is generally more difficult to measure than amplitude. As a matter of fact, researchers have observed [2, 3, 94] that the accuracy of phase measurements cannot be guaranteed for operating frequencies approaching the millimeter-wave band and beyond. To overcome this inherent drawback, several methods have been proposed [97–99, 101–104, 131] to reconstruct the scatterers by utilizing only phaseless data so as to obviate the need for measuring phase. Due to the fact that the phase information of the field

is more prone to noise pollution than the amplitude information, under certain circumstances, these methods using only phaseless data are able to produce the same result as, or even better result than the methods using both amplitude and phase information can do.

Whereas the original version of the SOM outlined in [29, 105–107] requires the full set of amplitude and phase measurements for the scattered fields, we shall resort to the phaseless data approach and develop another version of the SOM to handle inverse scattering problems without recourse to phase measurements. To differentiate between these two versions of the SOM, we borrow the prefix terminology coined by other researchers [103]: the original SOM (based on the full set of data) and the revised SOM (based only on amplitude data) will, for convenience, be referred to as full data SOM (FD-SOM) and phaseless data SOM (PD-SOM), respectively. It should be worth highlighting that although we will capitalize on the SOM's two essential features of analyzing the spectrum of the scattering operator and partitioning the contrast source into two orthogonally complementary portions, the PD-SOM differs fundamentally from the FD-SOM due to the unavailability of phase data. The original contributions in this chapter may be summarized as follows:

- (a) Noting that the PD-SOM cannot follow the FD-SOM in employing the singular value decomposition (SVD) procedure to evaluate the deterministic portion of the induced currents, we have opted for a novel optimization method based on the dominant contribution to the scattered fields. And for determining the ambiguous portion and relative permittivity, we have decided to replace the objective function employed in the FD-SOM because of the

benefits that can be accrued by choosing a different definition for use in the PD-SOM.

- (b) Studies upon illumination's influence on microwave imaging [47, 132–136] have shown the significance and necessity of further research on transverse electric (TE) illumination. For example, [136] shows that the TE illumination can present better reconstruction accuracy compared to the TM illumination when dielectric scatterers are dealt with; and [47, 135] report that inversion of a combination of the TE and transverse magnetic (TM) illuminations, either simultaneously or alternatively, may produce the possibility of better reconstruction. Nevertheless, the numerical results reported thus far in the literature are predominantly for the TM case. Hence, in this chapter, we shall apply the PD-SOM to study several scatterers of complex geometries under TE incidence. But we should also add the claim that our proposed method can equally be extended to TM and 3-D inverse scattering problems as well.
- (c) We have found from our numerical trials that the PD-SOM is able to reconstruct patterns of complex geometry with rapid convergence even in the presence of high-level noise and there is less critical dependence on initial guesses when running the algorithm.

## 3.2 Formulation of forward scattering problem

We consider a two-dimensional configuration under TE incidence where the cylindrical dielectric scatterers (which are inhomogeneous in the  $x$ - $y$  plane but invariant in the  $z$  direction) are located in the domain  $\mathbf{D} \subset \mathbf{R}^2$  in the  $x$ - $y$  plane. As

depicted in Fig. 3.1,  $N_t$  unit magnetic-current line sources (with TE polarization) have been placed at  $\mathbf{r}_p^t$  ( $p = 1, 2, \dots, N_t$ ) in a circle around the domain  $\mathbf{D}$ . The dielectric scatterers are illuminated by each of these line sources successively in turn and Ampère's Law may be utilized to express the incident TE waves from the  $p$ th line source in the following form:  $\mathbf{H}_p^{\text{inc}}(\mathbf{r}) = \hat{\mathbf{z}}H_{z,p}^{\text{inc}}(\mathbf{r}) = \hat{\mathbf{z}}\frac{i}{4}H_0^{(1)}(k_0 \cdot |\mathbf{r}_p^t - \mathbf{r}|)$ , and  $\mathbf{E}_p^{\text{inc}}(\mathbf{r}) = \hat{\mathbf{x}}E_{x,p}^{\text{inc}}(\mathbf{r}) + \hat{\mathbf{y}}E_{y,p}^{\text{inc}}(\mathbf{r})$ . The scattered signal is then received by  $N_r$  receivers which are placed at  $\mathbf{r}_q^r$  ( $q = 1, 2, \dots, N_r$ ) in another circle surrounding the domain  $\mathbf{D}$ .

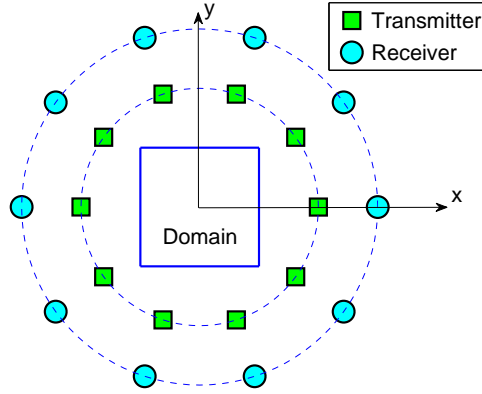


Figure 3.1: Geometry of the inverse scattering problem.

For the full data (FD) approach, there is a need to collate both amplitude and phase information of the scattered wave received by all of the  $N_r$  receivers. For the phaseless data (PD) approach, however, the available information is the intensity of the total received field (i.e., the sum of the scattered field and the field radiated by the transmitting antennas). The PD inverse problem thus consists of determining the relative permittivity ( $\varepsilon_r$ ) profile of the scatterers, given a set of  $2N_tN_r$  scattering data, where each data is a scalar intensity of  $x$  or  $y$  component of the total field. In practice, the domain  $\mathbf{D}$  is discretized into a total number of  $N_d$  subunits, with

the centers of the subunits located at  $\mathbf{r}_m$  ( $m = 1, 2, \dots, N_d$ ), and the PD inverse problem then reduces to determining  $\varepsilon_r(\mathbf{r}_m)$  instead.

Table 3.1: Variables used in the formulation of the forward scattering problem

Variable Name	Size	Meaning
$\overline{E}_p^{\text{inc}}$	$2N_d \times 1$	electrical field incident to the scatter from the $p$ th transmitting antenna
$\overline{E}_p^{\text{rad}}$	$2N_r \times 1$	electrical field incident to the receiving antennas from the $p$ th transmitting antenna
$\overline{E}_p^{\text{scat}}$	$2N_r \times 1$	scattered electrical field due to $p$ th incidence
$\overline{I}_p^{\text{d}}$	$2N_d \times 1$	induced contrast displacement current due to $p$ th incidence
$\overline{F}_p$	$2N_r \times 1$	square of intensity of total received field due to $p$ th incidence
$\overline{\xi}$	$2N_d \times 2N_d$	diagonal matrix of scattering strength
$\overline{G}_S$	$2N_r \times 2N_d$	Green's function matrix describing the scattering from object to the receiving antennas
$\overline{G}_D$	$2N_d \times 2N_d$	Green's function matrix describing the multiple scattering effect

Table 3.1 lists the variables required for the formulation of the forward scattering problem: of these variables, the definitions for  $\overline{E}_p^{\text{inc}}$ ,  $\overline{E}_p^{\text{scat}}$ ,  $\overline{I}_p^{\text{d}}$ ,  $\overline{\xi}$ ,  $\overline{G}_S$  and  $\overline{G}_D$  follow what we previously adopted in [105]. The variable  $\overline{E}_p^{\text{rad}}$ , which represents the field radiated by the  $p$ th transmitting antenna and received by the  $N_r$  receiving antennas, can be expressed as a column vector of size  $2N_r$  in the following manner:

$$\overline{E}_p^{\text{rad}} = [E_{p,x}^{\text{rad}}(\mathbf{r}_1^r), E_{p,x}^{\text{rad}}(\mathbf{r}_2^r), \dots, E_{p,x}^{\text{rad}}(\mathbf{r}_{N_r}^r), E_{p,y}^{\text{rad}}(\mathbf{r}_1^r), E_{p,y}^{\text{rad}}(\mathbf{r}_2^r), \dots, E_{p,y}^{\text{rad}}(\mathbf{r}_{N_r}^r)]^T.$$

Without any loss of generality, the phaseless data may conveniently be taken to be the square of the intensity of the total received field, and denoted by  $\mathbf{F}_p(\mathbf{r}_q^r)$ , where  $p = 1, 2, \dots, N_t$ ;  $q = 1, 2, \dots, N_r$ . It is known that the square of the

intensity of the total received field due to the  $p$ th transmitting antenna can be recast as a column vector of size  $2N_r$  in the following form:

$$\bar{F}_p = \left( \bar{E}_p^{\text{rad}} + \bar{E}_p^{\text{scat}} \right)^* \circ \left( \bar{E}_p^{\text{rad}} + \bar{E}_p^{\text{scat}} \right), \quad (3.1)$$

where  $\circ$  denotes the Hadamard product (or Schur product) [137], which is an element-wise product, and the superscript  $*$  denotes the complex conjugate.

We need to utilize two relationships to describe the forward scattering phenomenon. The first relationship, which describes how the induced contrast displacement current is generated by an incident field, can be expressed as

$$\bar{I}_p^{\text{d}} = \bar{\xi}(\bar{E}_p^{\text{inc}} + \bar{G}_D \cdot \bar{I}_p^{\text{d}}). \quad (3.2)$$

The second equation, which describes the relationship between the scattered field and the induced current, can be written as

$$\bar{E}_p^{\text{scat}} = \bar{G}_S \cdot \bar{I}_p^{\text{d}}. \quad (3.3)$$

Eq. (3.2) and Eq. (3.3) are referred to as the *state equation* and the *field equation*, respectively, and their detailed derivation has already been furnished in [105]. They, in conjunction with Eq. (3.1), the *intensity equation*, constitute the foundation for the PD inverse scattering problem.

### 3.3 Phaseless Data Subspace-based optimization method

In inverse scattering, the state equation remains the same for both PD and FD approaches. The essential difference between the two is that the intensity equation

for the PD approach is dissimilar from its counterpart, the field equation for the FD approach. Nevertheless, it is still possible to employ the SOM to solve the PD inverse scattering problem and we shall investigate in this section the similarities and differences between PD-SOM and FD-SOM.

The first step of PD-SOM is actually similar to that outlined for the FD-SOM ([29, 120, 129]). The SVD of  $\overline{\overline{G}}_S$  can be expressed as  $\overline{\overline{G}}_S = \overline{\overline{U}} \cdot \overline{\overline{\Sigma}} \cdot \overline{\overline{V}}^*$ . The induced currents ( $\overline{\overline{I}}_p^d$ ) on scatterers due to the  $p$ th incidence are partitioned into two orthogonally complementary portions (viz., the deterministic portion  $\overline{\overline{I}}_p^s$  and the ambiguous portion  $\overline{\overline{I}}_p^n$ ) in the following manner:  $\overline{\overline{I}}_p^d = \overline{\overline{I}}_p^s + \overline{\overline{I}}_p^n = \overline{\overline{V}}^s \cdot \overline{\overline{\alpha}}_p^s + \overline{\overline{V}}^n \cdot \overline{\overline{\alpha}}_p^n$ , where  $\overline{\overline{V}}^s$  (which comprises the first  $L$  right singular columns of the  $\overline{\overline{V}}$  matrix) is the basis of the signal subspace,  $\overline{\overline{V}}^n$  (which comprises the last  $2N_d - L$  right singular columns of the  $\overline{\overline{V}}$  matrix) is the basis of the noise subspace,  $L$  is the total number of singular values in the  $\overline{\overline{\Sigma}}$  matrix that are above a predefined noise-dependent threshold [29, 120, 129], and  $\overline{\overline{\alpha}}_p^s$  and  $\overline{\overline{\alpha}}_p^n$  are two vectors of coefficients for the deterministic and ambiguous portions, respectively. It should be pointed out that the deterministic portion and the ambiguous portion of the induced current are different from the radiating current and the non-radiating current commonly employed in, for example, [15, 48]. A detailed discussion on the difference between these two classifications has been provided earlier in [120, 126].

The second step of PD-SOM is for the purpose of evaluating the deterministic portion  $\overline{\overline{I}}_p^s$  (or, more specifically, its coefficient vector  $\overline{\overline{\alpha}}_p^s$ ). Although this can be handled by the SVD procedure for the FD-SOM, we are unable to proceed likewise for the PD-SOM because the mapping from the induced current to the measured data is no longer linear due to the lack of the phase information. If there is no  $\overline{\overline{E}}_p^{\text{rad}}$

term in our field expression, it is possible for the mapping to become linear by changing the bases as explained earlier in [129] (but then quadratic constraints will have to be introduced in the process). However, the presence of  $\overline{E}_p^{\text{rad}}$  here changes the linearity of the mapping.

Since the straightforward linear inversion in FD-SOM cannot be applied to the PD scenario and linear mapping cannot be realized as in the case without  $\overline{E}_p^{\text{rad}}$ , we need to explore other approaches to addressing the problem. From the fact that, in the first step, the deterministic portion corresponds to the first  $L$  largest singular values obtained in the SVD of  $\overline{\overline{G}}_S$ , we infer that the major contribution to the scattered electromagnetic field is due to the deterministic portion. It follows that the dominant contribution to the intensity of the total field is due to the  $\overline{E}_p^{\text{rad}}$  and the deterministic portion. This inference paves the way for estimating the deterministic portion  $\overline{T}_p^s$  by solving an nonlinear optimization problem. Using this idea, an objective function is proposed as follows,

$$\overline{\alpha}_p^s = \arg \min_{\overline{\alpha}_p^s} \left\| \overline{F}_{\text{mea},p} - \left( \overline{E}_p^{\text{rad}} + \overline{\overline{G}}_S \cdot \overline{\overline{V}}^s \cdot \overline{\alpha}_p^s \right)^* \circ \left( \overline{E}_p^{\text{rad}} + \overline{\overline{G}}_S \cdot \overline{\overline{V}}^s \cdot \overline{\alpha}_p^s \right) \right\|, \quad (3.4)$$

where  $\overline{F}_{\text{mea},p}$  denotes the square of the measured intensity vector due to the  $p$ th incidence. The objective function in this optimization problem is a quartic polynomial and the gradient of the function can be computed in a straightforward manner. Following [29] and references therein, the Levenberg-Marquardt (LM) algorithm, which is a mixture of the Gauss-Newton algorithm and the method of gradient decent, is efficient in solving nonlinear least squares problems. We employ the LM algorithm to minimize the error function, and we have found from the experience gained during our numerical simulations that the convergence is very



fast, which is shown by the numerical results in the next section.

After the deterministic portion has been evaluated, the third step of the PD-SOM is to determine the  $\bar{\varepsilon}_r$  profile of the scatterers by minimizing the sum of relative mismatches in both *state equation* and in *intensity equation*. The relative residue in the *state equation* is defined to be

$$\Delta^{\text{state}} = \sum_{p=1}^{N_t} \frac{\|\bar{A} \cdot \bar{\alpha}_p^n - \bar{B}_p\|^2}{\|\bar{I}_p^s\|^2}, \quad (3.5)$$

where  $\bar{A} = \bar{V}^n - \bar{\xi} \cdot \bar{G}_D \cdot \bar{V}^n$ , and  $\bar{B}_p = \bar{\xi} \cdot (\bar{E}_p^{\text{inc}} + \bar{G}_D \cdot \bar{I}_p^s) - \bar{I}_p^s$ . Due to the truncation of the singular values, the relative residue in the *intensity equation* can be defined as

$$\Delta^{\text{intensity}} = \sum_{p=1}^{N_t} \frac{\|\bar{F}_{\text{mea},p} - \bar{C}_p^* \circ \bar{C}_p\|^2}{\|\bar{F}_{\text{mea},p}\|^2}, \quad (3.6)$$

where  $\bar{C}_p = \bar{E}_p^{\text{rad}} + \bar{G}_S \cdot \bar{I}_p^s + \bar{G}_S \cdot \bar{V}^n \cdot \bar{\alpha}_p^n$ . It is recommended that  $\bar{\alpha}_p^n$  (which is also a function of  $\bar{\varepsilon}_r$ ) be obtained by the least squares solution [29], i.e.,  $\bar{\alpha}_p^n = (\bar{A}^* \cdot \bar{A})^{-1} \cdot (\bar{A}^* \cdot \bar{B}_p)$ .

The relative permittivity is obtained by minimizing the following objective function.

$$\bar{\varepsilon}_r = \arg \min_{\bar{\varepsilon}_r} (\Delta^{\text{state}} + \Delta^{\text{intensity}}). \quad (3.7)$$

We observe the following when utilizing the Levenberg-Marquardt algorithm to minimize the second objective function:

- (a) Computing the derivative of the objective function is more involved in the PD-SOM than that in the FD-SOM.
- (b) The relative mismatch in the state equation is the same for both PD-SOM and FD-SOM.

- (c) The relative mismatch in the intensity equation for the PD-SOM is quite different from its counterpart (i.e., the field equation for the FD-SOM) due to the lack of phase information.
- (d) The convergence can be rapidly reached, normally in 10 iterations. Please refer to the next section for details

### 3.4 Numerical results

The numerical results for the two examples presented in this section are based on the same set of values assigned to their configuration parameters. The line sources (serving as transmitting antennas) are evenly distributed on a circle of radius  $5\lambda$ , with their locations given by  $(5\lambda \cdot \cos \frac{2\pi p}{N_t}, 5\lambda \cdot \sin \frac{2\pi p}{N_t})$   $p = 1, 2, \dots, N_t$ . A total number of  $N_r = 30$  receivers are also evenly distributed on a circle of radius  $5.5\lambda$ , with their locations given by  $(5.5\lambda \cdot \cos \frac{2\pi q}{N_r}, 5.5\lambda \cdot \sin \frac{2\pi q}{N_r})$   $q = 1, 2, \dots, N_r$ . The reason for such a configuration of receivers and transmitters is simply to avoid the overlap between them, and numerical simulations show that the reconstruction is equally successful for many other configurations without overlap between transmitters and receivers. We first check the validity of the forward solver Eq. (3.2) and Eq. (3.3) by comparing with a different numerical method (viz., method of moments) [113]; we have since found that the difference between the scattered fields computed by these two methods is negligibly small and thus affirmed the validity of the forward solver. The scattered field is then recorded in the format of the multi-static response (MSR) matrix  $\overline{\overline{K}}$  with size of  $2N_r \times N_t$  [30]. White Gaussian noise  $\overline{\overline{\kappa}}$  is thereafter added to the MSR matrix, and the resultant noise-corrupted matrix  $\overline{\overline{K}} + \overline{\overline{\kappa}}$  is treated as the measured

MSR matrix which we utilized to reconstruct the scatterers. The noise level is quantified in percentage form as  $\frac{\|\overline{\kappa}\|_{\text{F}}}{\|\overline{K}\|_{\text{F}}} \cdot 100\%$ , where  $\|\cdot\|_{\text{F}}$  denotes the Frobenius norm of a matrix. We have found from preliminary trials that it is sufficient to select 20 and 10 iterations for the second and third steps, respectively, of the PD-SOM.

The first test structure is depicted in Fig. 3.3(a) where the annular scatterer (with relative permittivity of 2.5 and inner and outer radii of  $0.15\lambda$  and  $0.3\lambda$  respectively) is centered at the origin of the  $x$ - $y$  coordinate system and the selected domain (which is a square of  $0.8\lambda$  for each side) has been discretized into a grid of  $25 \times 25$  subunits. The reason for this particular choice of structure is that it was previously studied in [29, 105] for the FD case, where the reconstructions were based on both phase and amplitude data with 10% and 31.6% levels of noise added during the simulations. The numerical results reported in [29, 105] may thus be compared with what we can obtain here by utilizing only phaseless data where we have increased the noise level to 50% and employed  $N_{\text{t}} = 10$  transmitters successively in turn. When applying the SOM in the presence of noise, choosing an appropriate value for the number of leading singular values ( $L$ ) from the spectrum of the the matrix  $\overline{G_S}$  [29] not only improves the rate of convergence and the quality of the reconstructed patterns, but also strengthens the immunity to noise; we infer from the singular values plotted in Fig. 3.2 that  $L$  should be chosen as 9, where there is a noticeable change of slope in the spectrum of the matrix  $\overline{G_S}$ . To initiate the optimization process, it is convenient to choose free space with  $\varepsilon_{\text{r}}(\mathbf{r}_m) = 1$ ,  $m = 1, 2, \dots, N_{\text{d}}$  as the default for the initial guess. As can be seen from Fig. 3.3, the reconstructed pattern satisfactorily exhibits the scatterer's key features (including the annular contour and the central hole), which is rather

successful considering the 50% noise level. To the best of the author's knowledge, PD reconstruction result in presence of such high noise level has thus far not been reported.

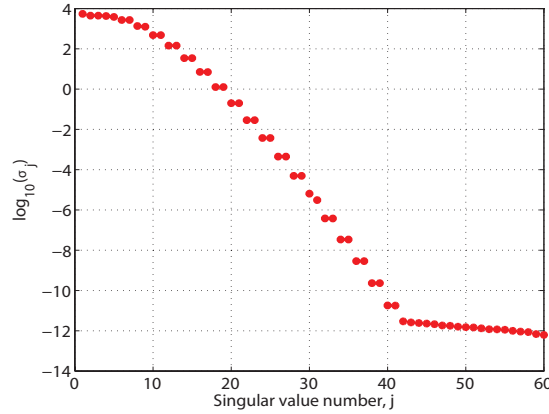


Figure 3.2: Singular values of the matrix  $\overline{G}_S$  in the first numerical simulation.

Other researchers [12, 14, 26–28] have cautioned that choosing a proper starting point is crucial for their algorithms to eventually yield satisfactory reconstructed results; e.g., the simulation example provided in Fig.5 of [103] shows a random initial guess failing to reconstruct the profile. Hence, there is a need for us to check the robustness of the PD-SOM to the choice of initial guesses. Starting from a random initial guess with  $\varepsilon_r$  assuming uniform distribution from 0 to 1, as portrayed in Fig. 3.4(a), we have found that the PD-SOM is still able to reconstruct the pattern reproduced in Fig. 3.4(b) where the key features of the annular contour and central hole remain evident even in presence of 50% white Gaussian noise. We have additionally repeated the experiment so as to test for  $L = 1$ , which is close to the contrast source inversion (CSI) due to that  $L$  cannot be zero [120], and the unsuccessful reconstruction in Fig. 3.4(c), where the key features are no longer discernible, highlights the significance of introducing spectrum analysis in

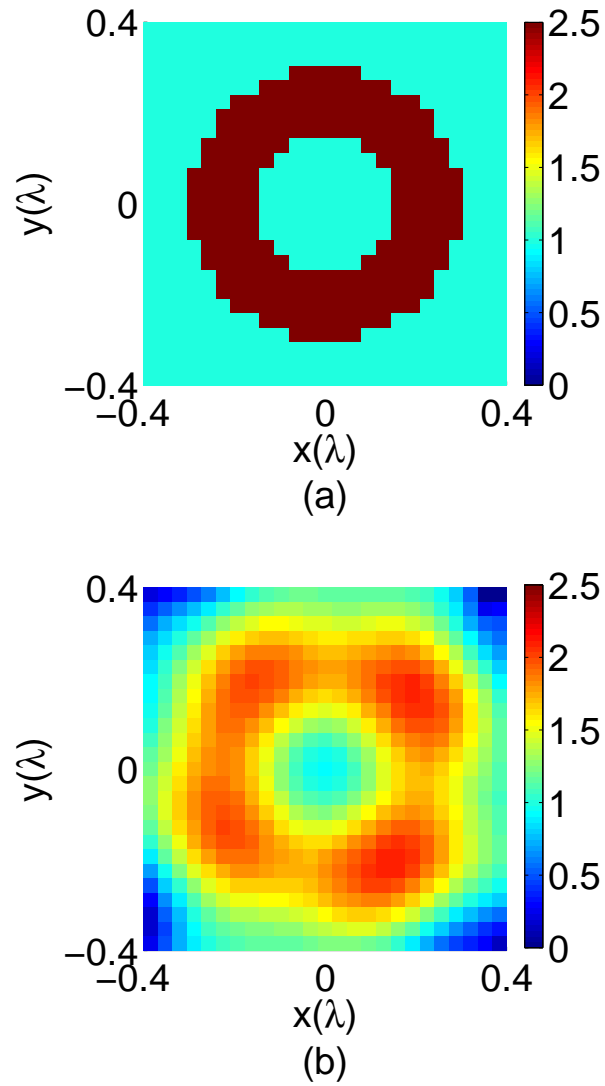


Figure 3.3: An annulus with inner radius  $0.15\lambda$  and outer radius  $0.3\lambda$ . (a). Exact relative permittivity. (b) Reconstructed relative permittivity with 50% Gaussian white noise.

the SOM. It has been observed in [120] that choosing a value of  $L$  that is either too large or too small will lead to poor reconstruction. However, the performance of the algorithm does not critically depend on the value of  $L$ , since there is a range of consecutive integers for  $L$ ; e.g., we observe that all integer values from 5 to 11 lead to reconstructions that are comparable to Fig. 3.4(b) for the annular structure in the presence of 50% white Gaussian noise.

The second test structure is more complex. As depicted in Fig. 3.5(a), a circle (with relative permittivity of 2 and radius of  $0.15\lambda$ ) is placed in the central hole of a concentric annulus (with relative permittivity of 1.6 and inner and outer radii of  $0.4\lambda$  and  $0.6\lambda$  respectively). For the domain of interest, we have chosen a square region (with width of  $1.6\lambda$ ), which is discretized into a grid of  $30 \times 30$  subunits. A similar pattern had previously been reconstructed in [105] by FD-SOM with  $N_t = 14$  transmitting antennas in the presence of 31.6% noise. The inverse result reconstructed by the PD-SOM is reproduced in Fig. 3.5(b) for the same set of operating parameters; even without the benefit of phase information, all the main features of the scatterer's structure can be identified clearly from the reconstructed pattern (including the gap with width of  $0.25\lambda$  between the central circle and the concentric annulus). To the best of the author's knowledge, such a complex structure has thus far not been adopted to test the PD retrieval algorithms.

In order to evaluate the convergence rate of the two optimizations (step 2 and step 3) used in PD-SOM, two convergence plots are exhibited in Fig. 3.6 and Fig. 3.7. Fig. 3.6 shows the convergence of the second step, i.e., to determine the deterministic portion, where "Experiment 1" means the reconstruction of an annulus from the initial guess of free space, as illustrated in Fig. 3.3; "Experiment

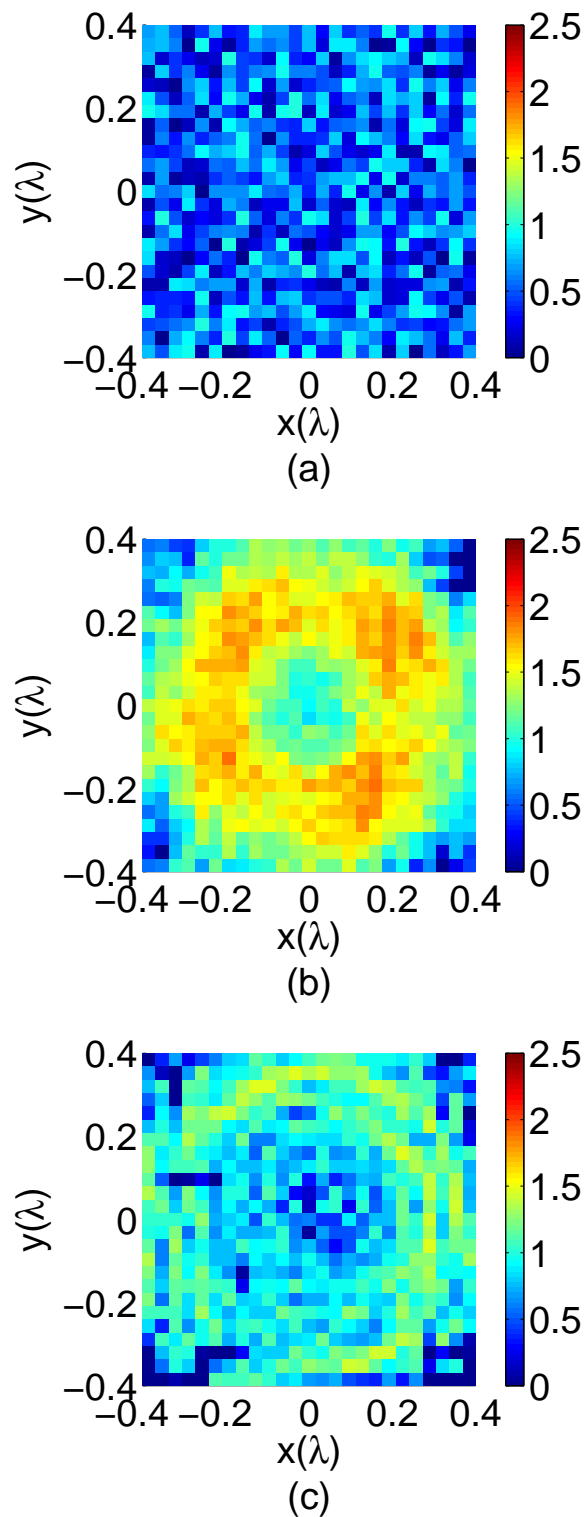


Figure 3.4: The exact relative permittivity pattern is shown in Fig. 3.3 (a). (a) Initial guess generated by random numbers. (b) Reconstructed relative permittivity with  $L = 9$ . (c) Reconstructed relative permittivity with  $L = 1$ .

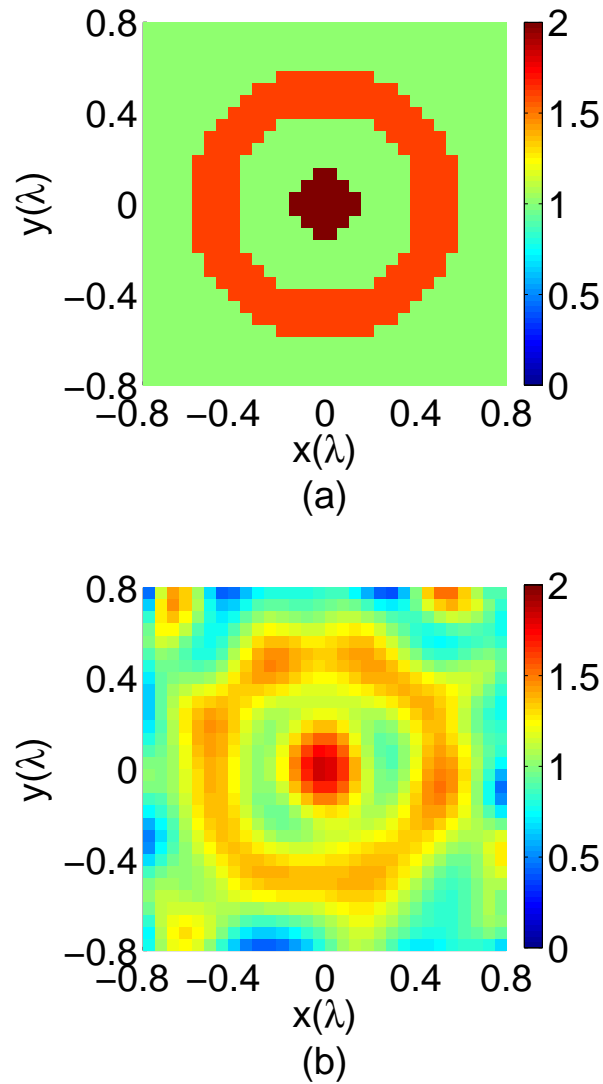


Figure 3.5: The pattern consisting of a circle and an annulus. (a) Exact relative permittivity, (b) Reconstructed relative permittivity with 31.6% Gaussian white noise.



"2" means the reconstruction of the pattern consisting of a circle and an annulus from free space initial guess, as illustrated in Fig. 3.5; and the residual is defined as the value of objective function, Eq. (3.4). It should be highlighted that although, for the sake of simplicity, only the result due to the first incidence is shown as a representative example of fast convergence, we have learnt from our numerical experience that the convergence rate is similar for the results due to other incidences. Fig. 3.7 shows the convergence of the third step, i.e., to determine the profile of relative permittivity, where the residual is defined to be the the value of objective function, Eq. (3.7). As shown in Fig. 3.6 and Fig. 3.7, it requires only 20 and 10 iterations to reach convergence for step 2 and step 3, respectively.

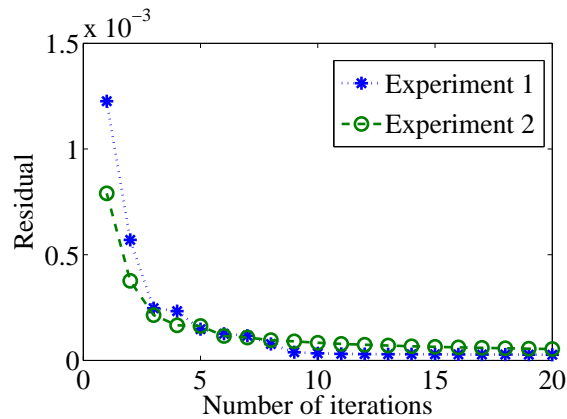


Figure 3.6: Residual versus number of iterations in the optimization for determining the deterministic portion corresponding to the first incidence. "Experiment 1" means the reconstruction of an annulus from the initial guess of free space, as illustrated in Fig. 3.3; "Experiment 2" means the reconstruction of the pattern consisting of a circle and an annulus from free space initial guess, as illustrated in Fig. 3.5; and the residual is defined as the value of objective function, Eq. (3.4).

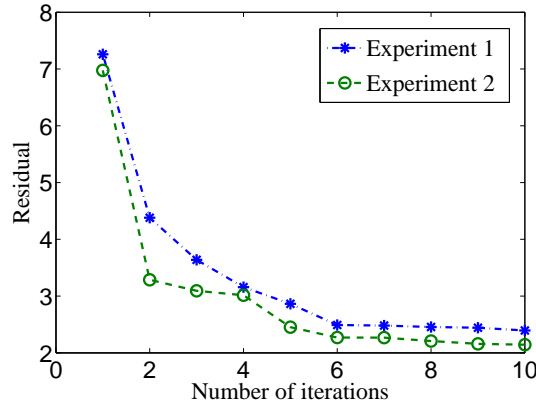


Figure 3.7: Absolute residue versus number of iterations in the optimization for determining relative permittivity. The residual is defined to be the value of objective function, Eq. (3.7).

### 3.5 Conclusion

In this section, we have proposed the novel PD-SOM for reconstructing the permittivity profiles of scatterers from phaseless measurements. In general, the lack of phase information has caused the inherent difficulty of the PD inverse scattering problem to be considerably higher when compared with its FD counterpart. Consequently, the PD-SOM is more complex than the FD-SOM. The principal difference between the two lies in the second step of the algorithm, where the PD-SOM requires a quartic polynomial to be minimized when solving for the deterministic portion of the induced current.

Two numerical experiments involving the TE-incident illumination of scatterers with complex shapes have been conducted in order to ascertain the performance of PD-SOM. The satisfactory resemblance of the reconstructed patterns Fig. 3.3 and Fig. 3.5 to their scatterers' geometrical and permittivity profiles offers convincing evidence that the PD-SOM is capable of reconstructing complicated patterns with rapid convergence (with only 20 and 10 iterations for second and third steps

respectively) and robust immunity to noise (of up to 50% and 31.6% for the two numerical experiments). It has also been observed in Fig. 3.4 that the PD-SOM shows reduced dependence on initial guesses due to the incorporation of spectrum analysis. Although our numerical results are for scatterers under TE incidence (since the corresponding case of TM incidence has been widely considered by others), it should be pointed out that the PD-SOM can be readily extended to 2-D TM and 3-D cases as well.



# Compressive Phaseless Imaging (CPI)

---

*“There is an enormous redundancy in every well-written book. With a well-written book I only read the right-hand page and allow my mind to work on the left-hand page. With a poorly written book I read every word.”*

*–Marshall McLuhan*

## 4.1 Original contributions

The novel approach to addressing the inverse scattering problem of small objects proposed in this chapter is motivated by the development of an emerging technique in the area of applied mathematics and signal processing, i.e. compressive sensing, also known as compressed sensing, compressive sampling, or sparse sampling. The recent explosion of this technique is attributed to the important contributions by Donoho, Candès, Romberg, and Tao [138–141]. Compressive sensing allows us to acquire and compress efficiently signals having a sparse or compressible representation in terms of an incoherent projecting basis or dictionary, and to reconstruct exactly the signal with overwhelming probability,

from dramatically under-sampled measurement, whose number is much lower than required by the celebrated Shannon-Nyquist theorem [140, 141]. For many physical signals in the real world being sparse in certain domain, compressive sensing has rapidly arrested considerable attention and interest in a broad diversity of applications, such as data compression, channel coding, data acquisition, and imaging applications (biomedical sensing, nondestructive testing) [142, 143].

A number of compressive-sensing-based approaches have been developed to address the inverse scattering problems by exploiting either basis pursuit techniques [81–83, 144, 145] or Bayesian approaches [84, 86]. In the former methods [81–83], high-frequency or Born approximations are used to linearize the intrinsically nonlinear inverse scattering problem, so as to recast it in the framework of compressive sensing where the location and the relative permittivity information are reconstructed. The latter methods [84, 85, 146] avoid the linear approximations by recasting successively the imaging problem into the framework of Bayesian compressive sampling (BCS), and invoking some prior (such as hierarchical sparseness prior or Laplace prior) to model the scatterers' geometry.

In this chapter, we aim at formulating the inverse scattering problem in the framework of compressive sensing in a manner without suffering the severe limitation caused by linear approximations. The proposed formulation consists of two steps. In the first step, the induced current is determined by basis pursuit technique, i.e., by solving a convex programming problem. After acquiring the induced current, the inverse problem is reduced to an over-determined linear problem of small size, and is therefore easily solved by least square methods in the second step. After that, the exact internal constitution in the domain of interest

can be reconstructed with overwhelming probability and computational efficiency.

## 4.2 Phaseless Imaging in the Framework of Compressive Sensing

### 4.2.1 Description of Physical Setup

We shall consider a two-dimensional scattering problem ( $\hat{\mathbf{z}}$  is the longitudinal direction) under time-harmonic (single frequency) transverse magnetic (TM) electromagnetic wave illumination. We shall first restrict formulation and algorithm to homogeneous background medium, free space for instance, and then extend them to heterogeneous background medium in Subsection 4.2.5. Since it is a scalar wave problem, we will henceforth conveniently suppress the unit vector  $\hat{\mathbf{z}}$ , wherever we refer to the electric field and the induced current throughout this chapter.

A total number of  $N_s$  scatterers of small yet finite size are embedded in a domain of interest  $\mathbf{D}$ , which is discretized into a total number of  $N_d$  subunits, with the centers of the subunits located at  $\mathbf{r}_m^d$  ( $m = 1, 2, \dots, N_d$ ), and the area and relative permittivity of the  $m$ th subunit are denoted by  $A_m$  and  $\varepsilon_r(\mathbf{r}_m)$ , respectively. The dimension of these small scatterers is much smaller than the wavelength, so that they are referred to as point-like scatterers, and consequently, for fine discretization, we can assume each point-like scatter just occupies a subunit with good approximation. The presence of point-like scatterers leads to the contrast in relative permittivity between the point-like scatters  $\varepsilon_r(\mathbf{r}_m^d)$  and the surrounding background medium  $\varepsilon_r^{\text{sm}}$ , which, for free space in our problem, is equal to 1. This

contrast, denoted by  $\chi(\mathbf{r}_m^d)$  ( $m = 1, 2, \dots, N_d$ ), is defined as

$$\chi(\mathbf{r}_m^d) = \begin{cases} \varepsilon_r(\mathbf{r}_m^d) - \varepsilon_r^{\text{sm}}, & \text{if the subunit is a point-like scatterer,} \\ 0, & \text{otherwise.} \end{cases}$$

In our problem, we assume the point-like scatterers are perfect (lossless) dielectric objects, so that the value of contrast is a real number. Outside the domain of interest  $\mathbf{D}$ , a total number of  $N_t$  transmitters (TX) are located at  $\mathbf{r}_p^t$  ( $p = 1, 2, \dots, N_t$ ), and they successively illuminate the domain. For the convenience of formulation, we consider the illumination of time harmonic electromagnetic wave due to unitary line sources. The scattered fields are received by a total number of  $N_r$  receivers (RX), which are arranged at  $\mathbf{r}_q^r$  ( $q = 1, 2, \dots, N_r$ ), also outside the domain of interest,

### 4.2.2 Formulation of scattering phenomenon in homogeneous background medium

The incident field from the  $p$ th TX at  $\mathbf{r}_p^t$  to the observation position  $\mathbf{r}$  is expressed as in Eq. (4.1).

$$E^{\text{inc}}(\mathbf{r}, \mathbf{r}_p^t) = -i\omega\mu \cdot g(\mathbf{r}, \mathbf{r}_p^t), \quad (4.1)$$

where  $\omega$  is temporal frequency,  $\mu$  is permeability,  $g(\mathbf{r}, \mathbf{r}_p^t) = \frac{i}{4} H_0^{(1)}(k_0 |\mathbf{r} - \mathbf{r}_p^t|)$  is the two-dimensional free space Green's function,  $H_0^1(\cdot)$  is Hankel function, and  $k_0$  stands for the free space wave number.

The total incident electric field onto the  $m$ th subunit at  $\mathbf{r}_m^d$ , due to the direct incidence from the  $p$ th TX at  $\mathbf{r}_p^t$  and the resultant scattering from other subunits, is denoted by  $E^{\text{tot}}(\mathbf{r}_m^d, \mathbf{r}_p^t)$ , and it satisfies the following self-consistent Foldy-Lax



equation [129, 147, 148], as shown in Eq. (4.2).

$$E^{\text{tot}}(\mathbf{r}_m^{\text{d}}, \mathbf{r}_p^{\text{t}}) = E^{\text{inc}}(\mathbf{r}_m^{\text{d}}, \mathbf{r}_p^{\text{t}}) + \sum_{\substack{n=1 \\ n \neq m}}^{N_d} k_0^2 \cdot A_n \cdot g(\mathbf{r}_m^{\text{d}}, \mathbf{r}_n^{\text{d}}) \cdot E^{\text{tot}}(\mathbf{r}_n^{\text{d}}, \mathbf{r}_p^{\text{t}}) \cdot \chi(\mathbf{r}_n^{\text{d}}), \quad (4.2)$$

The received field  $E^{\text{rec}}(\mathbf{r}_q^{\text{r}}, \mathbf{r}_p^{\text{t}})$  for the  $q$ th RX at  $\mathbf{r}_q^{\text{r}}$  due to the illumination from the  $p$ th RX at  $\mathbf{r}_p^{\text{t}}$  is the sum of two portions: the first portion is equal to the measured field in the absence of the small scatterers, denoted as  $E^{\text{rad}}(\mathbf{r}_q^{\text{r}}, \mathbf{r}_p^{\text{t}})$ , the second portion represents the influence of the presence of the point-like scatterers, and is denoted as  $E^{\text{pls}}(\mathbf{r}_q^{\text{r}}, \mathbf{r}_p^{\text{t}})$ , as expressed in Eq. (4.3).

$$E^{\text{rec}}(\mathbf{r}_q^{\text{r}}, \mathbf{r}_p^{\text{t}}) = E^{\text{rad}}(\mathbf{r}_q^{\text{r}}, \mathbf{r}_p^{\text{t}}) + E^{\text{pls}}(\mathbf{r}_q^{\text{r}}, \mathbf{r}_p^{\text{t}}). \quad (4.3)$$

For free space background medium,

$$E^{\text{rad}}(\mathbf{r}_q^{\text{r}}, \mathbf{r}_p^{\text{t}}) = -i\omega\mu \cdot g(\mathbf{r}_q^{\text{r}}, \mathbf{r}_p^{\text{t}}), \quad (4.4)$$

$$E^{\text{pls}}(\mathbf{r}_q^{\text{r}}, \mathbf{r}_p^{\text{t}}) = \sum_{n=1}^{N_d} k_0^2 \cdot A_n \cdot g(\mathbf{r}_q^{\text{r}}, \mathbf{r}_n^{\text{d}}) \cdot E^{\text{tot}}(\mathbf{r}_n^{\text{d}}, \mathbf{r}_p^{\text{t}}) \cdot \chi(\mathbf{r}_n^{\text{d}}). \quad (4.5)$$

The measured data is the intensity of total received electric field given by Eq. (4.6).

$$A^{\text{rec}}(\mathbf{r}_q^{\text{r}}, \mathbf{r}_p^{\text{t}}) = \sqrt{E^{\text{rec}}(\mathbf{r}_q^{\text{r}}, \mathbf{r}_p^{\text{t}}) E^{\text{rec}}(\mathbf{r}_q^{\text{r}}, \mathbf{r}_p^{\text{t}})^*}. \quad (4.6)$$

The forward scattering problem is to calculate the received intensity, given the contrast information in the domain of interest, and the inverse scattering problem is just the opposite, that is to determine the contrast information given the measured intensity. As demonstrated in Eq. (4.2) to Eq. (4.6), the inverse scattering problem is intrinsically nonlinear. Nevertheless, many linear approximate models are broadly applied in the regimes of optical imaging. A typical example among these models is the Born approximation [18, 112, 148, 149]. The Born approximation

states that the effect of multiple scattering can be neglected, and  $E^{\text{tot}}(\mathbf{r}_n^{\text{d}}, \mathbf{r}_p^{\text{t}})$  can be approximated by  $E^{\text{inc}}(\mathbf{r}_n^{\text{d}}, \mathbf{r}_p^{\text{t}})$  in the cases where scatterers having weak contrasts and small size are sufficiently separated. Eq. (4.7) follows as a consequence of applying Born approximation.

$$\begin{aligned}
E^{\text{pls}}(\mathbf{r}_q^{\text{r}}, \mathbf{r}_p^{\text{t}}) &\approx \sum_{n=1}^{N_{\text{d}}} k_0^2 \cdot A_n \cdot g(\mathbf{r}_q^{\text{r}}, \mathbf{r}_n^{\text{d}}) \cdot E^{\text{inc}}(\mathbf{r}_n^{\text{d}}, \mathbf{r}_p^{\text{t}}) \cdot \chi(\mathbf{r}_n^{\text{d}}) \\
&= \sum_{n=1}^{N_{\text{d}}} -i\omega\mu \cdot k_0^2 \cdot A_n \cdot g(\mathbf{r}_q^{\text{r}}, \mathbf{r}_n^{\text{d}}) \cdot g(\mathbf{r}_n^{\text{d}}, \mathbf{r}_p^{\text{t}}) \cdot \chi(\mathbf{r}_n^{\text{d}}) \quad (4.7) \\
&= \sum_{n=1}^{N_{\text{d}}} y_n^{\text{qp}} \cdot \chi(\mathbf{r}_n^{\text{d}}),
\end{aligned}$$

where we use the definition  $y_n^{\text{qp}} = -i\omega\mu \cdot k_0^2 \cdot A_n \cdot g(\mathbf{r}_q^{\text{r}}, \mathbf{r}_n^{\text{d}}) \cdot g(\mathbf{r}_n^{\text{d}}, \mathbf{r}_p^{\text{t}})$  to simplify the expression.

Without any loss of generality, the phaseless data may conveniently be taken to be the square of the intensity of the total received electric field, and denoted by  $F^{\text{rec}}(\mathbf{r}_q^{\text{r}}, \mathbf{r}_p^{\text{t}})$ , where  $p = 1, 2, \dots, N_{\text{t}}$ ;  $q = 1, 2, \dots, N_{\text{r}}$ , with the definition in Eq. (4.8).

$$\begin{aligned}
F^{\text{rec}}(\mathbf{r}_q^{\text{r}}, \mathbf{r}_p^{\text{t}}) &= E^{\text{rec}}(\mathbf{r}_q^{\text{r}}, \mathbf{r}_p^{\text{t}}) E^{\text{rec}}(\mathbf{r}_q^{\text{r}}, \mathbf{r}_p^{\text{t}})^* \\
&= [E^{\text{rad}}(\mathbf{r}_q^{\text{r}}, \mathbf{r}_p^{\text{t}}) + E^{\text{pls}}(\mathbf{r}_q^{\text{r}}, \mathbf{r}_p^{\text{t}})] [E^{\text{rad}}(\mathbf{r}_q^{\text{r}}, \mathbf{r}_p^{\text{t}}) + E^{\text{pls}}(\mathbf{r}_q^{\text{r}}, \mathbf{r}_p^{\text{t}})]^* \\
&= E^{\text{rad}}(\mathbf{r}_q^{\text{r}}, \mathbf{r}_p^{\text{t}}) E^{\text{rad}}(\mathbf{r}_q^{\text{r}}, \mathbf{r}_p^{\text{t}})^* + E^{\text{pls}}(\mathbf{r}_q^{\text{r}}, \mathbf{r}_p^{\text{t}}) E^{\text{pls}}(\mathbf{r}_q^{\text{r}}, \mathbf{r}_p^{\text{t}})^* \\
&\quad + 2\text{Re} \left\{ E^{\text{rad}}(\mathbf{r}_q^{\text{r}}, \mathbf{r}_p^{\text{t}}) E^{\text{pls}}(\mathbf{r}_q^{\text{r}}, \mathbf{r}_p^{\text{t}})^* \right\} \quad (4.8)
\end{aligned}$$

where the notation  $\text{Re}()$  stands for the real-part operator.

We define  $F^{\text{rad}}(\mathbf{r}_q^{\text{r}}, \mathbf{r}_p^{\text{t}}) = E^{\text{rad}}(\mathbf{r}_q^{\text{r}}, \mathbf{r}_p^{\text{t}}) E^{\text{rad}}(\mathbf{r}_q^{\text{r}}, \mathbf{r}_p^{\text{t}})^*$  and  $F^{\text{pls}}(\mathbf{r}_q^{\text{r}}, \mathbf{r}_p^{\text{t}}) = F^{\text{rec}}(\mathbf{r}_q^{\text{r}}, \mathbf{r}_p^{\text{t}}) - F^{\text{rad}}(\mathbf{r}_q^{\text{r}}, \mathbf{r}_p^{\text{t}})$ , and it is obvious that they are known information in

the phaseless imaging problem. Substitution with Eq. (4.7) yields

$$E^{\text{pls}}(\mathbf{r}_q^r, \mathbf{r}_p^t) E^{\text{pls}}(\mathbf{r}_q^r, \mathbf{r}_p^t)^* = \sum_{n=1}^{N_d} \sum_{m=1}^{N_d} y_n^{qp} \cdot y_m^{qp*} \cdot \chi(\mathbf{r}_n^d) \cdot \chi(\mathbf{r}_m^d),$$

and

$$2\text{Re} \left\{ E^{\text{rad}}(\mathbf{r}_q^r, \mathbf{r}_p^t) E^{\text{pls}}(\mathbf{r}_q^r, \mathbf{r}_p^t)^* \right\} = \sum_{m=1}^{N_d} 2\text{Re} \left\{ E^{\text{rad}}(\mathbf{r}_q^r, \mathbf{r}_p^t) y_m^{qp*} \right\} \cdot \chi(\mathbf{r}_m^d).$$

Now Eq. (4.8) is consequently transformed to

$$F^{\text{pls}}(\mathbf{r}_q^r, \mathbf{r}_p^t) = \sum_{m=1}^{N_d} 2\text{Re} \left\{ E^{\text{rad}}(\mathbf{r}_q^r, \mathbf{r}_p^t) y_m^{qp*} \right\} \cdot \chi(\mathbf{r}_m^d) + \sum_{n=1}^{N_d} \sum_{m=1}^{N_d} y_n^{qp} \cdot y_m^{qp*} \cdot \chi(\mathbf{r}_n^d) \cdot \chi(\mathbf{r}_m^d). \quad (4.9)$$

For convenience of description, we simplified the  $F^{\text{pls}}(\mathbf{r}_q^r, \mathbf{r}_p^t)$  and  $\chi(\mathbf{r}_m^d)$  to succinct notations  $F_{q,p}^{\text{pls}}$  and  $\chi_m$ . It is known that the square of the total received intensity can be recast as a column vector of length  $N_r N_t$  in the following form:

$$\overline{F}^{\text{pls}} = \left[ F_{1,1}^{\text{pls}}, F_{2,1}^{\text{pls}}, \dots, F_{N_r,1}^{\text{pls}}, F_{1,2}^{\text{pls}}, F_{2,2}^{\text{pls}}, \dots, F_{N_r,2}^{\text{pls}}, \dots, F_{1,N_t}^{\text{pls}}, F_{2,N_t}^{\text{pls}}, \dots, \dots, F_{N_r,N_t}^{\text{pls}} \right]^T,$$

where the superscript  $T$  stands for the transpose operator.

The contrast information can be recast as a column vector of length  $N_d$  in the following form:

$$\overline{\chi} = [\chi_1, \chi_2, \dots, \chi_{N_d}]^T.$$

We also build a vector of length  $N_d(N_d + 1)/2$  to record the information of the

products of contrast, which is written in a column vector as follows.

$$\begin{aligned} \bar{\lambda} = & [\chi_1\chi_1, \chi_1\chi_2, \chi_1\chi_3, \chi_1\chi_4 \cdots, \chi_1\chi_{N_d}, \\ & \chi_2\chi_2, \chi_2\chi_3, \chi_2\chi_4, \cdots, \chi_2\chi_{N_d}, \\ & \chi_3\chi_3, \chi_3\chi_4, \cdots, \chi_3\chi_{N_d}, \\ & \chi_4\chi_4, \cdots, \chi_4\chi_{N_d}, \\ & \cdots, \cdots, \cdots, \\ & \chi_{N_d}\chi_{N_d}]^T \end{aligned}$$

Combining  $\bar{\chi}$  and  $\bar{\lambda}$ , we define a vector  $\bar{\rho}$  of length  $N_d(N_d + 1)/2 + N_d$  as follows:

$$\bar{\rho} = [\bar{\chi}^T, \bar{\lambda}^T]^T.$$

Now Eq. (4.9) can be expressed in a compact form Eq. (4.10):

$$\bar{F}^{\text{pls}} = \bar{A}\bar{\rho} \quad (4.10)$$

where  $\bar{A}$  is a  $[N_r N_t]$ -by- $[N_d(N_d + 1)/2 + N_d]$  matrix, whose elements can be determined by the coefficients in Eq. (4.9). Now the phaseless imaging problem is reduced to finding the contrast vector  $\bar{\chi}$  given  $\bar{F}^{\text{pls}}$ .

### 4.2.3 Applicability of Compressive Sensing

We know, from Eq. (4.10) and the definition of vector  $\bar{\rho}$ , that the problem of recovering  $\bar{\chi}$  from  $\bar{F}^{\text{pls}}$  is intrinsically nonlinear, and therefore the framework of compressive sensing seems not applicable to this problem. However, if we simply ignore the complicated nonlinear relation between  $\bar{\chi}$  and  $\bar{\lambda}^T$  and treat each entry of  $\bar{\rho}$  as an independent variable, it can be regarded as a linear problem. This idea also provides the possibility of modeling the problem of imaging with phaseless data in

the framework of compressive sensing.

In order to evaluate the applicability of compressive sensing, we also examine two principles on which compressive sensing relies. These two principles are, as discussed in [141], sparsity, which pertains to the signal of interest, and incoherence, which pertains to the sensing modality. In the cases of sparsity and incoherence, the signal can be recovered accurately (or even perfectly) based on measurement by solving a convex programming problem.

In our modeling of the problem of imaging with phaseless measurement, the signal of interest corresponds to the contrast information, which is represented by vector  $\bar{\rho}$ . Suppose only  $S$  of the  $N_d$  subunits are occupied by the point-like scatterers ( $S \ll N_d$ ), the number of nonzero elements in vector  $\bar{\lambda}$  is  $S(S+1)/2$ , and the number of nonzero elements in vector  $\bar{\rho}$  is  $S + S(S+1)/2$ , thus  $\bar{\rho}$  can be regarded as a rather sparse signal, in view of the fact that the length of  $\bar{\rho}$  is  $N_d(N_d+1)/2 + N_d$ .

The random detector arrays has been a problem of longstanding interest for the purpose of improving the quality of imaging with a relatively small number of antennas [82, 83, 150, 151]. Recently, [82, 83] give a rigorous analysis of the single-input-multiple-output (SIMO), multiple-input-single-output (MISO), and multiple-input-multiple-output (MIMO) measurements for compressed sensing theory with and without the Born approximation. Furthermore, it is reported that random sensor arrays are consistent with the theory of compressive sensing, and is a good way of realizing incoherence measurement [150, 151]. The fulfillment of both sparsity and incoherence validates the applicability of compressive sensing in imaging with phaseless measurement.

#### 4.2.4 Phaseless Imaging with Compressive Sensing

By the compressive sensing theory, the problem of imaging with phaseless data can be transformed to a linear programming problem, that is, the location and electrical characteristics of the point-like scatterers can be accurately reconstructed from the randomly measured electromagnetic field with high probability. In the case of no noise or low noise, the sparse signal can be reconstructed by solving the following optimization problem as shown in (4.11).

$$\bar{\rho}^{\text{opt}} = \arg \min_{\bar{\rho}} \left\| \bar{\rho} \right\|_{l_0}, \text{ subject to } \bar{F}^{\text{pls}} = \bar{\bar{A}} \bar{\rho} \quad (4.11)$$

Since the  $l_0$ -norm minimization problem is non-deterministic polynomial-time hard and thus computationally infeasible, in practice, we consider instead its convex relaxation, which is also known as the basis pursuit (BP) problem as shown in (4.12), and can readily be solved by linear and quadratic programming techniques.

$$\bar{\rho}^{\text{opt}} = \arg \min_{\bar{\rho}} \left\| \bar{\rho} \right\|_{l_1}, \text{ subject to } \bar{F}^{\text{pls}} = \bar{\bar{A}} \bar{\rho} \quad (4.12)$$

After obtaining  $\bar{\rho}^{\text{opt}}$ , we can simply extract its first  $N_d$  elements, which is the recovered contrast vector  $\bar{\chi}$ .

Since the real measurement is inevitably corrupted by at least a small amount of noise, a robust reconstruction method should be able to overcome such non-ideality. Fortunately, the theorem of Compressive Sensing states that if we hold an “sensing matrix”  $\bar{\bar{A}}$  obeying the hypothesis of the restricted isometry property (RIP), robust and exact reconstruction from noisy data is still guaranteed [140, 141]. For phaseless imaging problem, the “sensing matrix”  $\bar{\bar{A}}$  is so complicated that theoretical validation of its RIP is not finished. However, the numerical simulation

in the next section successfully recover the signal by solving a linear programming problem with quadratic constraints, as shown in (4.13), or by solving a linear programming problem with residual correlation (also referred to as the Dantzig selector [152]), as shown in (4.14).

$$\bar{\rho}^{\text{opt}} = \arg \min_{\bar{\rho}} \left\| \bar{\rho} \right\|_{l_1}, \text{ subject to } \left\| (\bar{A} \cdot \bar{\rho} - \bar{F}^{\text{pls}}) \right\|_2 < \varepsilon \quad (4.13)$$

$$\bar{\rho}^{\text{opt}} = \arg \min_{\bar{\rho}} \left\| \bar{\rho} \right\|_{l_1}, \text{ subject to } \left\| \bar{A}^T (\bar{A} \cdot \bar{\rho} - \bar{F}^{\text{pls}}) \right\|_{\infty} < \varepsilon \quad (4.14)$$

#### 4.2.5 Phaseless Imaging of point-like scatterers in heterogeneous background medium

In many real world problems, such as through-wall imaging and nondestructive evaluation, it is often necessary to conduct phaseless imaging in heterogeneous background medium. Although the above-described approach is designed for imaging point-like scatterers embedded in homogeneous background medium, it is possible to extend the formulation and algorithm to the case of heterogeneous background medium, as long as the distribution and character of the objects, which form the heterogeneous medium background, are *a priori* information. It is noteworthy that the background-forming objects do not include the unknown point-like scatterers.

With the knowledge of the heterogeneous medium background, we are able to derive and calculate the four types of Green's functions listed in Table 4.1. Since Green's Function can be interpreted as a mapping from a unitary source to an observation point, we explain the meaning of the four types of Green's function by specifying the location of the unitary source and position of the observation point in the columns "From" and "To" of Table 4.1. Now, in order to generalize

Table 4.1: Four types of Green's functions

Green's Function	From	To
$g^{rt}(\mathbf{r}_q^r, \mathbf{r}_p^t)$	TX @ $\mathbf{r}_p^t$	RX @ $\mathbf{r}_q^r$
$g^{dt}(\mathbf{r}_m^d, \mathbf{r}_p^t)$	TX @ $\mathbf{r}_p^t$	Subunit @ $\mathbf{r}_m^d$
$g^{dd}(\mathbf{r}_n^d, \mathbf{r}_m^d)$	Subunit @ $\mathbf{r}_m^d$	Subunit @ $\mathbf{r}_n^d$
$g^{rd}(\mathbf{r}_q^r, \mathbf{r}_m^d)$	Subunit @ $\mathbf{r}_m^d$	RX @ $\mathbf{r}_q^r$

our formulation and approach to the case of heterogeneous background medium, the only necessary modification is to replace  $g(\mathbf{r}_n^d, \mathbf{r}_p^t)$ ,  $g(\mathbf{r}_q^r, \mathbf{r}_m^d)$ , and  $g(\mathbf{r}_q^r, \mathbf{r}_p^t)$  with  $g^{dt}(\mathbf{r}_n^d, \mathbf{r}_p^t)$ ,  $g^{rd}(\mathbf{r}_q^r, \mathbf{r}_m^d)$ , and  $g^{rt}(\mathbf{r}_q^r, \mathbf{r}_p^t)$ , respectively, in Eq. (4.2) to Eq. (4.7).

### 4.3 Numerical Experiments

In this section, we present simulation results that illustrate the performance of the formulation of phaseless imaging as convex programs, (4.12) for the noiseless case and (4.14) for noisy case. The convex problem is then solved by the “ $\mathcal{L}1$ -MAGIC” solver [153], which is based on standard interior-point methods, and is suitable for large-scale problems.

We employ a SIMO data acquisition scheme: (1) a single TX antenna ( $N_t = 1$ ) is placed at a position randomly chosen in the annulus-shaped region surrounding the domain of interest; (2) a total number of  $N_r$  RX antennas are placed at random positions also in the annulus; (3) overlap between these antennas should be avoided. For all the three simulation, we use a same annulus-shaped detection region centered at the origin, with its inner and outer radii being  $3\lambda$  and  $6\lambda$  respectively, as illustrated in Fig. 4.1. The scenario considered here is chosen so that it is comparable to the results previously reported in [143, 154].

Noise corruption of the electric field is realized by the following procedure.



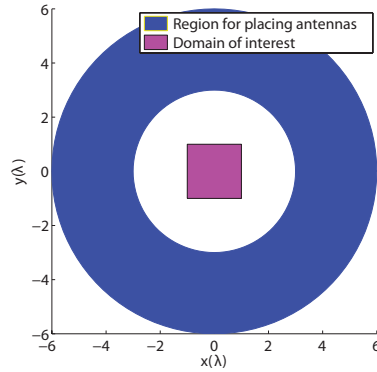


Figure 4.1: Configuration of physical setup

The received field is recorded in the format of the multi-static response (MSR) matrix  $\overline{\overline{K}}$  with size of  $N_r \times N_t$  [105]. White Gaussian noise  $\overline{\overline{\kappa}}$  is thereafter added to the MSR matrix, and the resultant noise-corrupted matrix  $\overline{\overline{K}} + \overline{\overline{\kappa}}$  is treated as the measured MSR matrix which we utilized to reconstruct the scatterers. The noise level is quantified in signal-to-noise ratio ( $SNR$ ) as  $20 \cdot \log \frac{\|\overline{\overline{K}}\|_F}{\|\overline{\overline{\kappa}}\|_F}$ , where  $\|\cdot\|_F$  denotes the Frobenius norm of a matrix [105].

In the first simulation shown in Fig. 4.2(a), we consider two point-like scatterers, with relative permittivities being 1.5 and 1.6 respectively, placed at at  $(0.7\lambda, -0.7\lambda)$  and  $(-0.7\lambda, 0.7\lambda)$  in the domain of interest, which is a  $2.0\lambda$ -by- $2.0\lambda$  square and has been discretized into a grid of  $10 \times 10$  subunits.  $N_r = 20$  RX antennas are placed randomly in the annulus-shaped region. Fig. 4.2(b) shows the retrieved image without the presence of additive noise, where the locations and permittivities of the two small scatterers are exactly recovered. Fig. 4.2(c) and (d) show the images reconstructed from the data corrupted by additive Gaussian white noise with  $SNR = 20dB$  and  $SNR = 10dB$ , respectively. Both of them reflect the exact locations and characteristics of the scatterers, though noticeable blurred parts due to noise corruption are observed and Fig. 4.2(d) is obviously worse than

Fig. 4.2(c), because of higher  $SNR$ .

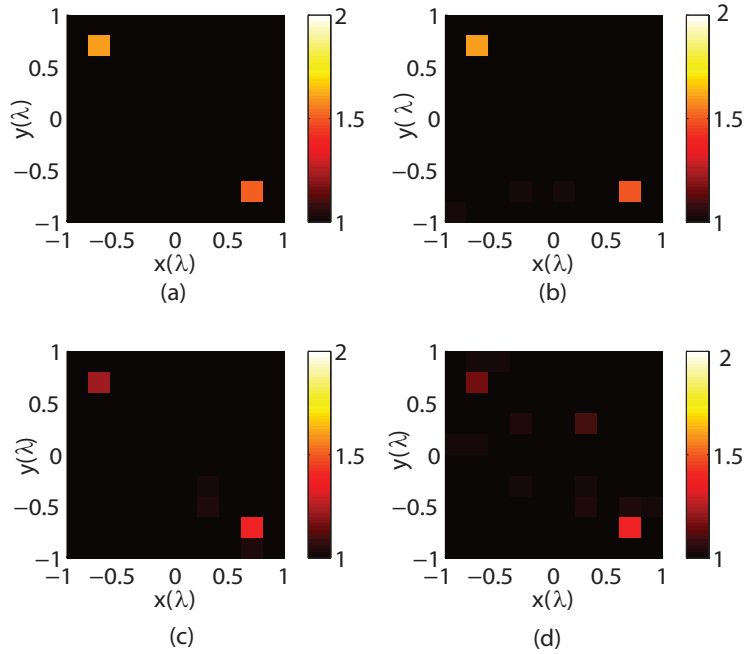


Figure 4.2: The pattern consisting of two point-like objects. (a) Exact pattern of relative permittivity. (b) Reconstructed pattern obtained by solving (4.12) with no noise added into measurement. (c) Reconstructed pattern obtained by solving (4.13) with Gaussian white noise added into measurement ( $SNR=20$  dB). (d) Reconstructed pattern obtained by solving (4.13) with Gaussian white noise added into measurement ( $SNR=10$  dB).

The choice of  $N_r$  is an interesting and meaningful topic in the sense of reducing the measurement cost, and thus has been discussed in the seminal work in [96]. We also investigate this issue within the framework of compressive sensing, by sweeping the value of  $N_r$  from 6 to 22 with step being 2 in the experiment without presence of additive noise. The results are reproduced in Fig. 4.3 and Fig. 4.4. In Fig. 4.4, the error is defined as the norm of the difference between the exact pattern ( $\overline{\varepsilon_r}$ ) and the reconstructed pattern ( $\overline{\varepsilon_r^{\text{rec}}}$ ):

$$err = \|\bar{\varepsilon}_r - \bar{\varepsilon}_r^{\text{rec}}\|,$$

where

$$\bar{\varepsilon}_r = [\varepsilon_r(\mathbf{r}_1^d), \varepsilon_r(\mathbf{r}_2^d), \dots, \varepsilon_r(\mathbf{r}_{N_d}^d)]^T$$

$$\bar{\varepsilon}_r^{\text{rec}} = [\varepsilon_r^{\text{rec}}(\mathbf{r}_1^d), \varepsilon_r^{\text{rec}}(\mathbf{r}_2^d), \dots, \varepsilon_r^{\text{rec}}(\mathbf{r}_{N_d}^d)]^T$$

The results indicate that, in order to guarantee the good performance of compressive sensing,  $N_r$  must be larger than a threshold value (around 18 as shown in Fig. 4.4). According to the theory of compressive sensing [138–141], this threshold value is dependent on the sparsity of the signal. On the other hand, after exceeding the threshold, diminishing benefit can be gained by further increase in the number of RX antennas. This observation is also consistent with the theory of compressive sensing [139–141].

The second test configuration is more complex. As depicted in Fig. 4.5(a), five point-like scatterers are placed at  $(0.85\lambda, -0.55\lambda)$ ,  $(-0.6\lambda, 0.55\lambda)$ ,  $(0.15\lambda, -0.1\lambda)$ ,  $(0.7\lambda, 0.7\lambda)$ ,  $(-0.7\lambda, -0.45\lambda)$ , with their relative permittivities being 1.8, 2.0, 1.6, 1.7, and 1.9, respectively, in a selected domain of interest, which is a square of  $2.0\lambda$  for each side, and has been discretized into a grid of  $12 \times 12$  subunits. As elaborated in [138–141], the minimum number of samples required by compressive sensing increases with the sparsity:  $m \geq C \cdot S \cdot \log(n/S)$ , where  $m$  is number of samples,  $n$  is the dimension of unknown signal,  $S$  is sparsity, and  $C$  is some constant depending on each instance. Therefore, in our problem, although the exact analytic expression of number of measurement depending on number of point-like scatterers is not available, more measurement is required to cope with the increase in the number of nonzero entries (sparsity). Accordingly, we arrange

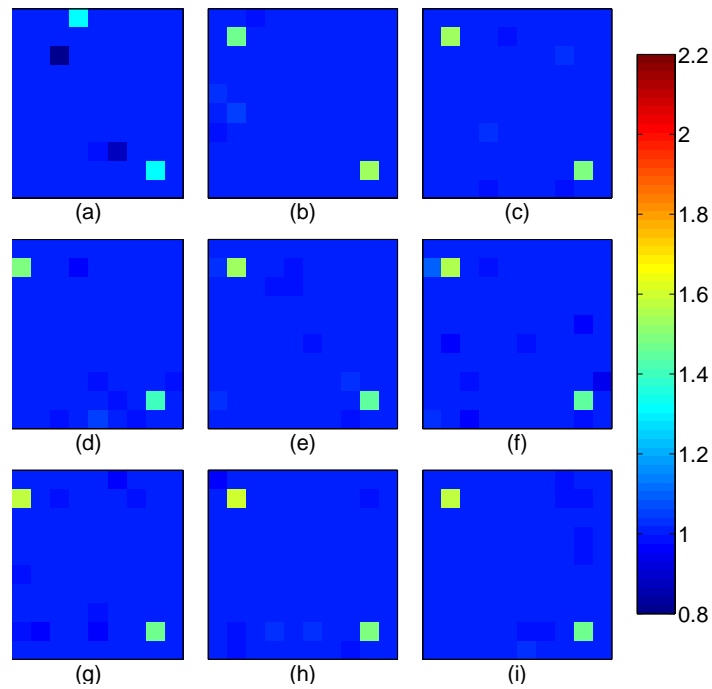


Figure 4.3: Reconstructed patterns in the first experiment without noise for the number of RX antennas being 6, 8, 10, 12, 14, 16, 18, 20, 22 in (a), (b), (c), (d), (e), (f), (g), (i), respectively.

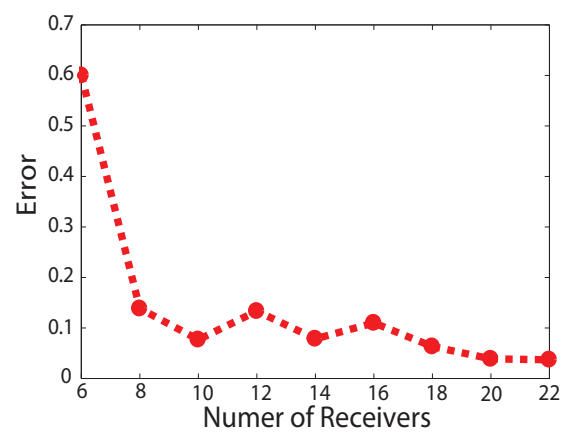


Figure 4.4: The error of reconstructed patterns in the first experiment without noise for varying number of RX antennas.

$N_r = 50$  RX antennas placed randomly in the annulus-shaped region. Fig. 4.5(b) and Fig. 4.5(c) exhibit the retrieved images in the absence and presence of additive noise ( $SNR = 20dB$ ), respectively, where both locations and permittivities of the five small scatterers are exactly recovered. It is also observed that excessive noise corruption prevents our method from reconstructing the exact image, as shown in Fig. 4.5(d), where  $SNR = 10dB$ .

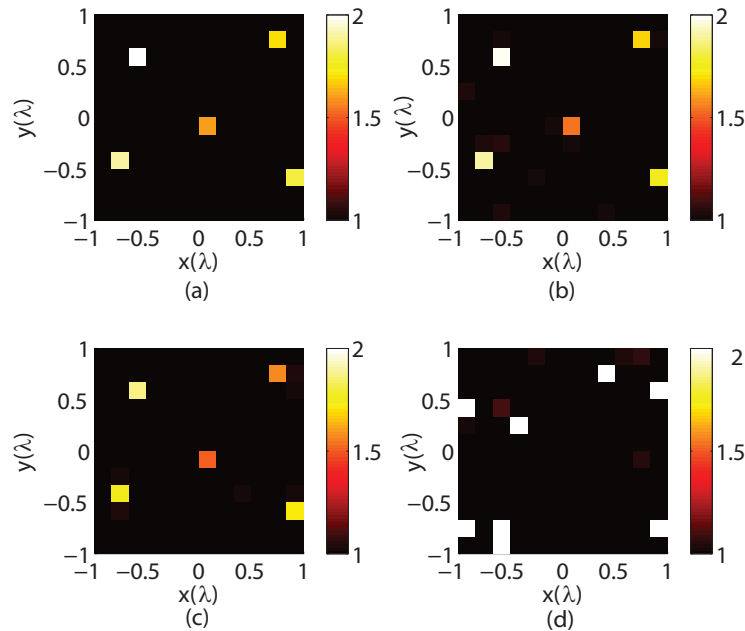


Figure 4.5: The pattern consisting of five point-like objects. (a) Exact pattern of relative permittivity. (b) Reconstructed pattern obtained by solving (4.12) with no noise added into measurement. (c) Reconstructed pattern obtained by solving (4.13) with Gaussian white noise added into measurement ( $SNR=20$  dB). (d) Reconstructed pattern obtained by solving (4.13) with Gaussian white noise added into measurement ( $SNR=10$  dB).

We examine the performance of our approach for heterogeneous background medium in the third numerical experiment, which is similar to the practical crack detection in cylindrical parts. The cylindrical background medium is shown in Fig. 4.6(a) as a circular region with radius being  $2\lambda$  and relative permittivity being

1.1. In the circular object, there are two cracks (point-like scatterers) located at  $(0.7\lambda, -0.7\lambda)$ ,  $(-0.7\lambda, 0.7\lambda)$ , with relative permittivities being 1.8 and 1.9, respectively. The domain of interest is centered at the origin (a square of  $2.0\lambda$  for each side, and has been discretized into a grid of  $10 \times 10$  subunits. We use  $N_r = 30$  RX antennas placed randomly in the annulus-shaped region of detection. For this kind of background medium, the four types of Green's functions have closed-form and is derived by using the Graf's addition theorem [62, 155]. For more complex heterogeneous background medium, the close-form Green's function may not be available, and thus we have to calculate numerically the value of Green's function as done, for instance, in [156]. After solving the optimization problem, the retrieved images in the absence and presence of additive noise ( $SNR = 20dB$ ) are shown in Fig. 4.6(b) and Fig. 4.6(c), respectively, where both locations and permittivities of the two small scatterers are clearly identified.

## 4.4 Conclusion

In this chapter, we present an approach to imaging the locations and characters of sparsely distributed point-like dielectric scatterers by utilizing intensity-only measurement, with or without the corruption of additive Gaussian white noise. Our formulation of phaseless imaging is based on the knowledge of the intensity of total measured electric field, which is more realistic from the standpoint of practical application, compared with the previously published modeling [143]. It is shown that, despite being an intrinsically nonlinear problem, the phaseless imaging problem can be reformulated as a linear system, provided that a proper bases are chosen; and the problem is then solved by minimizing a linear objective

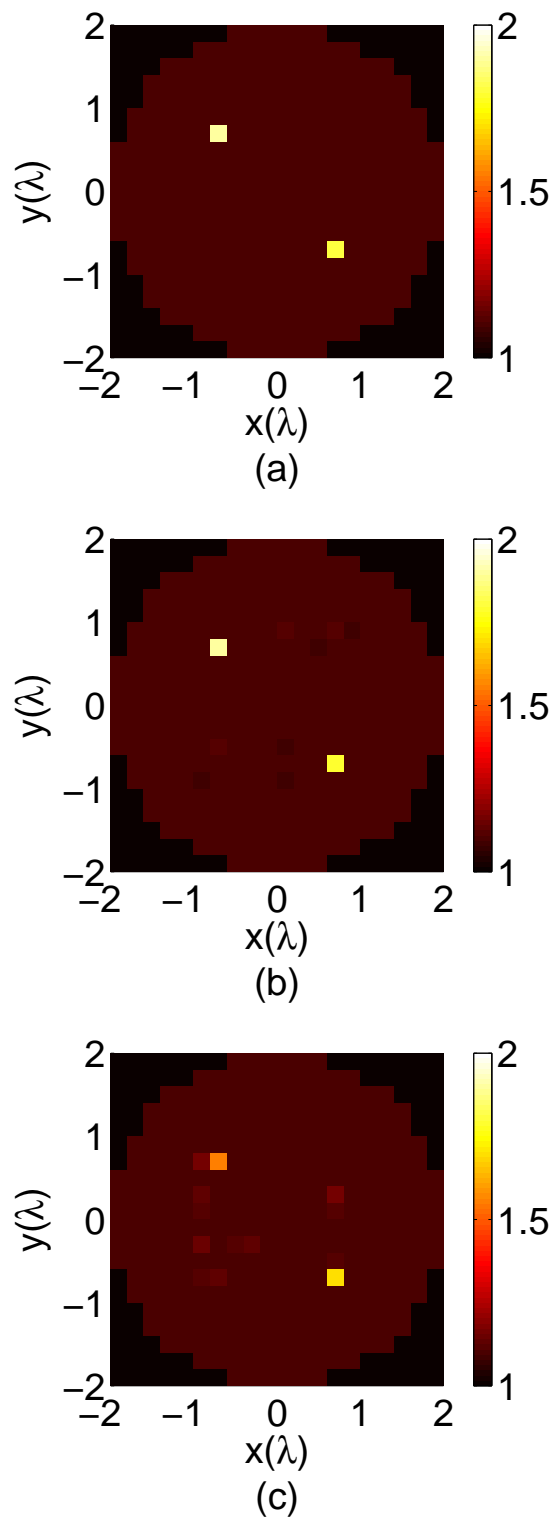


Figure 4.6: The pattern consisting of two point-like objects in a cylindrical heterogeneous background medium. (a) Exact pattern of relative permittivity. (b) Reconstructed pattern obtained by solving (4.12) with no noise added into measurement. (c) Reconstructed pattern obtained by solving (4.13) with Gaussian white noise added into measurement (SNR=20 dB).

functional with constraints in the framework of compressive sensing. We can easily extend the proposed formulation and algorithm to the case of heterogeneous background medium, if the distribution and character of the objects, which form the heterogeneous medium background, are *a priori* knowledge. This extension paves the road of employing the compressive-sensing-based approach to many real-world imaging problems involving heterogeneous background medium. The numerical simulations confirm that this approach is able to provide exact image of the domain of interest with efficiency and robustness against noise. It is note-worthy that our method is limited by the Born approximation, so the reconstruction scheme should be redesigned under circumstances where the Born approximation does not hold. Extension of our method to the general situation without Born approximation, together with the mathematical and theoretical justification of the robustness of our method, form our ongoing research effort.



## CHAPTER 5

# Future Work

---

*“Now this is not the end. It is not even the beginning of the end. But it is, perhaps, the end of the beginning.”*

*–Winston Churchill*

Investigation for better formulation and more efficient algorithms of the inverse scattering problems is always of our interest, and we will definitely proceed with our best endeavor in this aspect. On the other hand, we should never neglect the significance of other works which also deserve our attention for the sake of real-world application of our inversion algorithm.

The practical applicability of the inverse scattering methods proposed in this thesis is limited partly due to its expensive computational cost. This limitation manifests itself especially when we have to perform large-scale and real-time inverse scattering with intensity-only measurements. Fortunately, the way of accelerating the computationally intensive inverse scattering algorithms is paved by the recent progress in high performance computing (HPC) technologies based on various hardware platforms, for instance, the message passing interface (MPI) for distributed memory system, and open multi-processing (OpenMP) for the shared memory system, open computing language (OpenCL) or compute unified

device architecture (CUDA) for graphics processing unit (GPU) programming, and field-programmable gate array (FPGA) high performance computing. These technologies have prove efficient way of enhancing the efficiency of intensive scientific computation for a wide range of practical applications. Generally speaking, we will have to parallize our inverse scattering algorithm and take full advantage of the advanced parallel programming platform. The possible specific future work in this regard may include selecting the proper parallel programming platform based on the balance between performance and expense, transforming the serial algorithm to its parallel counterpart, and testing and tuning algorithm so as to optimize computational efficiency.

Another crucial future work is about the practical experiment of inverse scattering. From the viewpoint of application, this necessary work is still far from satisfactory, and is therefore partially responsible for the inverse scattering remaining as a scientific research in laboratory rather than as a mature and reliable technology in industry. Even in the inverse scattering research community, researchers often have to face the lack of real experiment database for specific scenario of interest. Encouragingly, in the recent two decades, a few database of inverse scattering experiment have been produced and opened to the inverse problems community. The Ipswich database [157–159] and the Fresnel database [160, 161] published the the far-field scattered data measured with a bi-static, mechanically scanned system, which is followed by the EIGOR database [162] providing the near-field multi-static data. These progress, however, have not completely addressed the insufficient coupling between inverse scattering theory and experiments, in the sense of real-world application. This demands our future

work regarding the inverse scattering experiment. The specific topic may focus on the compensation of drift error, the design of the measurement antennas, the calibration of the coupling among antennas, the problem of noise corruption, etc.

These constitute our future research plan.



# Bibliography

- [1] J. Keller, “Inverse problems,” *Am. Math. Mon.*, vol. 83, pp. 107 – 118, 1976.  
1
- [2] C. W. Liao, M. A. Fiddy, and C. L. Byrne, “Imaging from the zero locations of far-field-intensity data,” *J. Opt. Soc. Am. A*, vol. 14, pp. 3155 – 61, 1997.  
3, 12, 83
- [3] A. Litman and K. Belkebir, “Two-dimensional inverse profiling problem using phaseless data,” *J. Opt. Soc. Am. A*, vol. 23, pp. 2737 – 46, 2006.  
12, 83
- [4] T. Takenaka, Z. Q. Meng, T. Tanaka, and W. C. Chew, “Local shape function combined with genetic algorithm applied to inverse scattering for strips,” *Microw. Opt. Tech. Lett.*, vol. 16, pp. 337–341, 1997. 3, 8
- [5] A. Kirsch, *An introduction to the mathematical theory of inverse problem*. New York: Springer, 1996. 5, 26, 69
- [6] D. Colton and R. Kress, *Inverse Acoustic and Electromagnetic Scattering Theory*, 2nd ed. Berlin, Germany: Springer-Verlag, 1998. 5, 48, 59
- [7] A. Kirsch, “The MUSIC-algorithm and the factorization method in inverse scattering theory for inhomogeneous media,” *Inverse Probl.*, vol. 18, pp. 1025–1040, 2002. 7
- [8] Y. M. Wang and W. C. Chew, “An iterative solution of two-dimensional

- electromagnetic inverse scattering problem,” *Int. J. Imaging Syst. Technol.*, vol. 1, p. 100108, 1989.
- [9] W. C. Chew and Y. M. Wang, “Reconstruction of two-dimensional permittivity distribution using the distorted born iterative method,” *IEEE Trans. Med. Imag.*, vol. 9, p. 218225, 1990 6
- [10] M. Moghaddam, W. C. Chew, and M. Oristaglio, “Comparison of the born iterative method and tarantola’s method for an electromagnetic time-domain inverse problem,” *Int. J. Imaging Syst. Technol.*, vol. 3, pp. 318 – 333, 1991.
- [11] M. Vauhkonen, D. Vadasz, P. A. Karjalainen, E. Somersalo, and J. P. Kaipio, “Tikhonov regularization and prior information in electrical impedance tomography,” *IEEE Trans. Med. Imag.*, vol. 17, no. 2, pp. 285 – 293, 1998. 5
- [12] A. Abubakar, P. M. van den Berg, and J. J. Mallorqui, “Imaging of biomedical data using a multiplicative regularized contrast source inversion method,” *IEEE Trans. Microw. Theory Tech.*, vol. 50, pp. 1761–1771, 2002. 5, 94
- [13] A. Abubaker and P. V. D. Berg, “Total variation as a multiplicative constraint for solving inverse problems,” *IEEE Trans. Image Process.*, vol. 10, no. 9, pp. 1384 – 1392, 2001.
- [14] P. M. van den Berg, A. L. van Broekhoven, and A. Abubakar, “Extended contrast source inversion,” *Inverse Probl.*, vol. 15, pp. 1325–1344, 1999. 5, 7, 94

- [15] S. Caorsi and G. L. Gragnani, "Inverse-scattering method for dielectric objects based on the reconstruction of the nonmeasurable equivalent current density," *Radio Sci.*, vol. 34, pp. 1 – 8, 1999. 5, 89
- [16] H. Abdullah and A. K. Louis, "The approximate inverse for solving an inverse scattering problem for acoustic waves in inhomogeneous medium," *Inverse Probl.*, vol. 15, pp. 1213 – 1229, 1999.
- [17] A. Lakhali and A. K. Louis, "Locating radiating sources for Maxwell's equations using the approximate inverse," *Inverse Probl.*, vol. 24, p. 045020, 2008. 5
- [18] W. C. Chew, *Waves and Fields in Inhomogeneous Media*, ser. Electromagnetic Waves, D. G. Dudley, Ed. IEEE Press, 1995. 5, 6, 15, 107
- [19] W. A. Kalender, "X-ray computed tomography," *Phys. Med. Biol.*, vol. 51, pp. R29–R43, 2006. 6
- [20] J. B. Keller, "Accuracy and validity of the Born and Rytov approximations," *J. Opt. Soc. Am. A*, vol. 59, no. 8, pp. 1003–1004, 1969. 6
- [21] M. Moghaddam and W. C. Chew, "Study of some practical issues in inversion with the Born iterative method using time-domain data," *Academic Press*, vol. 41, no. 2, pp. 177 – 184, 1993. 6
- [22] F. Li, Q. H. Liu, and L. Song, "Three-dimensional reconstruction of objects buried in layered media using Born and distorted Born iterative methods," *IEEE Trans. Geosci. Remote Sens.*, vol. 1, no. 2, pp. 107 – 111, 2004. 6

- [23] W. C. Chew and Y. M. Wang, "Reconstruction of two-dimensional permittivity distribution using the distorted born iterative method," *IEEE Trans. Med. Imag.*, vol. 9, pp. 218 – 225, 1990. 6
- [24] R. Lavarello and M. Oelze, "A study on the reconstruction of moderate contrast targets using the distorted born iterative method," *IEEE Trans. Ultrason., Ferroelectr., Freq. Control*, vol. 55, pp. 112 – 124, 2008. 6
- [25] R. E. Kleinman and P. M. van den Berg, "A modified gradient method for two-dimensional problems in tomography," *J. Computat. Appl. Math.*, vol. 42, pp. 17 – 35, 1992. 7
- [26] P. M. van den Berg and R. E. Kleinman, "A contrast source inversion method," *Inverse Probl.*, vol. 13, pp. 1607–1620, 1997. 7, 94
- [27] A. Abubakar and P. M. van den Berg, "The contrast source inversion method for location and shape reconstructions," *Inverse Probl.*, vol. 18, pp. 495–510, 2002.
- [28] A. Abubakar, T. M. Habashy, P. M. van den Berg, and D. Gisolf, "The diagonalized contrast source approach: an inversion method beyond the born approximation," *Inverse Probl.*, vol. 21, pp. 685–702, 2005. 7, 94
- [29] X. Chen, "Application of signal-subspace and optimization methods in reconstructing extended scatterers," *J. Opt. Soc. Am. A*, vol. 26, pp. 1022–1026, 2009. 7, 14, 39, 46, 47, 48, 49, 58, 59, 60, 64, 68, 69, 84, 89, 90, 91, 93
- [30] Y. Zhong and X. Chen, "MUSIC imaging and electromagnetic inverse



- scattering of multiply scattering small anisotropic spheres,” *IEEE Trans. Antennas Propag.*, vol. 55, pp. 3542–3549, 2007. 7, 11, 48, 59, 68, 92
- [31] X. Chen and K. Agarwal, “MUSIC algorithm for two-dimensional inverse problems with special characteristics of cylinders,” *IEEE Trans. Antennas Propag.*, vol. 56, pp. 1808–1812, 2008. 7, 10
- [32] X. Chen and Y. Zhong, “A robust noniterative method for obtaining scattering strengths of multiply scattering point targets,” *J. Acoust. Soc. Am.*, vol. 122, pp. 1325–1327, 2007. 7, 11
- [33] K. Agarwal and X. Chen, “Applicability of MUSIC-type imaging in two-dimensional electromagnetic inverse problems,” *IEEE Trans. Antennas Propag.*, vol. 56, pp. 3217–3223, 2008. 7, 10
- [34] Y. Zhou, J. Li, and H. Ling, “Shape inversion of metallic cavities using hybrid genetic algorithm combined with tabu list,” *Electron. Lett.*, vol. 39, no. 3, pp. 280 – 281, 2003. 8
- [35] Z. Q. Meng, T. Takenaka, and T. Tanaka, “Image reconstruction of two-dimensional impenetrable objects using genetic algorithm,” *J. Electromagn. Waves Appl.*, vol. 13, pp. 95 – 118, 1999.
- [36] C. C. Chiu, T. C. Tu, T. A. Wysocki, B. J. Wysock, and H. C. Lu, “Cubic-spline expansion for electromagnetic imaging of buried multiple conductors,” *Electromagnetics*, vol. 29, pp. 321 – 336, 2009.
- [37] C. C. Chiu and W. T. Chen, “Electromagnetic imaging for an imperfectly

- conducting cylinder by the genetic algorithm,” *IEEE Trans. Microw. Theory Tech.*, vol. 48, pp. 1901–1905, 2000. 8
- [38] R. Storn and K. Price, “Differential evolution - a simple and efficient heuristic for global optimization over continuous spaces,” *J. Global Optim.*, vol. 11, pp. 341–359, 1997. 8
- [39] R. Storn, “System design by constraint adaptation and differential evolution,” *IEEE Trans. Evol. Comput.*, vol. 3, no. 1, pp. 22–34, Apr. 1999.
- [40] X. Chen, K. O’Neill, B. E. Barrowes, T. M. Grzegorzcyk, and J. A. Kong, “Application of a spheroidal-mode approach and a differential evolution algorithm for inversion of magneto-quasistatic data in UXO discrimination,” *Inverse Probl.*, vol. 20, pp. S27–40, 2004.
- [41] I. T. Rekanos, “Shape reconstruction of a perfectly conducting scatterer using differential evolution and particle swarm optimization,” *IEEE Trans. Geosci. Remote Sens.*, vol. 46, pp. 1967–1974, 2008. 8
- [42] B. Mhamdi, K. Grayaa, and T. Aguilu, “Microwave imaging for conducting scatterers by hybrid particle swarm optimization with simulated annealing,” in *2011 8th International Multi-Conference on Systems, Signals and Devices (SSD)*, Anchorage, AK, USA, pp. 1 – 6. 8
- [43] M. Saillard, P. Vincent, and G. Micolau, “Reconstruction of buried objects surrounded by small inhomogeneities,” *Inverse Probl.*, vol. 16, pp. 1195 – 1208, 2000. 8
- [44] J. H. Lin and W. C. Chew, “Solution of the three-dimensional

- electromagnetic inverse problem by the local shape function and the conjugate gradient fast fourier transform methods,” *J. Opt. Soc. Am. A*, vol. 14, pp. 3037 – 3045, 1997.
- [45] ———, “Ultrasonic imaging by local shape function method with cgfft,” *IEEE Transactions on Ultrasonics Ferroelectrics and Frequency Control*, vol. 43, pp. 956–969, 1996. 8
- [46] A. Litman, D. Lesselier, and F. Santosa, “Reconstruction of a two-dimensional binary obstacle by controlled evolution of a level-set,” *Inverse Probl.*, vol. 14, pp. 685–706, 1998. 8
- [47] L. Poli and P. Rocca, “Exploitation of TE-TM scattering data for microwave imaging through the multi-scaling reconstruction strategy,” *Prog. Electromagn. Res.*, vol. 99, pp. 245 – 260, 2009. 8, 85
- [48] P. Rocca, M. Donelli, G. L. Gragnani, and A. Massa, “Iterative multi-resolution retrieval of non-measurable equivalent currents for the imaging of dielectric objects,” *Inverse Probl.*, vol. 25, p. 055004, 2009. 8, 89
- [49] E. Bermani, A. Boni, S. Caorsi, and A. Massa, “An innovative real-time technique for buried object detection,” *IEEE Trans. Geosci. Remote Sens.*, vol. 41, no. 4, pp. 927 – 931, 2003. 8
- [50] S. Caorsi, D. Anguita, E. Bermani, A. Boni, M. Donelli, and A. Massa, “A comparative study of NN and SVM-based electromagnetic inverse scattering approaches to on-line detection of buried objects,” *J. APPL.*

- COMPUT. ELECTROM.*, *Special Issue on Neural Network Applications in Electromagnetic*, vol. 18, no. 2, pp. 1 – 11, 2003.
- [51] E. Bermani, A. Boni, S. Caorsi, M. Donelli, and A. Massa, “A multi-source strategy based on a learning-by-examples technique for buried object detection,” in *Progress in Electromagnetic Research Symposium*. 8
- [52] A. Lakhtakia, “Polarizability dyadics of small bianisotropic spheres,” *J. Phys. France*, vol. 51, pp. 2235 – 2242, 1990. 9
- [53] G. Micolau, M. Saillard, and P. Borderies, “DORT method as applied to ultrawideband signals for detection of buried objects,” *IEEE Trans. Geosci. Remote Sens.*, vol. 41, no. 8, pp. 1813–1820, Aug. 2003. 9
- [54] C. Prada and J. Thomas, “Experimental subwavelength localization of scatterers by decomposition of the time reversal operator interpreted as a covariance matrix,” *J. Acoust. Soc. Am.*, vol. 114, no. 1, pp. 235–43, 2003.
- [55] H. Tortel, G. Micolar, and M. Saillard, “Decomposition of the time reversal operator for electromagnetic scattering,” *J. Electromagn. Waves Appl.*, vol. 13, pp. 687–719, 1999.
- [56] G. Lerosey, J. de Rosny, A. Tourin, A. Derode, G. Montaldo, and M. Fink, “Time reversal of electromagnetic waves,” *Phys. Rev. Lett.*, vol. 92, p. 193904, 2004.
- [57] M. Fink, “Time reversal of ultrasonic fields—part 1: Basic principles,” *IEEE Trans. Ultrason. Ferroelect. Freq. Contr.*, vol. 39, pp. 555–566, 1992.

- [58] D. H. Chambers and J. G. Berryman, "Analysis of the time-reversal operator for a small spherical scatterer in an electromagnetic field," *IEEE Trans. Antennas Propag.*, vol. 52, pp. 1729–1738, 2004.
- [59] G. Lerosey, J. de Rosny, A. Tourin, A. Derode, and M. Fink, "Time reversal of wideband microwaves," *Appl. Phys. Lett.*, vol. 88, p. 154101, 2006.
- [60] A. J. Devaney, "Time reversal imaging of obscured targets from multistatic data," *IEEE Trans. Antennas Propag.*, vol. 53, no. 5, pp. 1600–1610, May 2005.
- [61] D. Liu, G. Kang, L. Li, Y. Chen, S. Vasudevan, W. Joines, Q. H. Liu, J. Krolik, and L. Carin, "Electromagnetic time-reversal imaging of a target in a cluttered environment," *IEEE Trans. Antennas Propag.*, vol. 53, no. 9, pp. 3058–3066, Sep. 2005.
- [62] T. Rao and X. Chen, "Analysis of the time-reversal operator for a single cylinder under two-dimensional settings," *J. Electromagn. Waves Appl.*, vol. 20, no. 15, pp. 2153–2165, 2006. [120](#)
- [63] X. Chen, "Time-reversal operator for a small sphere in electromagnetic fields," *J. Electromagn. Waves Appl.*, vol. 21, no. 15, pp. 1219–30, 2007.
- [64] D. H. Chambers and J. G. Berryman, "Target characterization using decomposition of the time-reversal operator: electromagnetic scattering from small ellipsoids," *Inverse Probl.*, vol. 22, pp. 2145–2163, 2006.
- [65] A. Derode, A. Tourin, and M. Fink, "Time reversal in multiply scattering media," *Ultrasonics*, vol. 36, pp. 443–447, 1998.

- [66] —, “Limits of time-reversal focusing through multiple scattering: Long-range correlation,” *J. Acoust. Soc. Am.*, vol. 107, pp. 2987–2998, 2000.
- [67] P. Roux, A. Derode, A. Peyre, A. Tourin, and M. Fink, “Acoustical imaging through a multiple scattering medium using a time-reversal mirror,” *J. Acoust. Soc. Am.*, vol. 107, pp. L7–L12, 2000. 9
- [68] R. Sicard, A. Chahbaz, and J. Goyette, “Guided lamb waves and L-SAFT processing technique for enhanced detection and imaging of corrosion defects in plates with small depth-to-wavelength ratio,” *IEEE Trans. Ultrason., Ferroelectr., Freq. Control*, vol. 51, no. 10, pp. 1287 – 1297, 2004. 10
- [69] Z. Shao, L. Shi, Z. Shao, and J. Cai, “Design and application of a small size SAFT imaging system for concrete structure,” *Review of Scientific Instruments*, vol. 82, no. 7, pp. 073708, 2011. 10
- [70] K. W. K. Lui and H. C. So, “Modified pisarenko harmonic decomposition for single-tone frequency estimation,” *IEEE Trans. Signal Process.*, vol. 56, no. 7, pp. 3351 – 3356, 2008. 10
- [71] S. K. Lehman and A. J. Devaney, “Transmission mode time-reversal super-resolution imaging,” *J. Acoust. Soc. Am.*, vol. 113, pp. 2742 – 2753, 2003. 10
- [72] F. K. Gruber, E. A. Marengo, and A. J. Devaney, “Time-reversal imaging

- with multiple signal classification considering multiple scattering between the targets,” *J. Acoust. Soc. Am.*, vol. 115, pp. 3042–3047, 2004. 10
- [73] A. J. Devaney, E. A. Marengo, and F. K. Gruber, “Time-reversal-based imaging and inverse scattering of multiply scattering point targets,” *J. Acoust. Soc. Am.*, vol. 118, pp. 3129–3138, 2005. 10
- [74] H. Ammari, E. Iakovleva, and H. Kang, “Reconstruction of a small inclusion in a two-dimensional open waveguide,” *SIAM J. Appl. Math.*, vol. 65, pp. 2107–2127, 2005.
- [75] H. Ammari, E. Iakovleva, D. Lesselier, and G. Perruson, “MUSIC-type electromagnetic imaging of a collection of small three-dimensional bounded inclusions,” *SIAM J. Sci. Comput.*, vol. 29, no. 2, pp. 674–709, 2007.
- [76] E. Iakovleva, S. Gdoura, D. Lesselier, and G. Perrusson, “Multistatic response matrix of a 3-D inclusion in half space and MUSIC imaging,” *IEEE Trans. Antennas Propag.*, vol. 55, pp. 2598 – 2609, 2007.
- [77] X. Chen and K. Agarwal, “MUSIC algorithm for two-dimensional inverse problems with special characteristics of cylinders,” *IEEE Trans. Antennas Propag.*, vol. 56, pp. 1808–1812, 2008.
- [78] H. Ammari, E. Iakovleva, and D. Lesselier, “A MUSIC algorithm for locating small inclusions buried in a half-space from the scattering amplitude at a fixed frequency,” *SIAM Mult. Model. and Simu.*, vol. 3, pp. 597–628, 2005.
- [79] X. Chen and Y. Zhong, “MUSIC electromagnetic imaging with enhanced

- resolution for small inclusions,” *Inverse Probl.*, vol. 25, p. ID:015008, 2009. 10
- [80] E. A. Marengo and F. K. Gruber, “Noniterative analytical formula for inverse scattering of multiply scattering point targets,” *J. Acoust. Soc. Am.*, vol. 120, pp. 3782–3788, 2006. 11
- [81] A. C. Fannjiang, “Compressive imaging of subwavelength structures,” *SIAM J. Imag. Sci.*, vol. 2, no. 4, pp. 1277 – 1291, 2009. 11, 104
- [82] —, “Compressive inverse scattering I. high-frequency SIMO/MISO and MIMO measurements,” *Inverse Probl.*, vol. 26, 2010. 111
- [83] —, “Compressive inverse scattering II. multi-shot SISO measurements with born scatterers,” *Inverse Probl.*, vol. 26, 2010. 11, 104, 111
- [84] G. Oliveri, P. Rocca, and A. Massa, “A bayesian-compressive-sampling-based inversion for imaging sparse scatterers,” *IEEE Trans. Geosci. Remote Sens.*, vol. 49, pp. 3993 – 4006, 2011. 11, 104
- [85] G. O. et al., “Model-based inversion algorithms based on bayesian compression sensing,” in *Proc. 2011 IEEE AP-S International Symposium*, Spokane, Washington, USA, July 2011, pp. 492–495. 104
- [86] E. Marengo, “Subspace and bayesian compressive sensing methods in imaging,” in *Progress in Electromagnetics Research Symposium (PIERS) 2008*, Cambridge, Massachusetts, USA, July 2008. 11, 104



- [87] V. Rokhlin, “Rapid solution of integral equations of scattering theory in two dimensions,” *J. Comput. Phys.*, vol. 86, pp. 414 – 439, 1990. [12](#)
- [88] C. C. Lu and W. C. Chew, “A multilevel algorithm for solving boundary-value scattering,” *Micro. Opt. Tech. Lett.*, vol. 7, no. 10, pp. 466 – 470, 1994. [12](#)
- [89] J. M. Song, C. C. Lu, and W. C. Chew, “Multilevel fast multiple algorithm for electromagnetic scattering by large complex objects,” *IEEE Trans. Antennas Propag.*, vol. 45, no. 10, pp. 1488 – 1493, 1997. [12](#)
- [90] W. C. Chew, J. M. Jin, E. Michielssen, and J. Song, Eds., *Fast and Efficient Algorithms in Computational Electromagnetics*, ser. Electromagnetic Waves. Artech House, Inc., 2001. [12](#)
- [91] A. J. Hesford and W. C. Chew, “Fast inverse scattering solutions using the distorted born iterative method and the multilevel fast multipole algorithm,” *J. Acoust. Soc. Am.*, vol. 128, no. 2, pp. 679 – 690, 2010. [12](#)
- [92] P. Zwamborn and P. M. van den Berg, “The three-dimensional weak form of the conjugate gradient FFT method for solving scattering problems,” *IEEE Trans. Microw. Theory Tech.*, vol. 9, no. 40, pp. 1757 – 1766, 1992. [12](#)
- [93] H. Gan and W. C. Chew, “Fast computation of 3d inhomogeneous scattered field using a discrete BCG-FFT algorithm,” in *Antennas and Propagation Society International Symposium, 1995. AP-S. Digest*, Newport Beach, CA, USA, pp. 1532 – 1535. [12](#)
- [94] T. Takenaka, D. J. N. Wall, H. Harada, and M. Tanaka, “Reconstruction

- algorithm of the refractive index of a cylindrical object from the intensity measurements of the total field,” *Microw. Opt. Technol. Lett.*, vol. 14, pp. 182 – 8, 1997. [12](#), [83](#)
- [95] O. M. Bucci and G. Franceschetti, “On the spatial bandwidth of scattered fields,” *IEEE Trans. Antennas Propag.*, vol. 35, no. 12, pp. 1445 – 1455, 1987. [13](#)
- [96] ———, “On the degrees of freedom of scattered fields,” *IEEE Trans. Antennas Propag.*, vol. 37, pp. 918–926, 1989. [13](#), [60](#), [68](#), [116](#)
- [97] L. Crocco, M. D’Urso, and T. Isernia, “Inverse scattering from phaseless measurement of the total field on a closed curve,” *J. Opt. Soc. Am. A*, vol. 21, pp. 622 – 631, 2004. [13](#), [83](#)
- [98] O. Bucci, L. Crocco, M. D’Urso, and T. Isernia, “Inverse scattering from phaseless measurements of the total field on open lines,” *J. Opt. Soc. Am. A*, vol. 23, pp. 2566 – 2577, 2006. [13](#)
- [99] M. D’Urso, K. Belkebir, L. Crocco, A. Litman, and T. Isernia, “Phaseless imaging with experimental data: facts and challenges,” *J. Opt. Soc. Am. A*, vol. 25, pp. 271 – 281, 2008. [13](#), [83](#)
- [100] A. Devaney, “Diffraction tomographic reconstruction from intensity data,” *IEEE Trans. Image Process.*, vol. 1, no. 2, pp. 221 – 228, 1992. [14](#)
- [101] L. Li, W. Zhang, and F. Li, “Tomographic reconstruction using the distorted Rytov iterative method with phaseless data,” *IEEE Geosci. Remote Sens. Lett.*, vol. 5, no. 3, pp. 479 – 483, 2008. [14](#), [83](#)

- 
- [102] W. Zhang, L. Li, and F. Li, "Multi-frequency imaging from intensity-only data using the phaseless data distorted Rytov iterative method," *IEEE Trans. Antennas Propag.*, vol. 57, pp. 290 – 295, 2009. 14
- [103] L. Li, H. Zheng, and F. Li, "Two-dimensional contrast source inversion method with phaseless data: TM case," *IEEE Trans. Geosci. Remote Sens.*, vol. 47, no. 6, pp. 1719 – 1736, 2009. 14, 84, 94
- [104] H. Zheng, L. Li, and F. Li, "A multi-frequency MRCSI algorithm with phaseless data," *Inverse Probl.*, vol. 25, no. 6, pp. 112 – 124, 2009. 14, 83
- [105] L. Pan, K. Agarwal, Y. Zhong, S. P. Yeo, and X. Chen, "Subspace-based optimization method for reconstructing extended scatterers: Transverse electric case," *J. Opt. Soc. Am. A*, vol. 26, pp. 1932 – 1937, 2009. 14, 48, 62, 64, 68, 69, 84, 87, 88, 93, 96, 115
- [106] L. Pan, X. Chen, and S. P. Yeo, "Application of the subspace-based optimization method in the framework of the method of moments: Transverse electric case," in *Asia-Pacific Microwave Conference*, Singapore, Dec. 2009.
- [107] Y. Zhong and X. Chen, "Twofold subspace-based optimization method for solving inverse scattering problems," *Inverse Probl.*, vol. 25, no. 085003, 2009. 14, 80, 84
- [108] L. Pan, Y. Zhong, X. Chen, and S. P. Yeo, "Subspace-based optimization

- method for inverse scattering problems utilizing phaseless data,” *IEEE Trans. Geosci. Remote Sens.*, vol. 49, pp. 981 – 987, 2011. 14
- [109] L. Pan, X. Chen, and S. P. Yeo, “Compressive phaseless imaging: Utilizing the intensity-only measurement to reconstruct images for point-like perfect dielectric objects with born approximation within the framework of compressed sensing,” *Opt. Express*, pp. –, 2011. 14
- [110] R. F. Harrington, *Time Harmonic Electromagnetic Fields*. New York: McGraw-Hill, 1961. 15
- [111] J. D. Jackson, *Classical Electrodynamics*, 3rd ed. New York: Wiley, 1998. 15
- [112] J. A. Kong, *Electromagnetic Wave Theory*. Cambridge, MA: EMW, 2000. 44, 107
- [113] A. F. Peterson, S. L. Ray, and R. Mittra, *Computational Methods for Electromagnetics*. Oxford: Oxford University Press, 1998. 27, 45, 48, 52, 56, 92
- [114] A. Lakhtakia, “Strong and weak forms of the method of moments and the coupled dipole method for scattering of time-harmonic electromagnetics fields,” *Int. J. Mod. Phys. C*, vol. 3, pp. 583–603, 1992. 28, 29, 44
- [115] A. Yaghjian, “Electric dyadic green’s functions in the source region,” *Proc. IEEE*, vol. 68, no. 2, pp. 248 – 263, 1980. xiii, 29, 30, 31
- [116] R. Fischer, *Precoding and Signal Shaping for Digital Transmission*. Wiley-Interscience, 2002. 34

- [117] R. Remmert, *Theory of Complex Functions*. Springer-Verlag, 1991.
- [118] Z. Nehari, *Introduction to Complex Analysis*. Allyn Bacon, Inc, 1961. 15, 34
- [119] H. T. Hui, “Alternative expression of the electric field in the source region without the source dayadic term,” *J. Electromagn. Waves Appl.*, vol. 18, no. 11, pp. 1523 – 1531, 2004. 29
- [120] X. Chen, “Subspace-based optimization method for solving inverse scattering problems,” *IEEE Trans. Geosci. Remote Sens.*, vol. 48, pp. 42 – 49, 2010. 40, 64, 65, 66, 79, 89, 94, 96
- [121] K. Belkebir, P. C. Chaumet, and A. Sentenac, “Superresolution in total internal reflection tomography,” *J. Opt. Soc. Am. A*, vol. 22, pp. 1889–1897, 2005. 44
- [122] L. Tsang, J. A. Kong, K. H. Ding, and C. O. Ao, *Scattering of Electromagnetic Waves: Numerical Simulations*. Wiley-Interscience, 2000. 44
- [123] O. M. Bucci, L. Crocco, and T. Isernia, “Improving the reconstruction capabilities in inverse scattering problems by exploitation of close-proximity setups,” *J. Opt. Soc. Am. A*, vol. 16, pp. 1788–1798, 1999. 60, 68
- [124] X. Chen, “Subspace-based optimization method in electric impedance tomography,” *J. Electromagn. Waves Appl.*, vol. 23, pp. 1397 – 406, 2009. 64

- 
- [125] L. Pan, X. Chen, and S. P. Yeo, “Nondestructive evaluation of nano-scale structures: inverse scattering approach,” *Applied Physics, A*, vol. 101, pp. 143 – 146, 2010.
- [126] K. Agarwal, L. Pan, and X. Chen, “Subspace-based optimization method for reconstruction of two-dimensional complex anisotropic dielectric objects,” *IEEE Trans. Microw. Theory Tech.*, vol. 58, pp. 1065 – 74, 2010. 64, 68, 89
- [127] J. Nocedal and S. Wright, *Numerical Optimization*, 2nd ed., 2006. 66
- [128] R. Pierri and A. Tamburrino, “On the local minima problem in conductivity imaging via a quadratic approach,” *Inverse Probl.*, vol. 13, no. 6, pp. 1547 – 68, 1997. 68
- [129] X. Chen, “MUSIC imaging applied to total internal reflection tomography,” *J. Opt. Soc. Am. A*, vol. 25, pp. 357–364, 2008. 68, 69, 89, 90, 107
- [130] Y. Zhong and X. Chen, “An FFT twofold subspace-based optimization method for solving electromagnetic inverse scattering problem,” *IEEE Trans. Antennas Propag.*, vol. 59, pp. 914 – 927, 2011. 80
- [131] A. A. Govyadinov, G. Y. Panasyuk, and J. C. Schotland, “Phaseless three-dimensional optical nanoimaging,” *Phys. Rev. Lett.*, vol. 103, no. 213901, pp. 112 – 124, 2009. 83
- [132] M. R. Hajihashemi and M. El-Shenawee, “Te versus tm for the shape reconstruction of 2-d pec targets using the level-set algorithm,” *IEEE Trans. Geosci. Remote Sens.*, vol. 48, no. 3, pp. 1159 – 1168, 2010. 85

- [133] M. J. Akhtar and A. S. Omar, "An analytical approach for the inverse scattering solution of radially inhomogeneous spherical bodies using higher order te and tm illuminations," *IEEE Trans. Geosci. Remote Sens.*, vol. 42, no. 7, pp. 1450 – 1455, 2004.
- [134] I. T. Rekanos, T. V. Yioultsis, and C. S. Hilar, "An inverse scattering approach based on the differential e-formulation," *IEEE Trans. Geosci. Remote Sens.*, vol. 42, no. 7, pp. 1456 – 1461, 2004.
- [135] C. P. Chou and Y. W. Kiang, "Inverse scattering of dielectric cylinders by a cascaded te-tm method," *IEEE Trans. Microw. Theory Tech.*, vol. 47, no. 10, pp. 1923 – 1930, 1999. 85
- [136] D. Franceschini, M. Donell, G. Franceschini, and A. Massa, "Iterative image reconstruction of two-dimensional scatterers illuminated by te waves," *IEEE Trans. Microw. Theory Tech.*, vol. 54, no. 4, pp. 1484 – 1494, 2006. 85
- [137] A. Horn and C. R. Johnson, *Matrix Analysis*. Cambridge, UK: Cambridge University Press, 1985. 88
- [138] D. L. Donoho, "Compressed sensing," *IEEE Trans. Inf. Theory*, vol. 52, pp. 1289 – 1306, 2006. 103, 117
- [139] E. J. Candès, J. Romberg, and T. Tao, "Robust uncertainty principles: exact signal reconstruction from highly incomplete frequency information," *IEEE Trans. Inf. Theory*, vol. 52, pp. 489 – 509, 2006. 117
- [140] E. J. Candès and T. Tao, "Reflections on compressed sensing," *IEEE*

- Information Theory Society Newsletter*, vol. 58, pp. 20 – 23, 2008. 104, 112
- [141] E. J. Candès and M. B. Wakin, “An introduction to compressive sampling,” *IEEE Signal Process. Mag.*, vol. 25, pp. 21 – 30, 2008. 103, 104, 111, 112, 117
- [142] Z. Xu and E. Y. Lam, “Image reconstruction using spectroscopic and hyperspectral information for compressive terahertz imaging,” *J. Opt. Soc. Am. A*, vol. 27, no. 7, pp. 1638 – 1646, 2010. 104
- [143] A. Chai, M. Moscoso, and G. Papanicolaou, “Array imaging using intensity-only measurements,” *Inverse Probl.*, vol. 27, 2011. 104, 114, 120
- [144] L. Zhang, M. Xing, C. Qiu, J. Li, and Z. Bao, “Achieving higher resolution isar imaging with limited pulses via compressed sampling,” *Geosci. Rem. Sens. Lett. IEEE*, vol. 6, pp. 567 – 571, 2009. 104
- [145] L. Zhang, M. Xing, C. Qiu, J. Li, J. Sheng, Y. Li, and Z. Bao, “Resolution enhancement for inversed synthetic aperture radar imaging under low SNR via Improved Compressive Sensing,” *IEEE Trans. Geosci. Remote Sens.*, vol. 48, pp. 3824 – 38, 2010. 104
- [146] L. H. He and L. Carin, “Exploiting structure in wavelet-based bayesian compressive sensing,” *IEEE Trans. Signal Process.*, vol. 57, no. 9, pp. 3488 – 3497, 2009. 104
- [147] X. Chen, “Signal-subspace method approach to intensity-only



- electromagnetic inverse scattering problem,” *J. Opt. Soc. Am. A*, vol. 25, pp. 2018–2024, 2008. 107
- [148] L. Tsang, J. A. Kong, and K. H. Ding, *Scattering of Electromagnetic Waves: Theories and Applications*. New York: Wiley, 2000. 107
- [149] D. L. Marks, “A family of approximations spanning the Born and Rytov scattering series,” *Opt. Express*, vol. 14, no. 19, pp. 8837 – 8848, 2006. 107
- [150] L. Carin, D. Liu, W. Lin, and B. Guo, “Compressive sensing for multi-static scattering analysis,” *J. Comput. Phys.*, vol. 228, pp. 3464 – 3477. 111
- [151] L. Carin, “On the relationship between compressive sensing and random sensor arrays,” *IEEE Antennas Propag. Mag.*, vol. 51, no. 5, pp. 72 – 81, 2009. 111
- [152] E. Candès and T. Tao, “The dantzig selector: Statistical estimation when  $p$  is much larger than  $n$ ,” *Ann. Statist.*, vol. 35, no. 6, pp. 2313 – 2351, 2007. 113
- [153] E. J. Candès and J. Romberg, “11-magic: Recovery of sparse signals via convex programming,” <http://www.acm.caltech.edu/11magic/>. 114
- [154] E. A. Marengo, R. D. Hernandez, and H. Lev-Ari, “Intensity-only signal-subspace-based imaging,” *J. Opt. Soc. Am. A*, vol. 24, pp. 3619–3635, 2007. 114
- [155] M. Abramowitz and I. A. Stegun, *Handbook of Mathematical Functions*. Dover, 1964. 120

- 
- [156] X. Chen, “Subspace-based optimization method for inverse scattering problems with an inhomogeneous background medium,” *Inverse Probl.*, vol. 26, p. ID: 074007, 2010. 120
- [157] R. McCahan and R. Kleinman, “Special session on image reconstruction using real data,” *IEEE Antennas Propag. Mag.*, vol. 38, no. 3, p. 39, 1996. 124
- [158] —, “Second annual special session on image reconstruction using real data,” *IEEE Antennas Propag. Mag.*, vol. 39, no. 2, pp. 7 – 9, 1997.
- [159] R. McGahan and R. Kleinman, “Third annual special session on image reconstruction using real data, part 1,” *IEEE Antennas Propag. Mag.*, vol. 41, no. 1, pp. 34 – 36, 1999. 124
- [160] J. M. Gefferin, P. Sabouroux, and C. Eyraud, “Free space experimental scattering database continuation: experimental set-up and measurement precision,” *Inverse Probl.*, vol. 21, pp. S117–S130, 2005. 124
- [161] A. Litman and L. Crocco, “Testing inversion algorithms against experimental data: 3D targets,” *Inverse Probl.*, vol. 25, p. 020201, 2009. 124
- [162] C. Gilmore, A. Zakaria, P. Mojabi, M. Ostadrahimi, S. Pistorius, and J. LoVetri, “Near-field multi-static wideband microwave scattering repository for the testing of calibration and inversion algorithms,” in *IEEE Int. Symp. on Ant. and Prop. and USNC/URSI National Radio Science Meeting*, Spokane, Washington, USA, July 2011. 124

